

Progress Report on Numerical Modeling of a Prototype Fuel Cell:

1. Comparison between Mathematical Formulations

Otávio Beruski,^{1,*} Ivan Korkischko,¹ Thiago Lopes,¹ and Fabio Coral Fonseca¹

¹*Instituto de Pesquisas Energéticas e Nucleares,
IPEN/CNEN-SP, 05508-000, São Paulo, São Paulo, Brazil*

Abstract

Progress on the numerical modeling of a prototype fuel cell is reported. Some known limitations of the previously published Alpha model are addressed, and the numerical uncertainty due to discretization of the improved model, Beta, was estimated. In this part, the Beta model is compared to Alpha, where significant albeit small differences are seen. One noteworthy difference lies in the reactant usage, where the Beta model shows a better fit to available experimental data. Shortcomings of the improved model are discussed, paving the way forward, while a discrepancy with previous results is addressed, further suggesting the use of the Darcy-Brinkman over Stokes-Darcy formulation for free and porous media flow. Furthermore, a parametric study is carried out, constraining plausible values of the reaction rate constants to $10 < k_1 \approx 10^2 < 10^3 \text{ s}^{-1}$, for adsorption, and $k_2 \gtrsim 10^3 \text{ s}^{-1}$ for decomposition reactions. Additional opportunities for validation are identified, viz. the stoichiometry and reactant partial pressure profiles along the catalyst layer. Nevertheless, given the uncertainties in the numerical data and the available experimental data, the results lack validation power, highlighting the need for additional experimental data and improved precision for the numerical data.

I. INTRODUCTION

Research in fuel cell modeling has come a long way since the early work of Giner and Hunter[1] and Cutlip[2]. Constraints on resources and numerical techniques allowed only highly simplified models with low dimensionality and relatively coarse spatial and temporal resolution (see for instance the overview in [3]). The research field has now reached a level of maturity where relatively robust models are routinely coupled to empirical development, providing greater detail than most experiments are able to achieve ([4–6] and references therein). Fuel cells are known to harbor an awe-inspiring, perhaps frightening, set of coupled non-linear physical processes, covering a wide range of length and time scales[6–8]. Thus, despite the level of detail found in modern models, in both physical processes and resolution, accurate models still prove too demanding in most situations.

In order to deal with such complexity, not to mention the idiosyncrasies of each device, it is common to approximate, or even neglect, some phenomena, a notable case being two-

* oberuski@alumni.usp.br

phase flow in polymer electrolyte fuel cells (PEFCs). In this case, it is common to work in conditions where two-phase flow is minimized, such as high temperatures and stoichiometries (the ratio between molar influx and usage for a given reactant), with numerical models then ignoring the effects of two-phase flow[9–12]. On the other hand, in order to deal with it, one strategy has been to focus on the two-phase flow in porous media, using generalized Darcy’s law for each phase[6, 13], while another has been to use multiphase mixture models[6, 14, 15]. Of course, more complex models exist, for instance the ones compared in [16] for porous media, and phase field, level set, and volume-of-fluid for fully resolved two-phase flows. However these are in general transient-only models, computationally intensive and usually do not consider phase transition, although this point has developed rapidly[17, 18].

Another common source of approximations is the porous media, in particular the catalyst layer (CL). Apart from the possibility of two-phase flow, which is particular to some devices, the CL always show the complexities of dealing with reacting flow in porous media[6, 7]: Knudsen diffusivity is usually important; the reaction mechanisms involves several steps and intermediate species; the heterogeneous kinetics demands knowledge of the so-called triple-phase boundary (where reactant, electrolyte and electrode meet simultaneously) and its distribution within the porous medium; not to mention the effects of the overarching porous structure on mass, charge and heat transfer due to the distribution of pore radii and tortuosity of the pore network. Research on porous media is of course not restricted to fuel cells, and valuable input has been provided from other fields (see for instance [19–21] and more recently [22–24]).

Considering the interrelated complexities of the inner working of fuel cells, as briefly described above, a promising approach would be to investigate relatively simpler systems, with fewer or uncoupled phenomena, in order to acquire a firmer grasp on the common physical processes underlying both. Significant efforts are directed towards such approach, widely attempted and done all over the scientific community, however it is not always straightforward to find a suitable prototype. Half-cells are just an example, where part of the device is neglected in favor of a set of processes of interest, commonly employed in basic electrochemistry research. For fuel cells, half-cells are used to some extent, however they are not only somewhat difficult to operate, they still exhibit most of the complexity of a full device. In this context, a prototype half-cell system has been developed that puts aside both charge and heat transfer[25], focusing on single-phase fluid flow and species transfer of a PEFC-like

device. In a similar fashion, a setup allowing direct visualization of reactant transport with liquid flow has been developed for redox flow batteries[26]. Work on such prototypes allows greater control and a clearer view of the processes underlying mass transfer in fuel cells and similar devices, for both experimental[27] and computational[28] research.

We build on the previously published model for the aforementioned prototype fuel cell cathode[28], with the main goals of improving the mathematical framework, and therefore its accuracy, and estimating the discretization error, thus assessing its precision. In this part[29], known limitations of the original model have been addressed, such as the use of Fick’s law for species diffusion and a homogeneous reaction model. A comparison between formulations and to existing experimental data is then carried out, and a parametric study on the reaction rate constants was performed in order to assess the behavior of the response variables as function of these degrees of freedom. Shortcomings of the new model are addressed and discussed, for instance by considering the results of Part 2 on the discretization error and validation, and bounds for reasonable values for the reaction rate constants are drawn. In this way, this manuscript is organized as follows. Section II provides an overview of the original model’s mathematical formulation and the improvements made, as well as the details for the comparison between models and parametric study. Section III first presents the comparison between model formulations, followed by a discussion addressing shortcomings pointed out during the development of the work. Afterwards, the parametric study on reaction rate constants is presented, pointing out instances of validation that might be used in future work and establishing the range of values that reasonably reproduce the known experimental response. Finally, Section IV concludes with a summary of the results and brief remarks on future studies.

II. METHODS

We first present a brief description of the experimental device that is simulated by our model, first described by Lopes *et al.*[25], followed by the computational methods used for the development of this work.

The device is a prototype polymer electrolyte fuel cell (PEFC), more specifically a cathodic half-cell, which allows *in situ* observation of reactive fluid flow in a porous medium. Ozone-enriched air is used as tracer in a carrier fluid, and a coumarin-based dye is used as

the sensor to map the local concentration of O_3 . The O_3 interacts with the dye anchored on silica particles, akin to electrocatalysts dispersed in a porous layer, resulting in the emission of photons and the degradation of both reactant and dye. Measuring the light emission from this “catalyst layer” allows determination of the local O_3 concentration and, thus, the species and fluid dynamics. Global variables, such as pressure drop and total reactant drop, provide additional information on the inner workings of the device.

Thus, considering the experimental device, the proposed computational model covers momentum and species transport, while assuming thermal equilibrium and steady state. The computational domains included are: i) the flow channel (Ch), in this case a single serpentine geometry, ii) the porous transport layer, here comprising only a macroporous substrate (MPS) made of carbon paper (representing Toray TGH-060 with a 10% PTFE hydrophobic treatment), and iii) the catalyst layer (CL), where the catalyst and substrate particles are considered homogeneously distributed (representing Sigma Aldrich Nano Silica Gel on TLC plates, see [25] for details). Domains ii) and iii) comprise the porous media domains (Pm). Figure 1 shows the domains’ disposition and Table I presents the geometrical parameters.

The setup used for all simulations was a workstation with two Intel® Xeon® E3 processors and 128GB of RAM, operated with a 64 bits Debian9 distribution, Linux kernel v. 4.9.0-4. The software used was the commercial package COMSOL Multiphysics®, v.5.1.0.234, along with the Batteries and Fuel Cell, CFD, and Chemical Engineering modules. All data handling and processing was done using GNU Octave v.4.2.1[30], while image processing was done using GIMP v.2.10.14[31].

A. Mathematical Formulation

1. Original model: *Alpha*

The original mathematical formulation, henceforth denominated *Alpha*, can be found in [28], but a brief description will be given below followed by the improvements which are the focus of this work.

The momentum transport is described using the (compressible) Darcy-Brinkman formulation (DB), which covers both free and porous media flow[32], coupled to conservation of

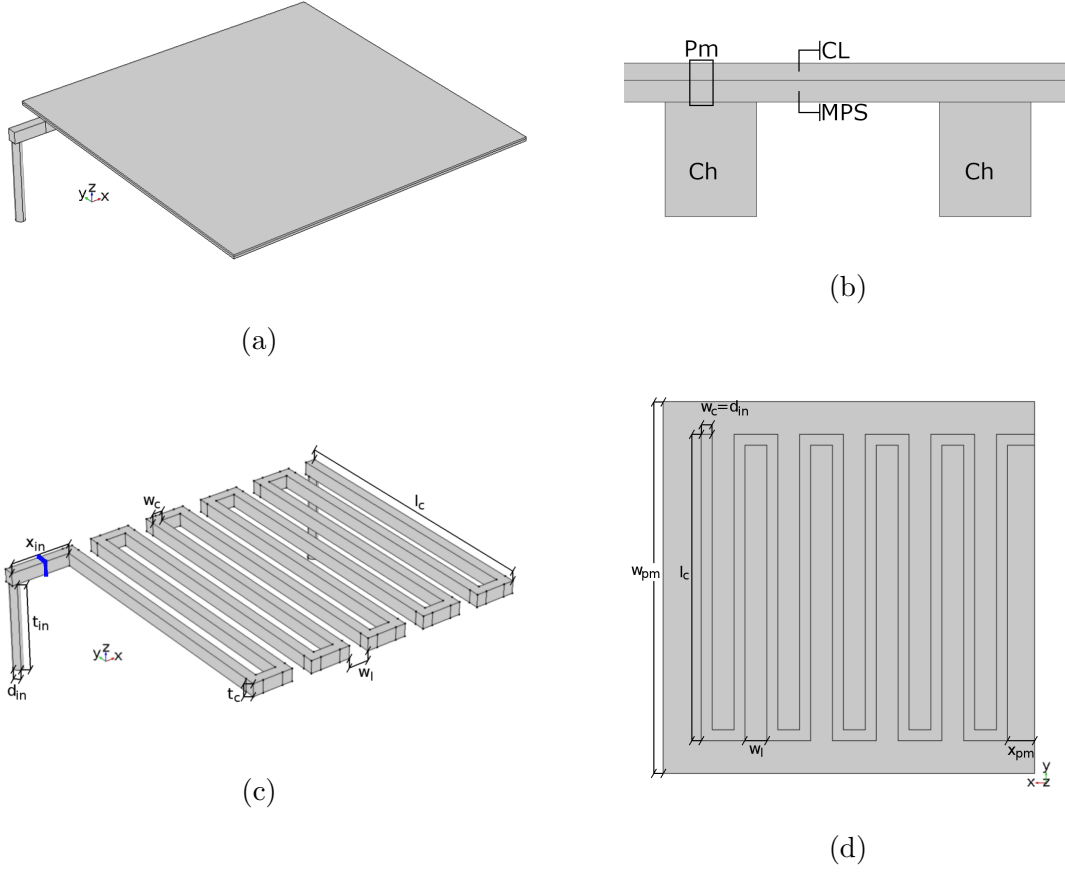


FIG. 1: Geometry used in the proto-cell simulations: **(a)** full geometry, showing the flow channel (Ch) and porous media (Pm) domains; **(b)** cross-section in the xz plane, showing the structure along the z axis; **(c)** Ch domain, with the segmentation edges shown in blue (see text), and **(d)** lower boundary of the MPS domain, showing the projection of the Ch domain.

mass:

$$\frac{\rho}{\epsilon} (\mathbf{u} \cdot \nabla) \left(\frac{\mathbf{u}}{\epsilon} \right) = \nabla \left[-P\mathbf{I} + \frac{\mu}{\epsilon} \left(\nabla \mathbf{u} + (\nabla \mathbf{u})^T \right) - \frac{2\mu}{3\epsilon} (\nabla \cdot \mathbf{u}) \mathbf{I} \right] - \frac{\mu}{\kappa} \mathbf{u}, \quad (1)$$

$$\nabla \cdot (\rho \mathbf{u}) = 0, \quad (2)$$

where ρ and μ are the fluid's density and kinematic viscosity, respectively, \mathbf{u} is the velocity field vector, P is the relative pressure, and ϵ and κ are the domain's porosity and permeability, respectively ($\epsilon = 1$ and $\kappa \rightarrow \infty$ for free flow). As shown in [28], DB provides a better description of this system when compared to a Stokes-Darcy approach, i.e. manually coupling the Navier-Stokes equation for the Ch domain and Darcy's law for porous media. The

TABLE I: Geometrical parameters of the computational domains.

Parameter	Symbol	Value
Channel width	w_c	0.8 mm
Land width	w_l	1.6 mm
Channel depth	t_c	1.0 mm
Channel section length	l_c	22.4 mm
Inlet/outlet diameter	d_{in}	0.8 mm
Inlet/outlet length	t_{in}	7.0 mm
Inlet offset	x_{in}	4.7752 mm
Porous media edge	w_{pm}	$(l_c + x_{in})$
Porous media offset	x_{pm}	$(x_{in} - w_w)/2$
MPS thickness	t_{MPS}	190 μm
CL thickness	t_{CL}	150 μm

parameters are shown in Table II, chosen in order to describe the materials and conditions used (see [25] for additional information). A normal inflow velocity, as inlet, and a constant pressure boundary conditions, for the outlet, were used.

The species transport was originally modeled using a diluted-species approach, coupling the advection-reaction equation:

$$\nabla \cdot \mathbf{J}_{O_3} + (\mathbf{u} \cdot \nabla) C_{O_3} = R_{O_3}, \quad (3)$$

to Fick's law of diffusion, which defines the molar diffusive flux vector:

$$\mathbf{J}_{O_3} = -D_{O_3} \nabla C_{O_3}, \quad (4)$$

where D_{O_3} and C_{O_3} are the diffusion coefficient and the concentration of ozone, respectively. Given the inlet concentration of the species of interest, $C_{O_3,in}$, of the order 10^3 ppm, such an approach was considered reasonable[28]. The diffusion was corrected for porous media transport:

$$D_{O_3}^{Pm} = f_{Pm} D_{O_3}, \quad (5)$$

where $f_{Pm} = f_{Pm}(\epsilon, \tau)$, with τ being the medium's tortuosity. A common form for f_{Pm} is:

$$f_{Pm} = \frac{\epsilon}{\tau}, \quad (6)$$

which might be readily used whenever τ is available, as is the case of the MPS domain. Otherwise, a porous medium model might be used, typically with the form $\tau = \tau(\epsilon)$. In this case, for the CL domain, the Millington & Quirk model was used[33], as implemented in the software, giving $\tau = \epsilon^{1/2}$. The reaction term was defined by a homogeneous first-order reaction:

$$R_{O_3} = -k_{\text{app}}C_{O_3}, \quad (7)$$

where the apparent reaction rate constant, k_{app} , is a free parameter to be adjusted against experimental data. Parameters are shown in Table II.

TABLE II: Parameterization of both models.

Parameter	Symbol	Value	Reference
Inlet concentration of O ₃	$C_{O_3,\text{in}}$	$1200 \times 10^{-6} \text{ mol m}^{-3}$	[25, 28]
Reference pressure	P_{ref}	1.027 bar	[28]
Cell back pressure	P_{out}	$1.0994 \text{ bar} - P_{\text{ref}}$	[28]
Carbon paper porosity	ϵ_{MPS}	0.801	[34]
Carbon paper permeability	κ_{MPS}	$9.18 \times 10^{-12} \text{ m}^2$	[35]
Carbon paper tortuosity	τ_{MPS}	1.199	[35]
Catalyst layer porosity	ϵ_{CL}	0.497	[28]
Catalyst layer permeability	κ_{CL}	$8.82 \times 10^{-11} \text{ m}^2$	[28]
O ₃ diffusion coefficient in N ₂	D_{O_3}	$0.16 \text{ cm}^2\text{s}^{-1}$	[36, 37]
O ₃ apparent reaction rate constant ^a	k_{app}	256.15 s^{-1}	[28]

^a Parameter used only in the original (Alpha) model.

Finally, for the sake of reference, the mesh used in [28] followed a custom-made procedure, based on the software’s recommendations, with ca. 1.7×10^6 domain elements. The set of equations was solved using a two-step segregated solver, with each step using an implementation of the PARDISO[38] linear solver, to a relative tolerance of 10^{-3} . A parametric solver was used to vary the inlet flow rate, with initial value $Q = 200 \text{ cm}^3 \text{ min}^{-1}$ and a step of $\delta Q = 50 \text{ cm}^3 \text{ min}^{-1}$ up to $450 \text{ cm}^3 \text{ min}^{-1}$, where each solution was used as the next step’s initial value.

2. Improved model: Beta

The improvements were largely implemented in the species transport formulation, with a closely related addition of surface cover kinetics, with two relatively minor changes in momentum transport and one in the model geometry. These modifications make up the *Beta* model. Additional parameters relevant to the Beta model are given in Table III.

TABLE III: Parameters relevant to the improved (Beta) model.

Parameter	Symbol	Value	Reference
Inlet molar fraction of O ₃	$\chi_{\text{O}_3, \text{in}}$	1200 ppm	[25]
Average molar mass of dry air	M_{air}	28.96546 g mol ⁻¹	[39]
O ₃ adsorption reaction rate constant	k_1	100 s ⁻¹	see text
O ₃ (ads) decomposition reaction rate constant	k_2	10 s ⁻¹	see text
Average silica particle radius	r_p	6.5 μm	see text
Quantity of dye deposited on the CL	Γ_{dye}	3 $\mu\text{mol cm}^{-2}$	[25]

The main change in the model was the use of a concentrated-species approach to the fluid, which uses the following statement of species conservation, i.e. the advection-reaction equation:

$$\nabla \cdot \mathbf{J}_i + \rho(\mathbf{u} \cdot \nabla) \omega_i = R_i, \quad (8)$$

where ω_i is the mass fraction of the i -th species, while the *mass* diffusive flux is given by the Maxwell-Stefan (MS) model:

$$\mathbf{J}_i = - \left(\rho \omega_i \sum_k D_{ik} \mathbf{d}_k \right) \quad (9)$$

$$\mathbf{d}_k = \nabla \chi_k + \frac{[(\chi_k - \omega_k) \nabla P_A]}{P_A}, \quad (10)$$

where D_{ik} are multi-component diffusivities, \mathbf{d}_k is a so-called diffusional driving force, χ_k is the molar fraction and P_A is the absolute pressure. According to the User Guide for COMSOL's Batteries and Fuel Cells module, in the version used the D_{ik} are multi-component Fick diffusivities, which are obtained from the MS diffusion matrix by solving the following relation:

$$\frac{\chi_i \chi_k}{D_{ik}^{\text{MS}}} = -\omega_i \omega_k \frac{\sum_{j \neq i} (\text{adj} B_i)_{jk}}{\sum_{j \neq i} D_{ij} (\text{adj} B_i)_{jk}}, \quad (11)$$

where D_{ik}^{MS} are the binary MS diffusion coefficients, $(B_i)_{kj} = D_{kj} - D_{ij}$, for $i \neq j$, and adj stands for the adjoint operation $\text{adj}(A_{ij}) = A_{ji}^*$, where $*$ is the complex conjugate. Both the MS and multi-component Fick diffusion matrices are symmetric. Furthermore, for two- and three-component mixtures, the software has analytical expressions for D_{ik} implemented, while for four components or more a numerical procedure is used. In addition to multi-component diffusion, the Knudsen regime was implemented for porous media transport:

$$D_{ij}^{\text{MS}} = \left[\frac{1}{D_{ij}^{\text{Pm}}} + \frac{1}{D_{ij}^{\text{K}}} \right]^{-1}. \quad (12)$$

Here two effects are added in a parallel-resistances fashion: i) the porous media diffusion coefficient, D_{ij}^{Pm} , which follows Eq. 5; and ii) the Knudsen regime diffusivity, obtained through kinetic theory:

$$D_i^{\text{K}} = \frac{d_p}{3} \sqrt{\frac{8RT}{\pi M_i}}, \quad (13)$$

where d_p is the average pore diameter, commonly used instead of the mean free path in porous media, R is the gas constant, T is the temperature and M_i is the molar mass. In this case, the average pore diameter is obtained using the Millington & Quirk model for cemented particle beds[33] for simplicity. It will be noticed that Eq. 13 is written for a single species, and it is not clear how a binary Knudsen diffusion coefficient should be expressed. One option would be to calculate an average molar mass between a pair of species, weighed by their relative molar fractions. Another would be to sum the individual coefficients in a similar fashion as Eq. 12, weighed by their relative molar fractions. While this may be worthwhile to investigate, it is neglected at this point, as discussed below.

Considering the formulation described, a few issues should be addressed. First, by switching to the MS model, the D_{O_3} used in Eq. 4 is no longer valid, being necessary appropriate MS binary diffusivities instead. Due to the difficulty of obtaining these coefficients, and given that the concentration of ozone is small, whereas that of N_2 and O_2 are approximately constant, the value given in Table II is still used. Second, given the constant relative concentrations of N_2 and O_2 , and to minimize computational costs, the components of the mixture were O_3 and “air”, the latter with a molar mass of M_{air} (see Table III). A brief discussion on this issue will be given in Section III A 1. See also Section SII of the Supplemental Material[40] (SM) for a comparison between results using $\text{O}_3/\text{O}_2/\text{N}_2$ or O_3/air mixtures.

Finally, it is not clear how the different phenomena affecting diffusion couple together, such as shown in Eq. 12. For instance, whether it is appropriate to correct the free diffusion

coefficient before calculating the multi-component Fick diffusivities, or, given the formulation and software limitations, how to correctly couple the individual Knudsen diffusivities to the Maxwell-Stefan diffusivities. The approach used here relies on the approximation of the constant N₂/O₂ mixture as “air”, which results in a single entry in the MS diffusion matrix, then assuming ozone as being the sole contribution to the term ($M_i = M_{O_3}$). It is also understood that the porous media affect species transport despite the contribution of the Knudsen regime, thus the application of the correction factor in Eq. 12. Section III A 1 provides some discussion around this issue. Section SIII of the SM[40] provides a comparison with a few possibilities regarding this issue, in order to illustrate the expected effects in the system under study.

Back to the mathematical formulation, the reaction involving ozone degradation, and hence light emission, was modified to include the interaction with the dye molecule in an adsorption-desorption step, then leading to decomposition:



where the dye molecule is 7-diethylamino-4-methylcoumarin[25]. In this way, a new variable was defined, θ_{O_3} , representing the surface coverage of ozone, with kinetics modeled by the differential equation:

$$\frac{d\theta_{O_3}}{dt} = k_1 c_{O_3} \chi_{O_3} (1 - \theta_{O_3}) - k_{-1} \theta_{O_3} - k_2 \theta_{O_3}, \quad (16)$$

where c_{O_3} is the ratio of the appropriate activity coefficients for bulk and adsorbed O₃, k_1 and k_{-1} are the forward and backward reaction rate constants for the adsorption-desorption reaction, respectively, and k_2 is the reaction rate constant for the decomposition reaction. Eq. 16 can be written as function of alternative variables concerning O₃, such as mass fraction or density, with the appropriate factors incorporated in the reaction rate constant. To couple with Eq. 8, one may write:

$$A_v \Gamma_s^* \frac{d\theta_{O_3}}{dt} = R_{O_3, \text{ads}}, \quad (17)$$

which corresponds to the total reaction rate for the adsorbed ozone over the CL domain, in mol s⁻¹, given that A_v is the total surface area by unit volume and Γ_s^* is the total surface concentration of active sites, i.e. dye molecules (see below). Thus, by excluding the last

term of Eq. 16, one may write the sink term for bulk ozone as:

$$R_{O_3} = -M_{O_3}R_{O_3,ads} - M_{O_3}A_v\Gamma_s^*k_2\theta_{O_3} \quad (18)$$

since the source/sink term in Eq. 8 is given in units of $\text{kg m}^{-3} \text{s}^{-1}$. For simplicity, the desorption term was neglected, thus leaving the sink term as:

$$R_{O_3} = -M_{O_3}A_v\Gamma_s^*k_1\chi_{O_3}(1 - \theta_{O_3}), \quad (19)$$

where it was further assumed that $c_{O_3} \approx 1$. The total surface concentration of adsorption sites can be obtained with:

$$\Gamma_s^* = \frac{\Gamma_{\text{dye}}}{t_{\text{CL}}A_v}, \quad (20)$$

where Γ_{dye} is the reported[25] quantity of dye deposited over a given geometric area of CL with thickness t_{CL} . The A_v can, in principle, be determined experimentally, but for now it is calculated using a simple model:

$$A_v = \frac{3\epsilon_{\text{CL}}}{r_p}, \quad (21)$$

where r_p is the average particle radius, in this case the silica particles where the dye were anchored on (Nano Silica Gel, Sigma Aldrich).

Regarding the minor changes in momentum transport, the first concerns the inclusion of a mass source term to Eqs. 1 and 2 accounting for the reaction in the CL domain:

$$S_M = R_{O_3}. \quad (22)$$

The momentum formulation written for the Beta model is thus written as:

$$\frac{\rho}{\epsilon}(\mathbf{u} \cdot \nabla) \left(\frac{\mathbf{u}}{\epsilon} \right) = \nabla \left[-P\mathbf{I} + \frac{\mu}{\epsilon} (\nabla \mathbf{u} + (\nabla \mathbf{u})^T) - \frac{2\mu}{3\epsilon} (\nabla \cdot \mathbf{u}) \mathbf{I} \right] + \left(\frac{S_M}{\epsilon^2} - \frac{\mu}{\kappa} \right) \mathbf{u} \quad (23)$$

$$\nabla \cdot (\rho \mathbf{u}) = S_M, \quad (24)$$

where S_M is defined by Eq. 22 in the CL domain only, being zero otherwise. While the inclusion of a source term may be considered a major change theoretically, it is deemed minor in this case since the magnitude of S_M is expected to be quite small when compared to the remaining terms in the DB formulation. The second change refers to the inlet boundary condition, where a (standard) mass flow rate condition is now being used:

$$-\int_{\partial\Omega} \frac{\rho}{\rho_{\text{std}}} (\mathbf{u} \cdot \mathbf{n}) dS = Q, \quad (25)$$

with dry air at $T_{\text{std}} = 273.15$ K and $P_{\text{std}} = 1$ atm defining the standard density $\rho_{\text{std}} = P_{\text{std}}M_{\text{air}}/RT_{\text{std}}$. Finally, given the use of a concentrated-species approach to species transport, the fluid composition is expected to play a role in its properties. However, for simplicity, the density is still given by the ideal gas law, while the viscosity is given by a constitutive relation for air, provided by the software:

$$\begin{aligned} \mu_{\text{air}}(T) = & -8.38278 \times 10^{-7} + 8.35717342 \times 10^{-8}T - 7.69429583 \times 10^{-11}T^2 \\ & + 4.6437266 \times 10^{-14}T^3 - 1.06585607 \times 10^{-17}T^4, \end{aligned} \quad (26)$$

where μ_{air} has units of Pa s and T of K.

The final minor change is related to geometry of the domains. The full geometry was an assembly of two distinct geometrical entities: the Ch and the Pm domains. The Ch domain follows the description in [28], with the following modifications: i) the inlet and outlet sections were extended to fully cover the supporting plates existing in the experimental prototype (7 mm)[25], and ii) the upper boundary, partly in contact with the MPS, was segmented in two, corresponding to the section in contact with the MPS and the remaining part, closer to the inlet. The Pm domains are simply parallelepipeds, with the addition of a copy of the Ch upper boundary at the lower boundary of the MPS, representing the part of the boundary in contact with the Ch domain. Figures 1c and 1d illustrate the above points. As a consequence of these changes, explicit coupling between the geometric entities was needed to ensure the proper continuity of the variables, i.e. the flow field, \mathbf{u} , and ozone mass fraction, ω_{O_3} . This was accomplished via an identity pair. Since the relevant boundaries were sectioned to properly match one another (at the Ch and MPS domains), no fallback features were necessary.

The mesh and solver schemes are described in more detail in Part 2, as well as the experimentation and mesh convergence study performed for this model. In this part of the work, three meshes were used with decreasing spatial resolution, termed meshes #1 to #3 ($\sigma = 12, 6, 4$), with the following outline:

1. Meshing of the Ch domain with tetrahedral elements, with scaling factor σ .
2. Copying the upper boundary of the Ch mesh to the projection onto the lower MPS boundary.

3. Meshing the remainder of the lower MPS boundary with triangular elements, with scaling factor 1.
4. Extruding the lower boundary elements throughout the Pm domains, with σ elements in each domain.

The final solution, shown in Section III, used mesh #1, with ca. 8.86×10^6 domain elements. The solver scheme was a two-step solution using meshes #2 and #1, with #2 at inlet flow rate $Q = 200 \text{ cm}^3 \text{ min}^{-1}$ as the initial values for mesh #1. The general outline for the solver for each step was the following: a segregated 3-steps solver was employed, with step i) solving for θ_{O_3} , step ii) solving for \mathbf{u} and P , and step iii) solving for ω_{O_3} . Step i) employed a direct solver based on MUMPS[44, 45], step ii) employed an iterative solver based on GMRES[46] with a geometric multigrid scheme as pre-conditioner, and step iii) employed the same GMRES-based iterative solver however using the domain decomposition method[47]. For the first solution, using mesh #2, mesh #3 was used as the coarse multigrid level, while for the second solution, with mesh #1, both meshes #2 and #3 were used. Finally, for the second step, a parametric solver was employed for Q , with $200 \leq Q \leq 450 \text{ cm}^3 \text{ min}^{-1}$ and a step of $\delta Q = 50 \text{ cm}^3 \text{ min}^{-1}$.

B. Model Comparison

The models described in Section II A were compared to each other. Similarly to the mesh convergence analysis described in Part 2, the response variables were chosen for compatibility with the experimental device, envisioning future validation rounds against empirical data. The chosen quantities are the following:

- the ratio K' between reactant consumption $\Delta\chi_{\text{O}_3}$ and apparent reaction rate R'_{O_3} ;
- the stoichiometry λ and apparent stoichiometry λ' ;
- ozone partial pressure and normalized reaction rate profiles, $P_{\text{O}_3}(x)$ and $\bar{R}_{\text{O}_3}(x)$ respectively, obtained at the upper surface of the CL, along the x axis;
- ozone partial pressure and normalized reaction rate surfaces, \mathbf{P}_{O_3} and $\bar{\mathbf{R}}_{\text{O}_3}$ respectively, obtained at the upper surface of the CL domain.

Since the models differ mainly in the species transport formulations, in particular concerning the reaction kinetics, the ratio K' , stoichiometries λ and λ' , and \bar{R}_{O_3} profiles and surfaces were primarily used for comparison. The individual variables, $\Delta\chi_{O_3}$ and R'_{O_3} , as well as P_{O_3} profiles and surfaces, were also compared for the sake of completeness, however the differences in formulation and parameterization should be taken in account when analyzing the results. Variables solely related to the flow field, such as pressure drop and flow speed profile, were not expected to show significant changes and are shown in Section SIV.A of the SM[40].

Another consequence of the difference in species transport formulation is that C_{O_3} is not the same for both models. This is because the Alpha model uses a diluted species approach that does not considers the solvent explicitly, thus molar fraction is not an available variable. However, since the excess of solvent with respect to the solute does not affect the results, using an inlet concentration of $C_{O_3,in}^{(\alpha)} = 1200 \times 10^{-6} \text{ mol m}^{-3}$ is essentially the same as saying that there is 1200×10^{-6} moles of O_3 for each mole of solvent. Thus, in general, one may use $\chi_{O_3}^{(\alpha)} = C_{O_3}^{(\alpha)} / C^*$, where $C^* = 1 \text{ mol m}^{-3}$. While the work reported in [28] corroborates this approach, the Alpha and Beta models are not directly comparable even when disregarding formulation differences, where the latter explicitly uses $\chi_{O_3,in}^{(\beta)} = 1200 \text{ ppm}$. Therefore, variables which depend on molar concentrations, notably R'_{O_3} and consequently $\Delta\chi_{O_3}/R'_{O_3}$, have to be processed before comparing them.

A brief description of the acquisition of the response variables will now be given. Figure 2 illustrates the relevant geometrical entities used for the acquisition of the data. While a reduced geometry is shown (used in Part 2 and Section II C, below), the same were used here, appropriately scaled. $\Delta\chi_{O_3}$ is simply the difference in value between inlet and outlet averages of χ_{O_3} , thus $\Delta\chi_{O_3}^{(\alpha)} = \Delta C_{O_3} / C^*$, while $\Delta\chi_{O_3}^{(\beta)} = \Delta\chi_{O_3}$. R'_{O_3} is given by integration of the decomposition term for O_3 over the upper CL upper boundary. For Alpha, $R_{O_3,dec}$ is the sink term of Eq. 7; while for Beta, it is $R_{O_3,dec}^{(\beta)} = A_v \Gamma_s^* k_2 \theta_{O_3}$, which is the volume-averaged decomposition term for θ_{O_3} . Since $C_{O_3}^{(\alpha)} \neq C_{O_3}^{(\beta)}$, R'_{O_3} was normalized by $C_{O_3,in}$. Thus:

$$R'_{O_3} = \frac{\int_{\partial\Omega} R_{O_3,dec}(\mathbf{r}) dA}{C_{O_3,in}}, \quad (27)$$

where $\partial\Omega$ is the upper CL boundary (Fig. 2a). The stoichiometry λ is defined as:

$$\lambda = \frac{\dot{n}_{O_3,in}}{R_{O_3}}, \quad (28)$$

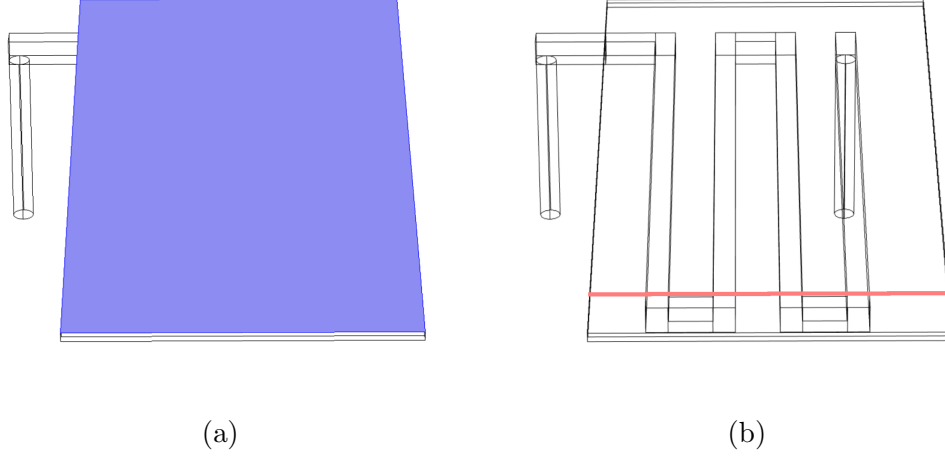


FIG. 2: Geometrical entities used to obtain the variables relevant for mesh convergence, shown for the reduced geometry: **(a)** surface used to obtain the apparent reaction rate, corresponding to the upper boundary of the CL domain; and **(b)** line used to track the ozone partial pressure profile atop the CL domain.

where $\dot{n}_{\text{O}_3, \text{in}}$ is the inlet molar rate of O_3 , obtained in a simplified manner as $\dot{n}_{\text{O}_3, \text{in}} = Q C_{\text{O}_3, \text{in}}$; while R_{O_3} is the total O_3 decomposition rate in the CL domain:

$$R_{\text{O}_3} = \int_{\Omega} R_{\text{O}_3, \text{dec}}(\mathbf{r}) \, dV, \quad (29)$$

with Ω being the CL domain. The apparent stoichiometry λ' is given by $\lambda' = \Delta \chi_{\text{O}_3} / \chi_{\text{O}_3, \text{in}}$, and is an approximation of λ more easily obtained experimentally. The $P_{\text{O}_3}(x)$ and $\bar{R}_{\text{O}_3}(x)$ profiles were obtained at the upper CL boundary (Fig. 2b), along a line parallel to the x axis, passing over the turn sections of the flow channel. The \mathbf{P}_{O_3} and $\bar{\mathbf{R}}_{\text{O}_3}$ surfaces were obtained at the upper CL boundary (Fig. 2a). For both models, $P_{\text{O}_3} = \chi_{\text{O}_3} P_A$, and thus $P_{\text{O}_3}^{(\alpha)} = C_{\text{O}_3}^{(\alpha)} P_A / C^*$; while \bar{R}_{O_3} is simply the decomposition term for a given model, $R_{\text{O}_3, \text{dec}}(\mathbf{r})$, normalized by $R_{\text{O}_3} V_{\text{CL}}$, where V_{CL} is the geometrical volume of the CL domain.

Finally, in order to ascertain that differences between models are not due to mesh influence, both Alpha and Beta models were run using the mesh chosen after the convergence analysis (see Part 2), briefly described at the end of Section II A 2. Thus, differences are expected between the results presented by Alpha in Section III and those reported in [28].

C. Parametric Study of Reaction Rate Constants

Similarly to what has been previously reported for the Alpha model[28], a parametric study has been carried out for the reaction rate constants related to the adsorption-decomposition reactions of ozone, k_1 and k_2 . This was done in order to assess the dependency of the chosen response variables to the order of magnitude of these parameters, arguably the major source of uncertainty in the Beta model. In this way, while a proper validation of the model would demand well-defined parameters, it may be possible to establish a range of k_1 and k_2 values where the model reasonably reproduce the experimental data available. This would, in turn, provide a rough prediction of the reaction rate constants, while at the same time constraining the model concerning its allowed behavior when compared to independently measured experimental variables.

The parametric study was carried using the Beta model, as described in Section II A 2, using the mesh and solvers described at the end of said section. The geometry was, however, reduced, in order to minimize time and computational resources spent on the simulations. This reduced geometry, shown in Fig. 2, was used for the mesh convergence study, described in Part 2. Since we are interested in relative changes in behavior due to changes in both k_1 and k_2 values, it is expected that the same conclusions hold for the full geometry. The study covers a range of 5 orders of magnitude, for both rate constants, centered on the value given in Table III. Thus, the parameters assumed the values given by the sets:

$$k_1 \in [1, 10, 10^2, 10^3, 10^4] \text{ s}^{-1} \text{ and} \\ k_2 \in [10^{-1}, 1, 10, 10^2, 10^3] \text{ s}^{-1},$$

where each parameter was varied independently of the other. For each doublet $\{k_1, k_2\}$, an auxiliary parametric study was used such that the inlet flow rate assumed the values $Q \in [250, 350, 450] \text{ cm}^3 \text{ min}^{-1}$. The response variables analyzed are the same used for model comparison, described in Section II B.

III. RESULTS

As mentioned in Section I, first a comparison between model formulations will be carried, along with comparison to experimental data when available. Afterwards, some shortcomings pointed out during the development of the work will be addressed and discussed, along

with further improvements that might be important for the model. Finally, the parametric study of reaction rate constants will be presented and its implications for model validation discussed.

A. Model Comparison

The improvements described on Section II A 2 were made based on well-known limitations of the original model, regarding the physical phenomena described by it. Thus, the Beta model is expected to more accurately replicate the physical phenomena underlying the experimental device. While a better fit to experimental data is expected, it is not at all guaranteed and neither is the current goal of this work. We focus here on the description of the Beta model, and its comparison with Alpha, as a reference frame for future comprehensive validation against experimental data. A brief discussion on this point will be given in Section III A 1.

Starting with the scalar response variables, Figure 3 shows the ratio $K' = \Delta\chi_{\text{O}_3}/R'_{\text{O}_3}$, its individual variables, and the stoichiometries λ and λ' . As mentioned in Section II B, the variables concerning the flow field are left to the SM[40] (Section SIV.A, Figs. S10 and S11). The most straightforward comparisons between models are given by K' and the stoichiometries, as they normalize the differences in reaction modeling and species transport formulation. Concerning K' , Fig. 3a, it can be observed that the Beta model shows a slightly higher rate of variation with Q than the Alpha model, suggesting that the changes implemented do affect the results qualitatively. Concerning the stoichiometries, Fig. 3b, for both λ and λ' the Alpha model predicts a higher value at all Q , also displaying a larger rate of increase. It is noticeable that, for λ' , the Beta model reproduces the available experimental data quite well, particularly at high Q . The reactant drop $\Delta\chi_{\text{O}_3}$, shown in Fig. 3c, corroborates this as expected, showing a closer fit to the experimental data from the Beta model, while the Alpha model predicts an almost linear decrease in $\Delta\chi_{\text{O}_3}$ with Q . The inlet-normalized apparent reaction rate $R'_{\text{O}_3}/C_{\text{O}_3,\text{in}}$, shown in Fig. 3d, shows little difference between models, with the Alpha model predicting slightly higher values.

A possible interpretation of Fig. 3 is that Q , and thus the convective transport, play a larger role in reactant transport in the Alpha model. Larger values of $R'_{\text{O}_3}/C_{\text{O}_3,\text{in}}$ for the Alpha model, despite lower $\Delta\chi_{\text{O}_3}$ ones, might suggest that reactants are brought to the

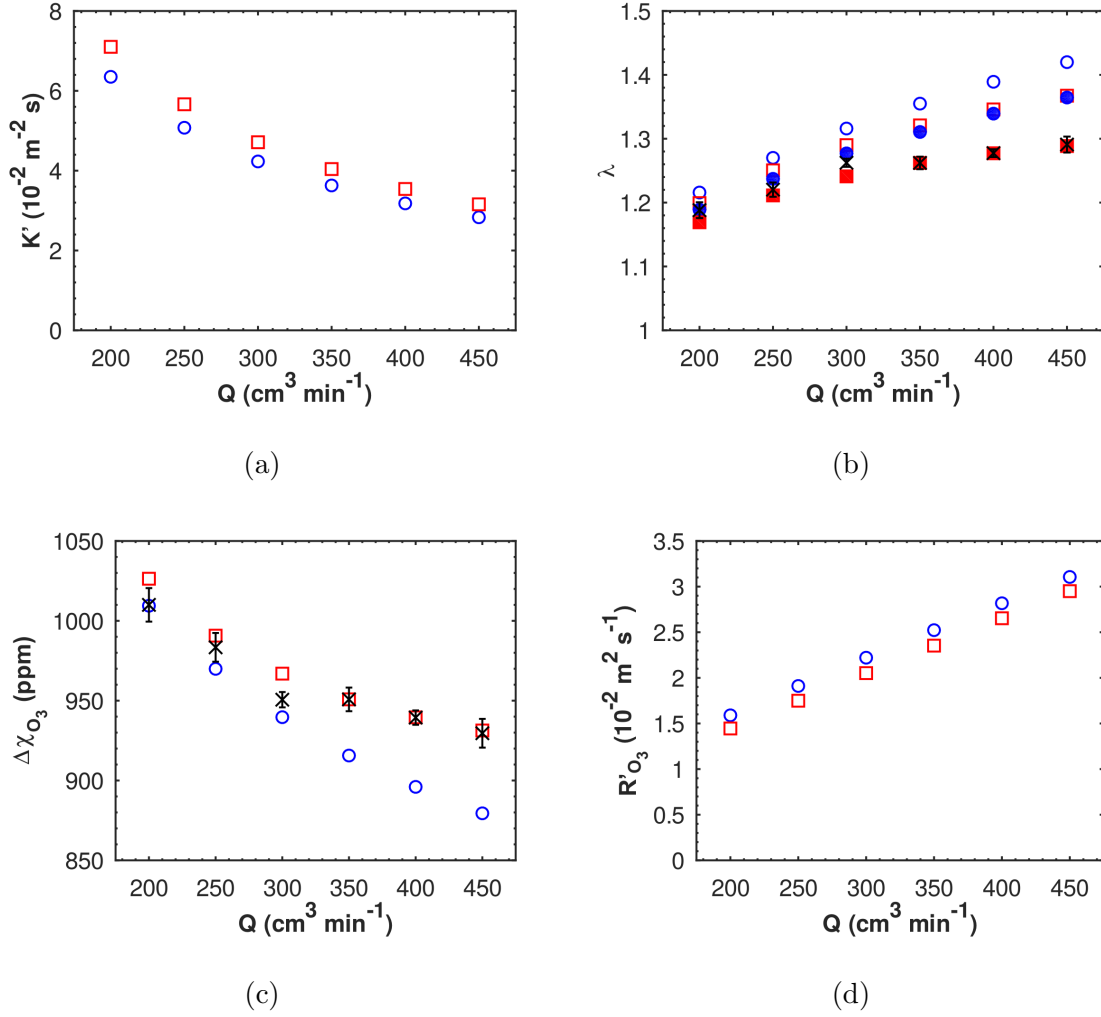


FIG. 3: Scalar variables as function of the inlet flow rate for the Alpha (\circ) and Beta (\square) models: **(a)** K' , **(b)** λ (empty) and λ' (full), **(c)** $\Delta\chi_{\text{O}_3}$, and **(d)** $R'_{\text{O}_3}/C_{\text{O}_3,\text{in}}$. Experimental data[28] (\times) is also shown in **(b)** and **(c)** as reference, with error bars representing one standard deviation.

upper CL surface more efficiently. On the other hand, the faster drop of $\Delta\chi_{\text{O}_3}$ with Q , as well as the higher values of λ , suggests that the reactants are also removed more efficiently from the CL. Comparison with available data, however, suggests this is not the case in the experimental device, and that the Beta model more closely captures this convective contribution.

Two points should be kept in mind, however. The first being that the reaction rate constants are degrees of freedom in both models, and thus variables that depend on it

must be analyzed with care, such as $\Delta\chi_{\text{O}_3}$ and λ' . Section IIIB provides a discussion over this issue. The second point is the matter of magnitude of C_{O_3} , as pointed out in Section IIB. While the overall effect is mainly a shift in order of magnitude in K' and R'_{O_3} , this suggests that the Alpha model would not reproduce the raw data obtained from the experimental technique used for validation, i.e. the chemiluminescence image from where the O_3 partial pressure surfaces are obtained[25]. Thus, in the absence of measurements of absolute O_3 concentration in the experimental device, a change towards dealing directly with molar fractions was inevitable. The Beta model therefore has the advantage over Alpha, mathematical frameworks aside, of being able to directly employ the experimental data available for model validation.

Finally, a brief note on the behaviors seen in Fig. 3c for $\Delta\chi_{\text{O}_3}(Q)$ is warranted. The resulting curves for the Alpha and Beta models are in contrast to the conclusion drawn in [28]: when comparing between Stokes-Darcy (SD) and Darcy-Brinkman (DB) formulations, the latter showed a closer fit to experimental data, resembling the current Beta model; where the current Alpha model more closely resembles the SD formulation of [28]. That is a testimony of how important grid convergence studies are, as it is clear now that the correlation between experiment and the Alpha model is dependent on the grid. This point will be briefly discussed in Section III A 1.

Moving on with the comparison between Alpha and Beta models, using the DB formulation, we turn to the profiles atop the CL domain. Figure 4 shows both \bar{R}_{O_3} and P_{O_3} profiles along the x axis, for $Q = 250$ and $450 \text{ cm}^3 \text{ min}^{-1}$. Considering first \bar{R}_{O_3} , Fig. 4a, in both cases differences are readily seen between models, with Beta showing narrower peaks and more pronounced structures between peaks. Analyzing one given peak, it is noticeable how the increase in \bar{R}_{O_3} and peak position are virtually the same for both models. The difference thus lies mainly with the decay in \bar{R}_{O_3} after each turn in the Fc, with the Alpha model showing slower decay and, consequently, larger ozone bypass between Fc sections, directly over the land and through the Pm domains. The structures between peaks are likely to be present in both models, seen more prominently for $Q = 250 \text{ cm}^3 \text{ min}^{-1}$ as unresolved local maxima between \bar{R}_{O_3} peaks. These are likely to be connected to recirculation at the first corner of each turn of the Ch domain. The faster decay predicted by the Beta model allows a better view of these local maxima, although only the pre-peak region, while the slower decay predicted by the Alpha model allows only inference of the presence of these local

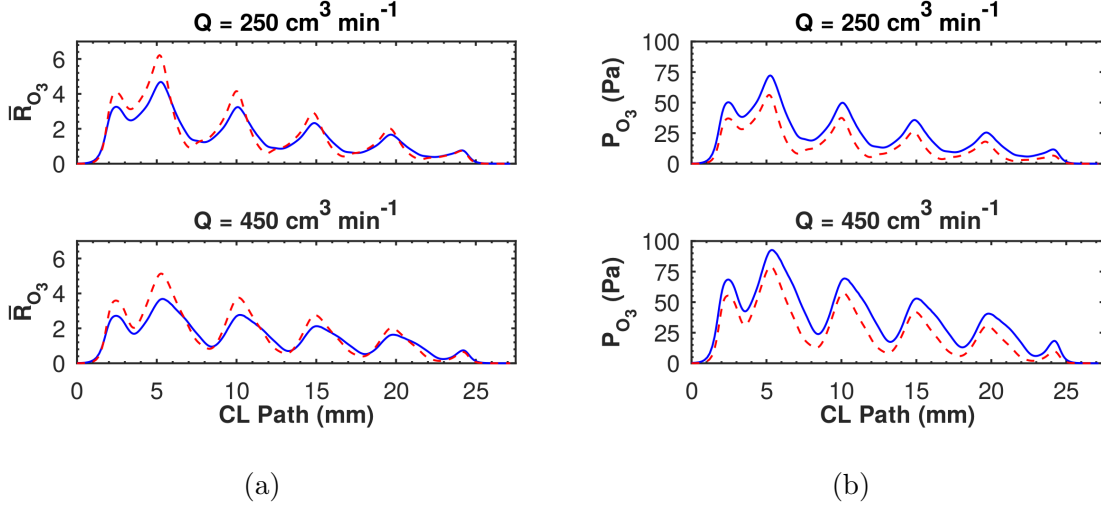


FIG. 4: **(a)** Normalized reaction rate and **(b)** ozone partial pressure profiles, at $Q = 250$ (top) and $450 \text{ cm}^3 \text{ min}^{-1}$ (bottom), for **Alpha** (full) and **Beta** (dashed) models.

maxima *via* the \bar{R}_{O_3} “plateau” between peaks. A similar effect is seen for the Beta model at $Q = 450 \text{ cm}^3 \text{ min}^{-1}$, where the presence of the smaller peaks can be inferred despite being unresolved. For the Alpha model, on the other hand, the presence of the smaller peaks seems to have vanished.

Considering now the P_{O_3} profiles, Fig. 4b, for a qualitative comparison, albeit no less important due to the interest on reactant partial pressure on fuel cells. These profiles are directly related to the \bar{R}_{O_3} ones, and as such, it is seen that P_{O_3} are lower for the Beta model. It can be seen by comparing Figs. 4a and 4b that despite the adsorption step implemented in the Beta model, for the overall ozone decomposition reaction, the P_{O_3} profiles are still proportional to \bar{R}_{O_3} and, consequently, the non-normalized reaction rate R_{O_3} . Thus, the points discussed above translate almost directly to this case, in particular the presence of the local maxima between peaks for the Beta model at $Q = 250 \text{ cm}^3 \text{ min}^{-1}$, albeit not as pronounced as in Fig. 4a. The overall lower values of P_{O_3} predicted by the Beta model are also in line with the results shown in Fig. 3, thus corroborating that the differences between profiles are not just a matter of rate constant values. To strengthen the case, Fig. S12 shows the same P_{O_3} profiles normalized by their respective R'_{O_3} values. In this case, it can be seen that the difference are even larger, further corroborating the idea that changes in P_{O_3} at the CL are due to more than just the magnitude of reaction kinetics.

It should be kept in mind that, in the case of the normalized reaction rate profiles, differ-

ences seen in Fig. 4a are expected to be mainly a consequence of the different mathematical frameworks. Although some influence on the magnitude of the reaction rate constants is to be expected, as is discussed in Section III B, the close results shown in Fig. 3 suggest that such influence is relatively small in this case. Nevertheless, these profiles join the scalar values shown in Fig. 3 as potential validation points, either as \bar{R}_{O_3} or P_{O_3} given the clear proportionality seen in Fig. 4. However, it should be noticed that experimental data currently available does not allow distinction between the Alpha and Beta models (see Fig. 4 of [28]). Such an increase in precision is currently being sought.

Carrying on, we proceed to analyze spatially-resolved data available for both models. Figure 5 shows the surfaces for the same values of Q as Fig. 4a, as well as the differences between Beta and Alpha models. As expected from Fig. 4a, the Beta model shows larger \bar{R}_{O_3} values over the corners of the Ch domain. Similarly, the Alpha model shows larger plumes of \bar{R}_{O_3} at the same regions. In addition, it is now possible to observe that this is the case all over the CL upper surface, being particularly evident in Figs. 5c and 5f. The increase in Q is followed by an increased difference in plume spread and the regions where it is evident, with slightly reduced differences in magnitude. Concerning the differences between peaks seen in Fig. 4a, \bar{R}_{O_3} surfaces provide little additional information, aside from the confirmation that it happens in all turn sections of the Ch domain.

For the final comparison, the P_{O_3} surfaces are shown, for selected values of Q , in Figure 6. It should be kept in mind that comparisons between Alpha and Beta models using P_{O_3} are qualitative in nature, thus it was chosen to normalize the color scales in Fig. 6 by their respective maximum values, in order to avoid quantitative comparisons. Similarly to Fig. 4, a direct relation between \bar{R}_{O_3} and P_{O_3} surfaces is seen, just as expected. Larger ozone plumes are also seen for the Alpha model, particularly for $Q = 450 \text{ cm}^3 \text{ min}^{-1}$. Aside from that, as expected from Fig. 4b, there is little difference between the models. A surface of differences in P_{O_3} could be instructive, as in Fig. 5, however as pointed out the difference in reaction kinetics makes such data misleading, and thus is better left out from the analysis.

Figs. 5 and 6, in particular Figs. 5c and 5f, provide additional insight over a discrepancy between experimental and numerical data reported in [28]. It was seen that, for a k_{app} value that reasonably matched experimental results, the preferred model predicted a narrower ozone plume in much of a given horizontal section of the Ch domain. Here we see that the Beta model predicts a narrower plume, when compared to Alpha, deepening the

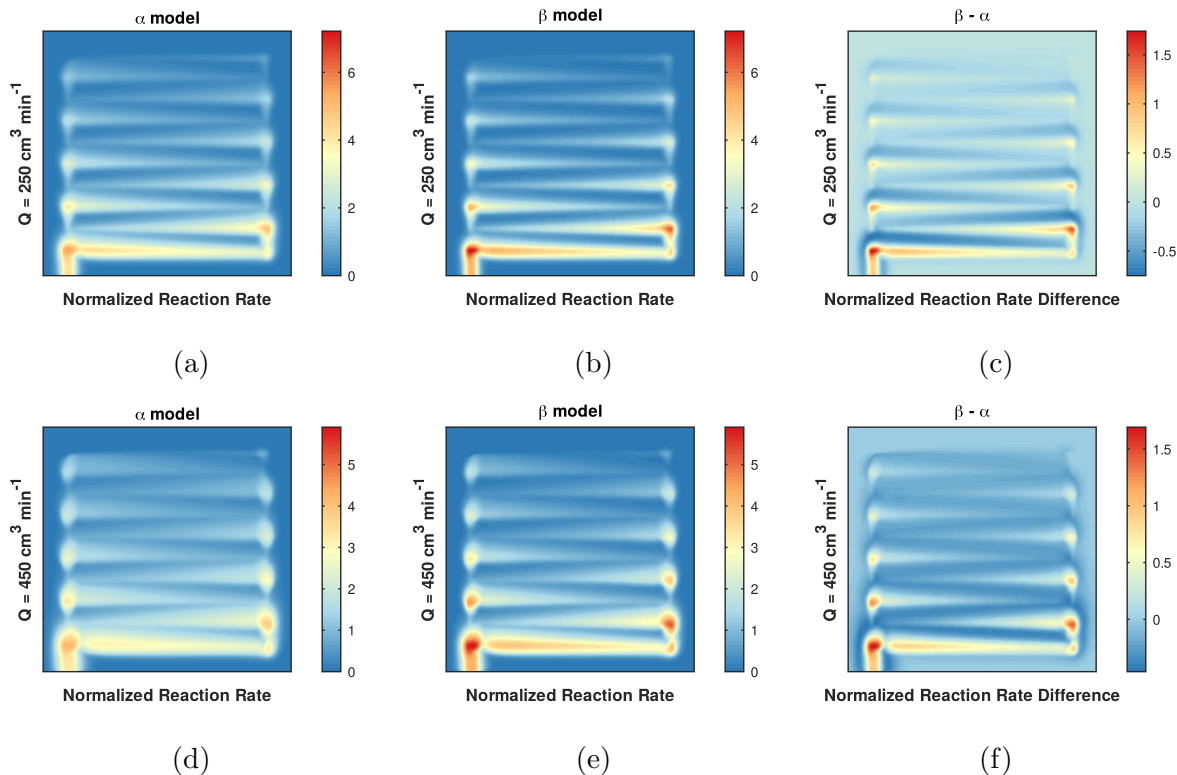


FIG. 5: Normalized reaction rate surfaces for the Alpha (left column) and Beta (central column) models, and the difference between Beta and Alpha models (right column), for $Q = 250$ (top row) and $450 \text{ cm}^3 \text{ min}^{-1}$ (bottom row).

discrepancy between numerical and experimental systems. However, as pointed out above, the precision of the experimental spatially-resolved data offers relatively small constraints to the computational models, thus an improved setup is being sought in order to allow robust comparison with numerical data and, consequently, further improvements to the models.

1. Discussions

Given the comparisons made above, it is clear that, in general, the differences between the Alpha and Beta models are relatively small, in particular with few qualitative differences. The most relevant difference seen, in Fig. 3c, lacks validation power due to the degree of freedom assigned to the reaction rate constants. To complicate matters, the estimated error for the Beta model (un)comfortably puts both experimental and the Alpha model's data within uncertainty bounds (see Figs. S13 and S14), specially more so if one assumes the

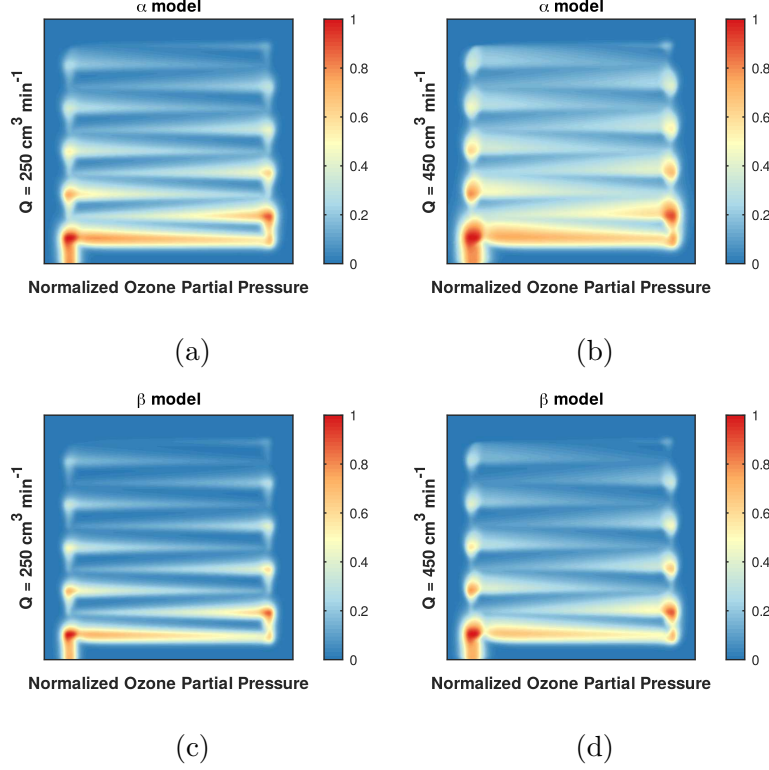


FIG. 6: Normalized ozone partial pressure surfaces for the Alpha (top row) and Beta (bottom row) models, for $Q = 250$ (left column) and $450 \text{ cm}^3 \text{ min}^{-1}$ (right column).

discretization error of Alpha is of the same magnitude as Beta. Variables that show error compensation and thus would be useful for validation, such as $K' = \Delta\chi_{\text{O}_3}/R'_{\text{O}_3}$ and R'_{O_3} , lack experimental data. Therefore, two major issues outside the mathematical framework need to be further considered before actual validation may be pursued: i) discretization error, i.e. the mesh refinement, and ii) the availability of experimental data. While both demand time and resources, they are currently being sought.

In the meantime, there are some shortcomings and approximations in the Beta model that deserve some clarifications. These have been brought up before, namely the Fickian diffusion coefficient for O_3 , the use of an O_3 /air mixture, and the coupling between free, porous media and Knudsen diffusion regimes. In addition, there is the insight regarding the behavior of $\Delta\chi_{\text{O}_3}$ when compared to the experimental data and previously published results[28]. Concerning the first point, we are not aware of the existence of measurements or calculations of the binary diffusion coefficients for ozone in any mixture. Following the rationale provided in Section II A 2, i.e. that the concentration of O_3 is small and the relative

concentrations of N_2 and O_2 are constant, and given such limitation, it seems that there is little else to be done at this moment other than directly using the single-component diffusion coefficient.

Regarding the mixture, it was mentioned in Section II A 2 that the Beta model uses a simplified formulation for the fluid’s species. As reported in [25], the experimental device used O_3 -enriched air as working fluid, and thus a first approach would be to model its species as a $\text{O}_3/\text{O}_2/\text{N}_2$ fluid. However it is known that only the O_3 is reactive in the experimental conditions used, and that $\chi_{\text{O}_3} \sim 10^{-3}$ at the inlet. Thus one might consider that χ_{O_2} and χ_{N_2} are approximately constant. Indeed, this is the same rationale behind the diluted species approach used previously[28]. This has two implications, namely i) the fluid’s properties, i.e. viscosity and density, are largely due to O_2 and N_2 , and thus very much like air; and ii) the chemical driving forces acting on O_3 are mainly given by $\nabla\chi_{\text{O}_3}$ in a bath of air. Therefore, an alternative would be to model the fluid using effective “air” molecules along with O_3 . In this way, one saves computational resources while at the same time reducing the hardships of measuring, or calculating, the binary diffusion coefficients for each pair of species in the fluid at varied concentrations.

Additional simulations were carried out using the proper $\text{O}_3/\text{O}_2/\text{N}_2$ mixture, however still using the same diffusion coefficient of Table II for $\text{O}_3 - \text{O}_2$ and $\text{O}_3 - \text{N}_2$ pairs. Section SII of the SM[40] provides additional information on the simulations, as well as the results (Figs. S1 to S3). While a reduced geometry was used for these simulations (shown in Fig. 2), they are compared against results for the O_3/air mixture using the same geometry. For all cases, scalar variables, O_3 profiles and surfaces, the differences are negligible, particularly when considering the estimated discretization errors. Notably, Fig. S3 shows the difference in \mathbf{P}_{O_3} between mixtures, where it is shown that, while a pattern can be seen, indicating a clear physical effect, the differences in O_3 partial pressure are ~ 0.1 Pa, which amounts to $\sim 0.1\%$ of the values observed. Thus, considering both the error estimates and the order of magnitude of the experimentally relevant variables, it is safe to assert that, for the moment, the O_3/air approximation is adequate.

Concerning the coupling between diffusion modes, it was pointed out in Section II A 2 that it was not entirely clear at this point. By that it is meant the mathematical relation that expresses the effective diffusion coefficient that would be measured in a macroscopic device, D_i . Here it was chosen to apply a correction to the free diffusion coefficient, due to the porous

media, which was then coupled to Knudsen diffusivity. Physically speaking, it means that regardless of the distribution of characteristic lengths in the pore network, the existence of such network and its tortuosity affects molecular diffusion, while the Knudsen regime exists alongside it. In appropriate circumstances, the Knudsen regime becomes dominant ($\text{Kn} \sim 1$ and above), and the macroscopic description of the porous medium, using porosity and tortuosity, breaks down.

In order to assess the importance of this effect in the Beta model, additional numerical simulations were carried with the reduced geometry mentioned above and the O_3 /air mixture. This was chosen, in addition to the justification presented above, as it becomes straightforward to apply different coupling schemes and to verify the contributions of each diffusion mode, given that in such case there is only one entry in the Maxwell-Stefan diffusion matrix, and thus a single generalized Fick diffusivity is calculated. Additional information can be found in Section SIII of the SM[40], and the simulations' results are shown in Figs. S4 to S9. Five settings were tested, although due to limitations of the software, only two couplings involving all processes were considered, namely the one described in Section II A 2 and one where the porous media correction is applied after coupling free and Knudsen diffusivities. The results show that the most important effect, for the simulated device, is the porous media correction. This is in line with previous work[28], where it was argued that the low Knudsen numbers ($\text{Kn} \sim 10^{-3} - 10^{-2}$) calculated for the device implied small contributions from Knudsen diffusion. Indeed, Figs. S8 and S9 shows the differences in \mathbf{P}_{O_3} between the chosen coupling, Eq. 12, and the other four settings, where a clear spatial pattern and larger partial pressure difference are seen when the alternative setting lacks porous media corrections. The differences due to a lack of Knudsen diffusion are of the same order as the difference between both settings including all effects ($\Delta P_{\text{O}_3} \sim 0.01$ Pa), however showing a noisy spatial pattern, while the latter shows a clear pattern. Considering the brief discussion given in [28], concerning differences between concentrated and diluted species approaches, these results suggest that concentration and pressure gradients, considered in the Maxwell-Stefan formulation, are also more important than Knudsen diffusion for the experimental device under consideration.

Finally, a brief discussion on the difference in behavior between Alpha and Beta models for $\Delta\chi_{\text{O}_3}(Q)$. As pointed out in Section III A, the behavior of the Alpha model resembles the one using the SD formulation in [28], while the Beta model resembles the one for the DB

formulation. To be clear, here both Alpha and Beta models use the DB formulation for free and porous media flow. This raises the question if, given the new mesh and solver schemes, the DB is actually superior to the SD formulation as previously claimed.

This was investigated, and it is given in Section SIV.C of the SM[40], with results shown in Figs. S15 to S20. Briefly, it is seen that, for the current mesh, the fluid flow formulation affects the Alpha and Beta similarly, with overall differences between SD and DB formulation being small and following the outline previously established in [28]. For the scalar response variables (Figs. S15 and S16), the SD formulation predicts slight lower values for K' , $\Delta P/P_{\text{in}}$, and ΔP , while predicting slightly higher values for R'_{O_3} , where it should be noticed that it affected the Beta model slightly more strongly, indicating larger differences at higher Q . Noteworthy results are seen for λ and $\Delta\chi_{\text{O}_3}$. For λ , the SD formulation predicts lower values for both Alpha and Beta models as well, however the differences are significantly larger than for other response variables, with the Beta model showing larger differences for higher Q . Considering the error estimates in Fig. S14, even relatively small gains in precision and additional data for higher Q might be able to provide significant distinction between models. For $\Delta\chi_{\text{O}_3}$, and consequently λ' , the SD formulation affects each model in slightly different ways: for the Beta model, again a slight increase in values is seen; however, for the Alpha model, a small increase in the slope of the curve is seen. In this way, the difference between formulations, and models using a given formulation, increases with Q . This provides another opportunity to allow significant distinction between formulations and/or models in the future with relatively small investment in precision and larger parameter ranges.

Considering now the spatially-resolved response variables, notable differences are seen for $U(z)$ and P_{O_3} . Concerning the U z -profiles (Fig. S17), in the Pm domains there is a significant mismatch between the SD and DB formulations. A comparison with Figure 5 of [28] will not only show a much better-resolved U profile for all frameworks, but also closer U values between formulations. The discrepancy lies in the discontinuities in U at domain interfaces and the profile inside the Pm domains. The discontinuities between the Ch and MPS domains as well as the difference in profile close to the upper CL boundary were already noted in [28]. The boundary conditions involved in both the coupling between free and porous media flow and with domain walls knowingly differ between the SD and DB formulations[20, 21, 32], and given deeper scrutiny might be improved or even reconciled. The U jump between different materials, however, is unlikely to be a proper description

of reality, or an artifact due to a coarse mesh, as there is evidence of proper continuity in U when using Darcy’s law (see for instance [48]). This is possibly an artifact of how the software couples free and porous media flow, perhaps dealing with differences in porosity and permeability in the same way no matter the case. Nevertheless, these results are interpreted as evidence that the SD formulation, as it has been applied here and using the COMSOL Multiphysics® software, provides a poorer description of coupled free and porous media flow than the DB formulation.

Considering the P_{O_3} and \bar{R}_{O_3} profiles (Fig. S18), the most prominent differences are well in line with [28], with the SD formulation showing overall values of P_{O_3} and larger plumes after turns for both models. It is noteworthy that all frameworks show distinctions that might be amenable for validation, for instance employing the SD formulation with the Beta model raises the overall P_{O_3} values to those of the Alpha model employing the DB formulation. However, the local minima in the profiles, i.e. the sections after a given turn and approaching the following one, differ between fluid flow formulations: the DB approach predicts a lower, short minima right after the local maximum, followed by a plateau preceding the next rise; the SD formulation, on the other hand, predicts a single, longer minimum between peaks. This, it should be reminded, for the a given model, say Beta, and same values for the reaction rate constants. This follows after the results of [28], with clearer differences that strengthen the hypothesis that they are caused by the fluid flow formulation, and the additional information that they are not artifacts of a diluted-mixture approach to species transport. With increased computational and experimental precision, these results will prove to be important in further validating and improving the mathematical models. The same reasoning seems to apply to the \bar{R}_{O_3} profiles, although smaller differences are seen between the Beta model using the DB formulation and the Alpha model using either fluid flow formulation. The most notable difference in this case lie on local minima between peaks, where, for the Beta model at higher Q , there is a significant shift forward when changing from the DB to the SD formulation. The differences are rather small, however, and it is unclear if it would provide any advantage over the P_{O_3} profiles. It could be argued that the \bar{R}_{O_3} profiles emphasize changes in reaction kinetics, mixing the effects with those of changes in the fluid flow formulation. In this way, these may be more suited to investigate the reaction kinetics after the debate between SD and DB formulation is settled.

Taking into account the discussions above concerning known limitations of the Beta

model, it is evident that despite the advances achieved in the mathematical formulation, there are additional points that demand further improvements. A Gamma model would need to consider the anisotropy and inhomogeneity of porous media, as well as solve the conundrum involving Knudsen diffusivity. Perhaps the dusty-gas model used in solid oxide fuel cell modeling might solve the latter [5, 7]. Ideally, in order to further reduce the gap between the prototype PEFC and an actual device, heat transport should also be considered, as well as two-phase flow. That would demand modifications in the experimental setup, as well as additional data on the properties of the materials and species involved. Moving away from phenomena under broad scrutiny, there is the discrepancy between ozone plume sizes to solve, briefly discussed in Section III A (see also Part II and [28]). In this case, two hypothesis are currently under consideration, i) inhomogeneous mechanical deformation of the MPS, and ii) molecular slip velocities. The first stems from the way PEFC devices are usually sealed, using screws distributed around the core of the device, while the second is the breakdown of the no-slip boundary condition, which asserts that $\mathbf{u} = 0$ at the interface between solid and fluid. It appears that both are known to play a role in PEFCs, and some work has been done on both for different reasons (see [22, 49–51] as well as [52] and references therein; and [53–56], respectively). How important would they be in actual fuel cells, however, appears little understood, as the complexity of including non-linear solid mechanics and the molecular interplay between fluid and solid species in already hard-to-solve differential equations is likely a powerful factor stymieing such research. Nevertheless, until it is done and calculated, one can only speculate.

B. Parametric Study of Reaction Rate Constants

For our final task, as described in Section II C, a parametric study on the reaction rate constants, k_1 and k_2 , associated with ozone adsorption and decomposition reactions respectively, was carried out. As pointed out in Section III A, when the discussing the difference in behavior of $\Delta\chi_{\text{O}_3}$ for the Alpha and Beta models (Fig. 3), these are degrees of freedom in the Beta model, as is k_{app} for the Alpha model, and no additional empirical or theoretical information is currently known by the authors. Hence the need for an assessment of the solution of the computational models as function of these parameters, as was done for the Alpha model in [28].

We start the analysis with a consideration on the computational models under analysis. Such a parametric study is dependent on the mesh used for the calculations. This is clear from the changes in $\Delta\chi_{\text{O}_3}$, as pointed out in Section III A 1, as well as from the grid convergence study carried out in Part 2. For instance, when considering the parametric study carried out for k_{app} for the Alpha model[28], it was shown that, for the mesh used then, values close to $k_{\text{app}} = 250 \text{ s}^{-1}$ are a close fit to the experimental data available[28]. This value was later refined to the one currently in use, $k_{\text{app}} = 256.15 \text{ s}^{-1}$. However, as seen in Fig. 3, when using a finer mesh $\Delta\chi_{\text{O}_3}$ changes both quali- and quantitatively, thus a more appropriate value for k_{app} could be calculated.

With that in mind, we begin with a preliminary result: the Beta model did not converge for $k_1 = 10^4 \text{ s}^{-1}$, already showing difficulties for 10^3 s^{-1} . While this could potentially be solved by adjusting the numerical solvers, results shown below suggest that it was due to excessive consumption of ozone, which could lead to unrealistic solutions. In this way, the parametric study was able to probe the following ranges: $k_1 \in [1, 10, 10^2, 10^3] \text{ s}^{-1}$ and $k_2 \in [10^{-1}, 1, 10, 10^2, 10^3] \text{ s}^{-1}$.

Moving to the results proper, Figure 7 presents the scalar response variables: the $K' = \Delta\chi_{\text{O}_3}/R'_{\text{O}_3}$ ratio, as well as the individual variables, and the stoichiometries λ and λ' . Analyzing first the individual variables, $\Delta\chi_{\text{O}_3}$ (Fig. 7a) behaves as expected, with increased values as both k_1 and k_2 increases. However it becomes clear that k_1 is much more important in defining the absolute value of $\Delta\chi_{\text{O}_3}$, with k_2 mainly contributing at higher Q , providing fine adjustment to the behavior of the curve (see Fig. S21 for the relative change in $\Delta\chi_{\text{O}_3}$ as k_2 increases for fixed k_1). In addition, it is seen that the increase in $\Delta\chi_{\text{O}_3}$, when moving from $k_1 = 10^2$ to 10^3 s^{-1} , is significantly smaller than observed for other intervals. This is also expected, as there is a limit to the mass transport from the Ch to CL domains given intrinsically by Q and the idiosyncrasies of the device (characterized by the Damköhler numbers).

The R'_{O_3} (Fig. 7b), on the other hand, shows more nuanced results. Up until $k_1 = 10^2 \text{ s}^{-1}$ the data conforms with expectations and Fig. 7a. However, for $k_1 = 10^3 \text{ s}^{-1}$, there is a sudden decrease in R'_{O_3} values. This is interpreted as a lack of reactants reaching the upper CL boundary, where R'_{O_3} is calculated, given the high k_1 value. Indeed, Fig. S22 of the SI, which shows the reaction rate integrated over the CL domain, corroborates this reasoning by showing a trend compatible with Fig. 7a, i.e. with values for $k_1 = 10^3 \text{ s}^{-1}$ being higher

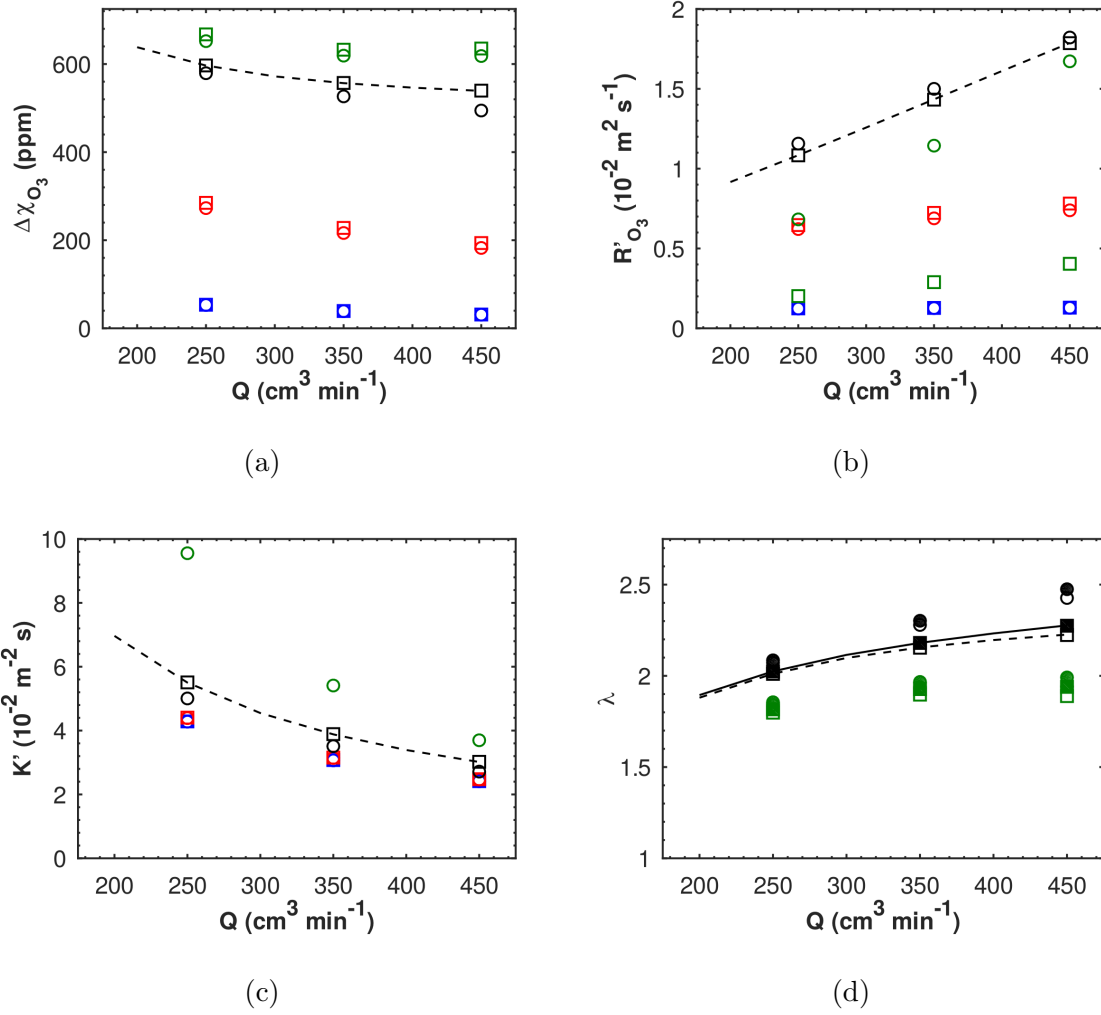


FIG. 7: Scalar variables as function of the inlet flow rate for the Beta model, using different combinations of k_1 and k_2 : (a) $\Delta\chi_{O_3}$, (b) R'_{O_3} , (c) $K' = \Delta\chi_{O_3}/R'_{O_3}$, and (d) λ (empty) and λ' (full). Different colors map the values of k_1 : 1, 10, 10², and 10³ s⁻¹; while the values of k_2 are mapped by different symbols: 10⁻¹ (o) and 10³ s⁻¹ (□). The Beta model, using the same reduced geometry, is shown as reference (dashed and full lines), with k_1 and k_2 given in Tab. III.

than all others. This naturally explains the results shown in Fig. 7c, for the K' ratio, which shows significantly higher values for $k_1 = 10^3$ s⁻¹ in comparison to $k_1 = 10^2$ s⁻¹, whereas the remaining results for $k_1 \leq 10^2$ s⁻¹ shows similar values and trends in Q (see Fig. S22 for the full range of k_1 and k_2). Interestingly, the values of such a ratio obtained when using the reaction rate integrated over the CL domain, shown in Fig. S22, are very close regardless of

the values of k_1 and k_2 .

The stoichiometries λ and λ' (Fig. 7d) are shown for $k_1 \geq 10^2 \text{ s}^{-1}$, since the range for $k_1 \leq 10 \text{ s}^{-1}$ was significantly larger and out of touch with experimental results (see Fig. S23 for the full range). Both λ and λ' shows the same trends with increasing k_1 and k_2 : reduced values and slope as k_1 increases, and for a given mean value, reduced slope as k_2 increases. It should be pointed out that both λ and λ' show good sensitivity towards k_2 , although slightly smaller than K' , when considering the full range of k_2 investigated. What is truly noteworthy, however, is that, relative to the error estimates from Part 2 (shown in Fig. S13), λ and λ' shows much larger sensitivity than any other scalar response variable, particularly at the high end of the Q range where it is one order of magnitude larger. The stoichiometries thus provide an excellent opportunity to constrain the values of k_2 , with other variables providing constraints for k_1 . Thus, with further improvements in both computational and experimental precision, information on the reaction kinetics may be available without the need to delve in the complexities of modeling transient effects.

Moving forward, we turn now to the profiles, where once again focus will be given to the \bar{R}_{O_3} profiles. Figure 8 shows the \bar{R}_{O_3} profiles for selected values of k_1 , k_2 , and Q . A similar trend to Fig. 7b is seen for \bar{R}_{O_3} magnitude in Fig. 8a, when comparing different k_1 and k_2 values, including the inversion seen for $k_1 = k_2 = 10^3 \text{ s}^{-1}$. Contrary to Fig. 7, however, Fig. 8a shows that, for $k_1 \gtrsim 10^2 \text{ s}^{-1}$, the value of k_2 shows greater influence on \bar{R}_{O_3} than for the scalar variables, thus providing the possibility of additional validation for k_1 and k_2 . Fig. 8b provides a full comparison between values of k_2 for $k_1 = 10^2 \text{ s}^{-1}$, showing the relative difference between increasing values of k_2 , where it can be seen that the largest changes are seen when moving from $k_2 = 10^{-1}$ to 1 s^{-1} , with significantly less changes for $k_2 = 1$ to 10 s^{-1} , and virtually no changes for $k_2 = 10$ to 10^2 s^{-1} ($\Delta \bar{R}_{\text{O}_3} \sim 0.1\%$). Therefore, while there is an opportunity for the validation of k_2 , the range of values is somewhat limited when using \bar{R}_{O_3} profiles, regardless of the precision available from either experimental or computational data.

The partial pressure profiles shows similar results to Fig. 8 and are shown in Fig. S24a. While the observed trends are similar, comparing P_{O_3} values for model runs with different values of k_1 and k_2 demands some caution, as the situation is similar to the comparison between Alpha and Beta models (Fig. 4). Nevertheless, the relative difference in P_{O_3} profiles for increasing values of k_2 , shown in Fig. S24b for $k_1 = 10^2 \text{ s}^{-1}$, shows very similar sensitivity

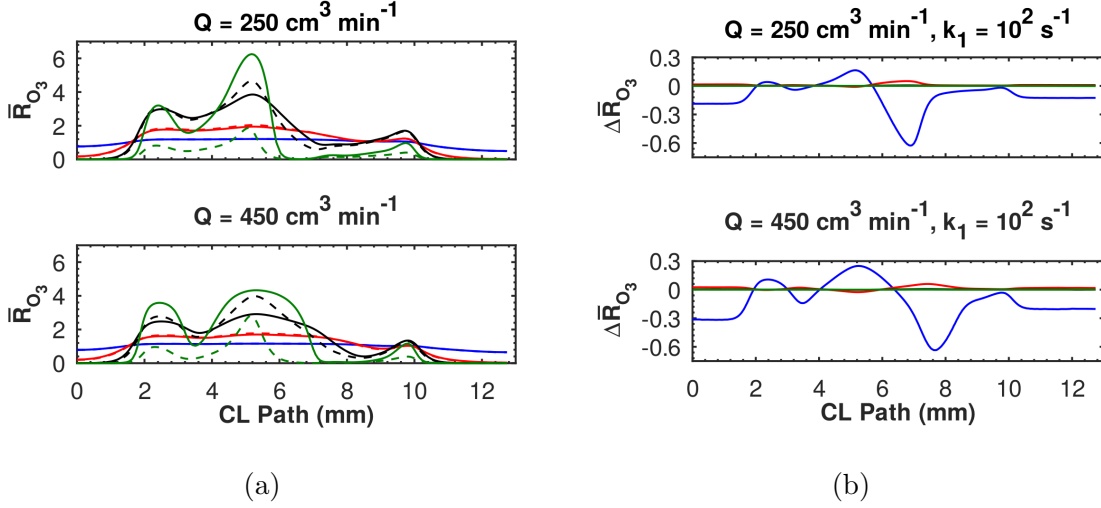


FIG. 8: Profiles associated with the normalized reaction rate, at $Q = 250$ (top) and 450 cm³ min⁻¹ (bottom), for selected values of k_1 and k_2 . **(a)** Normalized reaction rate profiles, with $k_1 = 1, 10, 10^2$, and 10^3 s⁻¹; and k_2 : 10^{-1} (full lines) and 10^3 s⁻¹ (dashed lines). **(b)** Relative difference between profiles for increasing values of k_2 , using

$$k_1 = 10^2 \text{ s}^{-1}: k_2 = 1 - k'_2 = 10^{-1}, k_2 = 10 - k'_2 = 1, k_2 = 10^2 - k'_2 = 10, \text{ and} \\ k_2 = 10^3 - k'_2 = 10^2.$$

to the absolute value of k_2 as the \bar{R}_{O_3} profiles of Fig. 8. Thus, while a comparison between model runs with different k_1 and k_2 values might prove redundant given \bar{R}_{O_3} profiles, the P_{O_3} profiles are currently available from experimental data, providing an excellent opportunity for validation of the k_1 and k_2 values in addition to the scalar response variables of Fig. 7.

Finally, we move on to the spatially-resolved data, where focus will naturally be given to $\bar{\mathbf{R}}_{O_3}$ surfaces, in particular to $k_1 = 10^2$ s⁻¹, since Fig. 8 suggests $k_1 \gtrsim 10^2$ s⁻¹ for the experimental device. Figure 9 shows $\bar{\mathbf{R}}_{O_3}$ surfaces, for $Q = 250$ and 450 cm³ min⁻¹, for $k_1 = 10^2$ s⁻¹ and $k_2 = [10^{-1}, 10, 10^3]$ s⁻¹. Additional surfaces may be found in the SI (Figs. S25 to S28). The trend observed as k_2 increases follows what has been discussed above, with $\bar{\mathbf{R}}_{O_3}$ showing virtually no changes when further increasing k_2 from 10 to 10^3 s⁻¹. There is novel information, however, in Fig. 9 (and Figs. S25 to S28): k_2 apparently has an important role in ozone dispersion within reactant plumes. This is clearer for $Q = 450$ cm³ min⁻¹, where it can be seen that $\bar{\mathbf{R}}_{O_3}$ is more homogeneously distributed around the Ch domain region for $k_2 = 10^{-1}$ than for 10 s⁻¹. Fig. S29 shows these same surfaces normalized by their respective maximum values, reinforcing the point. This suggests that, for a given value of

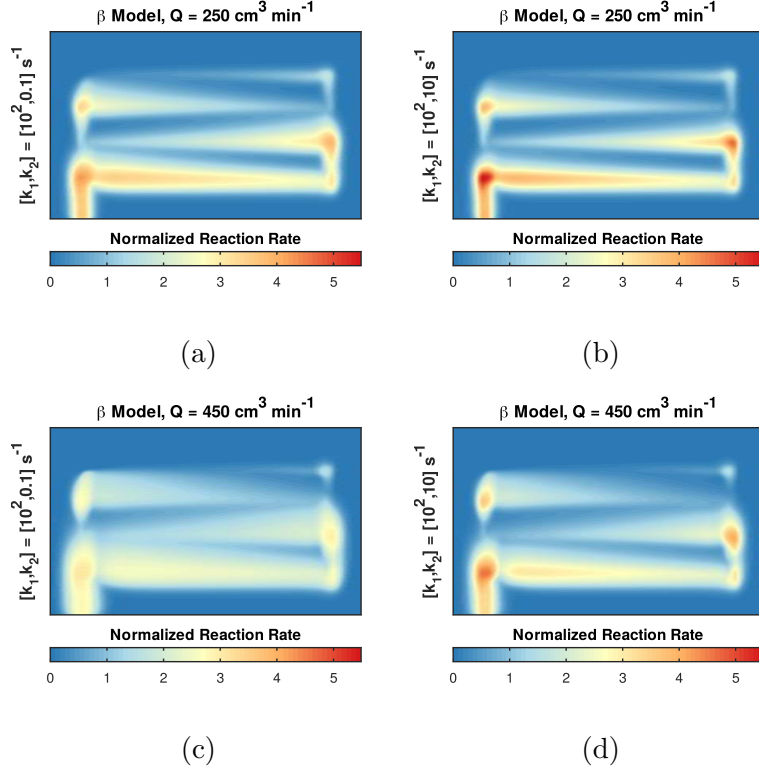


FIG. 9: Normalized reaction rate surfaces for $k_1 = 10^2 \text{ s}^{-1}$, with $Q = 250$ (top row) and $Q = 450 \text{ cm}^3 \text{ min}^{-1}$ (bottom row), and $k_2 = 10^{-1}$ (left column) and 10 s^{-1} (right column).

k_1 , k_2 modulates the gradient $\nabla \bar{R}_{\text{O}_3}$ within the reactant plume, whereas k_1 strongly impacts on the spread of the plume itself. It must not be misunderstood that each reaction, and consequently each reaction rate constant, is solely responsible for either aspect of $\bar{\mathbf{R}}_{\text{O}_3}$, as it is very likely that both k_1 and k_2 play a role in the final, steady-state shape of $\bar{\mathbf{R}}_{\text{O}_3}$. But rather that, given the mechanism used to describe the ozone-coumarin interaction, experimental data on the overall spread of the reaction plume may be used to validate k_1 , while data on the gradient may be used to validate k_2 .

Considering now the \mathbf{P}_{O_3} surfaces, Figure 10 shows the surfaces corresponding to Fig. 9, i.e. for $k_1 = 10^2 \text{ s}^{-1}$, $k_2 = 10^{-1}$ and 10 s^{-1} , and $Q = 250$ and $450 \text{ cm}^3 \text{ min}^{-1}$. Additional surfaces may be found in the SI (Figs. S30 to S33). Once again the trend of \mathbf{P}_{O_3} follows that of $\bar{\mathbf{R}}_{\text{O}_3}$, keeping in mind the caution one must take in comparing results with different values of k_1 and k_2 . In this case, Fig., 10 shows absolute values of P_{O_3} , albeit for shared color scales, in order to reach back towards the experimental results (such as shown in [25, 27, 28]). Thus, while the trend follows that of Fig. 9, it should be noticed that it is reversed: higher

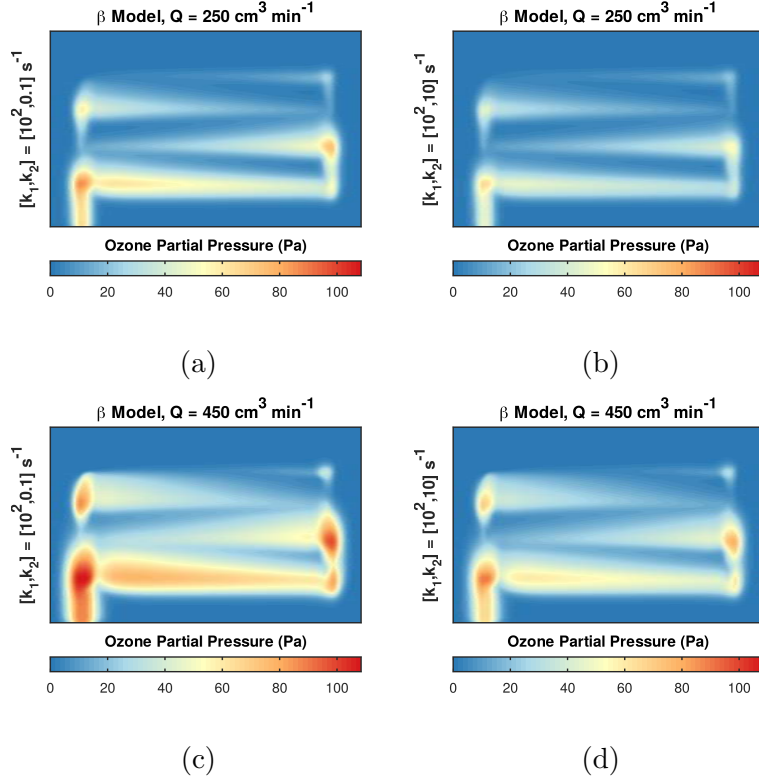


FIG. 10: Ozone partial pressure surfaces for $k_1 = 10^2 \text{ s}^{-1}$, with $Q = 250$ (top row) and $Q = 450 \text{ cm}^3 \text{ min}^{-1}$ (bottom row), and $k_2 = 10^{-1}$ (left column) and 10 s^{-1} (right column).

values of k_2 leads to smaller gradients in P_{O_3} , i.e. more homogeneous plumes. It should also be noticed that the effect is somewhat smaller than seen in Fig. 9, as further suggested by Fig. S29. Thus, while it may be more intuitive to look at \mathbf{P}_{O_3} surfaces for qualitative information and, perhaps, diagnostics; $\bar{\mathbf{R}}_{\text{O}_3}$ surfaces might provide a more stringent test for model and parameter validation.

Wrapping up, the range of k_1 and k_2 explored in the parametric study was shown to cover a wide range of device responses, from negligible O_3 usage, to a significant reactant drop. At the lower end of the k_1 range, the reduced geometry uses 4.4% to 2.6% of the inlet O_3 molar fraction, averaged over the range of k_2 , while at the upper end it averages to 55% to 53%. Through the K' ratio we can estimate the equivalent reactant drop for the full geometry (see Part 2 for justification on this), which at $k_1 = 10^3 \text{ s}^{-1}$ would be > 1 for all values of k_2 and Q except for one ($k_2 = 10^{-1} \text{ s}^{-1}$ and $Q = 450 \text{ cm}^3 \text{ min}^{-1}$). Considering the proximity between the Beta model, using the full geometry, and the available experimental results, we consider safe to state that $k_1 < 10^3 \text{ s}^{-1}$ for the present mathematical formulation.

The scalar response variables also suggest that $k_1 > 10 \text{ s}^{-1}$, given the range of k_2 explored and the relatively low sensitivity towards changes in its value. One noteworthy exception is the stoichiometries λ and λ' , which show good sensitivity towards changes in k_2 at the high end of the Q range. From the comparison with the available data (Fig. 3b), and the behavior of λ with k_2 (Fig. 7d), it seems that $k_1 \lesssim 10^2 \text{ s}^{-1}$ and $k_2 \gtrsim 10^3 \text{ s}^{-1}$. The profiles also appear to show good sensitivity towards k_2 for $k_1 = 10^2 \text{ s}^{-1}$, however the current lack of high-quality experimental data does not allow a finer constraint on k_2 than already obtained with the scalar variables. Finally, the parametric study allowed us to identify how each reaction rate constant appears to influence the response surfaces, viz. the \bar{R}_{O_3} and P_{O_3} surfaces. In the range of k_1 and k_2 explored, it seems that k_1 , associated with the adsorption reaction, controls the spread of the O_3 plume, while k_2 , associated with the decomposition reaction, controls the homogeneity of the plume. Thus we suggest that spatially-resolved data on the reactant partial pressure may be used to improve the constraints on k_1 , while data on the local gradient of P_{O_3} might be used to constrain k_2 . While the currently available experimental results do not allow tighter constraints on k_1 or an upper bound of k_2 , this study has helped to identify opportunities for future rounds of model validation following improvements in both the experimental and computational setups.

IV. SUMMARY

Work is presented concerning progress on the numerical modeling of a prototype polymer electrolyte fuel cell (PEFC)[25], building on previously published work[28]. Known limitations of the original model, Alpha, were addressed in order to increase fidelity with the current understanding of fuel cell devices, resulting in the Beta model. In this part, both mathematical frameworks are compared, and approximations and shortcomings are discussed. Having established the differences between models, a parametric study is carried out for Beta in order to assess the effects of the order of magnitude of each reaction rate constant on the global results. In part II, a grid convergence study was carried out in order to provide an estimate to the discretization error intrinsic to the Beta model.

Response variables, some of experimental interest, are compared between the Alpha and Beta models, viz., the reactant drop $\Delta\chi_{\text{O}_3}$; a proxy for the total reaction rate, R'_{O_3} ; the ratio between the two, $K' = \Delta\chi_{\text{O}_3}/R'_{\text{O}_3}$; the real and apparent stoichiometries, λ and

λ' respectively; and spatially-resolved variables, in the form of profiles and surfaces along the catalyst layer (CL), given by reactant partial pressure P_{O_3} and normalized reaction rate \bar{R}_{O_3} . It should be noticed that each model has degrees of freedom associated to the reaction kinetics, despite efforts to choose response variables that minimize such effects, thus care should be taken when drawing strong conclusions from comparisons. From the scalar response variables, relatively small differences are seen between models, although $\Delta\chi_{\text{O}_3}$ and λ' show noteworthy results. In both cases, the Beta model shows a better fit to the available experimental data than the Alpha model, in particular for $Q \geq 350 \text{ cm}^3 \text{ min}^{-1}$. For the spatially-resolved variables, \bar{R}_{O_3} profiles and surfaces show differences between models that might be distinguishable through experimental validation.

Shortcomings of the model comparison and the mathematical framework of the Beta model are discussed. Concerning model comparison, it should be noted that, given the estimated error of the numerical data in Part 2, the results shown lack validation power, as both models and experimental data are well within error bounds of each other. Adding uncertainties in parameterization, these results call for additional experimental data and denser meshes (i.e. more computational resources) in order to be able to accurately distinguish between models, providing further insight into the physical phenomena underlying PEFC devices. In addition, an apparent divergence from earlier results was also addressed, where the Alpha model, at the current mesh and solver schemes, differs from previously published results[28]. New results using the Stokes-Darcy (SD) and Darcy-Brinkman (DB) formulations, with both Alpha and Beta models, show similarities between formulations for a given model, with both models affected similarly. Some response variables do show differences that might be significant when comparing to experimental results, in particular $\Delta\chi_{\text{O}_3}$, and consequently λ' , and P_{O_3} profiles. Considering the differences seen and the current errors estimates for both computational and experimental results, it is reasonable to expect that small gains in precision should be enough to allow proper distinction between fluid flow formulations with a range of Q similar to the explored here. Finally, improving on previous results[28], flow speed profiles along the thickness of the Pm domains show a smoother profile for the DB formulation in both models. These differences are largely understandable when considering known differences in free and porous media flow coupling and wall boundary conditions. On the other hand, SD flow speed profiles show a discontinuity between MPS and CL domains, which is suggested to be an artifact from the software's approach when

coupling media with different porosity and permeability. Flow speed profiles are taken as increased evidence that, for the prototype PEFC device under consideration and the way it has been modeled, the Beta model using the DB formulation provides a better description of the experimental data available.

Concerning the mathematical framework of the Beta model, known approximations and uncertainties in the model were addressed and analysed, namely the use of Fick diffusivity for O_3 despite the Maxwell-Stefan formulation, the use of an approximated O_3 /air mixture, and the coupling between free, porous media, and Knudsen diffusion. While for the Fick diffusion coefficient there is little to be done about at the moment, the mixture and coupling between diffusion modes were investigated. It is shown that there is a negligible difference, considering the error estimates and order of magnitude of the experimental data, between the approximate O_3 /air and the proper $O_3/O_2/N_2$ mixtures. The different coupling between diffusion modes also shows negligible differences, however it is shown that the main factor affecting results is the presence of porous media correction, while the Knudsen regime appears to be of little significance for the current device.

Finally, a parametric study of the reaction rate constants k_1 and k_2 , associated with O_3 adsorption and decomposition reactions, was carried out. Given the degrees of freedom due to the lack of information on these reactions, it is important to establish the range of responses the model can provide given a variation of k_1 and k_2 . The study comprised the ranges $1 \leq k_1 \leq 10^3 \text{ s}^{-1}$ and $10^{-1} \leq k_2 \leq 10^3 \text{ s}^{-1}$, where the Beta model used $k_1 = 10^2$ and $k_2 = 10 \text{ s}^{-1}$, and with $k_1 = 10^4 \text{ s}^{-1}$ failing to converge. The chosen range was shown to cover negligible reactant usage up to unreal projections of the fraction of reactant used > 1 . In addition, the results show that k_1 largely controls the order of magnitude of the chosen response variables, with k_2 typically providing finer control, being particularly important at high Q . From comparisons with the Beta model, using $k_1 = 10^2$ and $k_2 = 10 \text{ s}^{-1}$, and its known good correlation with the available experimental data, the parametric study was able to constrain the reaction rate constants to $10 < k_1 < 10^3 \text{ s}^{-1}$, with $k_1 \approx 10^2 \text{ s}^{-1}$ showing good fit, and $k_2 \gtrsim 10^3 \text{ s}^{-1}$. While the range of values is somewhat broad, the study also identified opportunities for further validation of the Beta model’s reaction kinetics, viz., the stoichiometries λ and λ' , and the P_{O_3} profiles at the CL.

All the shortcomings and opportunities identified in this work would guide a future Gamma model regarding parameterization and whether to include additional features, such

as solid mechanics, improved porous media description and fluid flow formulations; in order to settle existing questions and, thus, further reduce the gap between experimental and computational results. Given the relatively simplicity of the model, being able to uncouple species and momentum transport from charge and heat transport and still maintain similarity to actual PEFC devices, we believe there is much to be gained from further refining this coupled experimental-numerical approach to fuel cell research.

ACKNOWLEDGMENTS

O.B. acknowledges the Fundação de Apoio à Universidade de São Paulo, FUSP, grant #2968. I.K and T.L. acknowledge the Fundação de Ampara à Pesquisa do Estado de São Paulo, FAPESP, grants #2016/12397-0, and #2014/22130-6 and #2017/15304-6, respectively. Authors also acknowledge the Research Centre for Gas Innovation, RCGI, sponsored by FAPESP grant #2014/50279-4 and Shell Brasil.[57]

-
- [1] J. Giner and C. J. Hunter. The mechanism of operation of the Teflon-bonded gas diffusion electrode: A mathematical model. *J. Electrochem. Soc.*, 116:1124–1130, 1969.
 - [2] M. B. Cutlip. An approximate model for mass transfer with reaction in porous gas diffusion electrodes. *Electrochim. Acta*, 20:767–773, 1975.
 - [3] A. Z. Weber and J. Newman. Modeling transport in polymer-electrolyte fuel cells. *Chemical Reviews*, 104:4679–4726, 2004.
 - [4] M. Bavarian, M. Soroush, I. G. Kevrekidis, and J. B. Benziger. Mathematical modeling, steady-state and dynamic behavior, and control of fuel cells: a review. *Industrial & Engineering Chemistry Research*, 49:7922–7950, 2010.
 - [5] S. A. Hajimolana, M. A. Hussain, W. M. A. W. Daud, M. Soroush, and A. Shamiri. Mathematical modeling of solid oxide fuel cells: a review. *Renew. Sust. Energ. Rev.*, 15:1893–1917, 2011.
 - [6] A. Z. Weber, R. L. Borup, R. M. Darling, P. K. Das, T. J. Dursch, W. Gu, D. Harvey, A. Kusoglu, S. Litster, M. M. Mench, R. Mukundan, J. P. Owejan, J. G. Pharoah, M. Secanell, and I. V. Zenyuk. A critical review of modeling transport phenomena in polymer-electrolyte

- fuel cells. *J. Electrochem. Soc.*, 161:F1254–F1299, 2014.
- [7] M. Andersson, J. Yuan, and B. Sundén. Review on modeling development for multiscale chemical reactions coupled transport phenomena in solid oxide fuel cells. *Appl. Energ.*, 87:1461–1476, 2010.
 - [8] F. Barbir. *PEM fuel cells*. Academic Press, San Diego, 2^a edition, 2013.
 - [9] N. Pourmahmoud, H. Sadeghifar, and A. Torkavannejad. A novel, state-of-the-art tubular architecture for polymer electrolyte membrane fuel cells: Performance enhancement, size and cost reduction. *Int. J. Heat Mass Tran.*, 108:577–584, 2017.
 - [10] H. Liu, M. G. George, N. Ge, D. Muirhead, P. Shrestha, J. Lee, R. Banerjee, R. Zeis, M. Messerschmidt, J. Scholta, P. Krolla, and A. Bazylak. Microporous layer degradation in polymer electrolyte membrane fuel cells. *J. Electrochem. Soc.*, 165:F3271–F3280, 2018.
 - [11] R. Darling. A comparison of models for transport resistance in catalyst layers. *J. Electrochem. Soc.*, 165:F1331–F1339, 2018.
 - [12] S. Chevalier, J.-C. Olivier, C. Josset, and B. Auvity. Polymer electrolyte membrane fuel cell operating in stoichiometric regime. *J. Power Sources*, 440:227100, 2019.
 - [13] I. V. Zenyuk, P. K. Das, and A. Z. Weber. Understanding impacts of catalyst-layer thickness on fuel-cell performance via mathematical modeling. *J. Electrochem. Soc.*, 163:F691–F703, 2016.
 - [14] S. Shimpalee, DeBolt M. Hirano, S., V. Lilavivat, J. W. Weidner, and Y. Khunatorn. Macro-scale analysis of large scale pem fuel cell flow-fields for automotive applications. *J. Electrochem. Soc.*, 164:E3073–E3080, 2017.
 - [15] T. Bednarek and G. Tsotridis. Issues associated with modelling of proton exchange membrane fuel cells by computational fluid dynamics. *J. Power Sources*, 343:550–563, 2017.
 - [16] B. Zhao, C. W. MacMinn, B. K. Primkulov, Y. Chen, A. J. Valocchi, J. Zhao, Q. Kang, K. Bruning, J. E. McClure, C. T. Miller, A. Fakhari, D. Bolster, T. Hiller, M. Brinkmann, L. Cueto-Felgueroso, D. A. Cogswell, R. Verma, M. Prodanović, J. Maes, S. Geiger, M. Vassvik, A. Hansen, E. Segre, R. Holtzman, Z. Yang, C. Yuan, B. Chareyre, and R. Juanes. Comprehensive comparison of pore-scale models for multiphase flow in porous media. *Proc. Natl. Acad. Sci. USA*, 116:13799–13806, 2019.
 - [17] L. S. Pan, J. Lou, H. Y. Li, and C. W. Kang. A diffusive interface model for two-phase flows with phase transition. *Phys. Fluids*, 31:092112, 2019.

- [18] P. Yi, S. Yang, C. Hakchi, and R. Lugo. A multicomponent real-fluid fully compressible four-equation model for two-phase flow with phase change. *Phys. Fluids*, 31:026102, 2019.
- [19] S. Whitaker. Flow in porous media I: A theoretical derivation of Darcy’s law. *Transport in Porous Media*, 1:3–25, 1986.
- [20] J. A. Ochoa-Tapia and S. Whitaker. Momentum transfer at the boundary between a porous medium and a homogeneous fluid–I. Theoretical development. *International Journal of Heat and Mass Transfer*, 38:2635–2646, 1995.
- [21] J. A. Ochoa-Tapia and S. Whitaker. Momentum transfer at the boundary between a porous medium and a homogeneous fluid–II. Comparison with experiment. *International Journal of Heat and Mass Transfer*, 38:2647–2655, 1995.
- [22] S. Bakhshian and M. Sahimi. Computer simulation of the effect of deformation on the morphology and flow properties of porous media. *Phys. Rev. E.*, 94:042903, 2016.
- [23] M.-J. Dalbe and R. Juanes. Morphodynamics of fluid-fluid displacement in three-dimensional deformable granular media. *Phys. Rev. Appl.*, 9:024028, 2018.
- [24] C. Z. Qiao, S. L. Zhao, H. L. Liu, and W. Dong. Connect the thermodynamics of bulk and confined fluids: Confinement-adsorption scaling. *Langmuir*, 35:3840–3847, 2019.
- [25] T. Lopes, M. Ho, B. K. Kakati, and A. R. J. Kucernak. Assessing the performance of reactant transport layers and flow fields towards oxygen transport: A new imaging method based on chemiluminescence. *J. Power Sources*, 274:382–392, 2015.
- [26] J. Rubio-Garcia, A. Kucernak, and A. Charleson. Direct visualization of reactant transport in forced convection electrochemical cells and its application to redox flow batteries. *Electrochem. Commun.*, 93:128–132, 2018.
- [27] T. Lopes, O. Beruski, A. M. Manthanwar, I. Korkischko, R. Pugliesi, M. A. Stanojev, M. L. G. Andrade, E. N. Pistikopoulos, J. Perez, F. C. Fonseca, J. R. Meneghini, and A. R. Kucernak. Spatially resolved oxygen reaction, water, and temperature distribution: Experimental results as function of flow field and implications for polymer electrolyte fuel cell operation. *Appl. Energ.*, 252:113421, 2019.
- [28] O. Beruski, T. Lopes, A. R. Kucernak, and J. Perez. Investigation of convective transport in the so-called “gas diffusion layer” used in polymer electrolyte fuel cell. *Phys. Rev. Fluids*, 2:103501, 2017.
- [29] A joint version of parts 1 and 2 can be found with DOI arXiv:2002.04519.

- [30] John W. Eaton, David Bateman, Søren Hauberg, and Rik Wehbring. *GNU Octave version 4.2.1 manual: a high-level interactive language for numerical computations*, 2017.
- [31] Available at <https://www.gimp.org/>.
- [32] M. Le Bars and M. G. Worster. Interfacial conditions between pure fluid and a porous medium: implications for binary alloy solidification. *Journal of Fluid Mechanics*, 550:149–173, 2006.
- [33] R. J. Millington and J. P. Quirk. Permeability of porous solids. *Transactions of the Faraday Society*, 57:1200–1207, 1961.
- [34] Z. Fishman, J. Hinebaugh, and A. Bazylak. Microscale tomography investigations of heterogeneous porosity distributions of pemfc gdl. *J. Electrochem. Soc.*, 157:B1643–B1650, 2010.
- [35] Z. Fishman and A. Bazylak. Heterogeneous through-plane distributions of tortuosity, effective diffusivity, and permeability for pemfc gdl. *J. Electrochem. Soc.*, 158:B247–B252, 2011.
- [36] R. Ono and T. Oda. Spatial distribution of ozone density in pulsed corona discharges observed by two-dimensional laser absorption method. *Journal of Physics D: Applied Physics*, 37:730–735, 2004.
- [37] W. J. Massman. A review of the molecular diffusivities of H₂O, CO₂, CH₄, CO, O₃, SO₂, NH₃, N₂O, NO and NO₂ in air, O₂ and N₂ near STP. *Atmospheric Environment*, 32:1111–1127, 1998.
- [38] O. Schenk and K. Gärtner. *Parallel Sparse Direct Solver PARDISO - User Guide*, versão 5.0.0 edition, 2014.
- [39] A. Picard, R. S. Davis, M. Gläser, and K. Fujii. Revised formula for the density of moist air (CIPM-2007). *Metrologia*, 45:149–155, 2008.
- [40] Supplemental Material is available at <https://arxiv.org/abs/2002.04519>.
- [41] M. L. Huber and A. H. Harvey. Diffusion in gases. In W. M. Haynes, editor, *CRC handbook of chemistry and physics*, chapter 6, pages 259–260. CRC, Boca Raton, 95^a edition, 2015.
- [42] T. R. Marrero and E. A. Mason. Gaseous diffusion coefficients. *Journal of Physical and Chemical Reference Data*, 1:3–118, 1972.
- [43] G. S. Beavers and D. D. Joseph. Boundary conditions at a naturally permeable wall. *Journal of Fluid Mechanics*, 30:197–207, 1967.
- [44] P. R. Amestoy, I. S. Duff, J. Koster, and J.-Y. L’Excellent. A fully asynchronous multi-frontal solver using distributed dynamic scheduling. *SIAM Journal on Matrix Analysis and Applications*, 23(1):15–41, 2001.

- [45] P. R. Amestoy, A. Guermouche, J.-Y. L'Excellent, and S. Pralet. Hybrid scheduling for the parallel solution of linear systems. *Parallel Computing*, 32(2):136–156, 2006.
- [46] Y. Saad and M. H. Schultz. GMRES: A generalized minimal residual algorithm for solving nonsymmetric linear systems. *SIAM Journal on Scientific and Statistical Computing*, 7:856–869, 1986.
- [47] A. Toselli and O. B. Widlund. *Domain Decomposition Methods*. Springer, Berlin, Heidelberg, 1 edition, 2005.
- [48] Y. Ye, G. Chiogna, O. A. Cirpka, P. Grathwohl, and M. Rolle. Experimental evidence of helical flow in porous media. *Phys. Rev. Lett.*, 115:194502, 2015.
- [49] I. Nitta, T. Hottinen, O. Himanen, and M. Mikkola. Inhomogeneous compression of PEMFC gas diffusion layer. Part I. Experimental. *J. Power Sources*, 171:26–36, 2007.
- [50] J. Kleemann, F. Finsterwalder, and W. Tillmetz. Characterisation of mechanical behaviour and coupled electrical properties of polymer electrolyte membrane fuel cell gas diffusion layers. *J. Power Sources*, 190:92–102, 2009.
- [51] A. El-kharouf, D. J. L. Mason, T. J. nd Brett, and B. G. Pollet. *Ex-situ* characterisation of gas diffusion layers for proton exchange membrane fuel cells. *J. Power Sources*, 218:393–404, 2012.
- [52] J. Millichamp, T. J. Mason, T. P. Neville, N. Rajalakshmi, R. Jervis, P. R. Shearing, and D. J. L. Brett. Mechanism and effects of mechanical compression and dimensional change in polymer electrolyte fuel cells - A review. *J. Power Sources*, 284:305–320, 2015.
- [53] N. V. Priezjev, A. A. Darhuber, and S. M. Troian. Slip behavior in liquid films on surfaces of patterned wettability: Comparison between continuum and molecular dynamics simulations. *Phys. Rev. E*, 71:041608, 2005.
- [54] T. Qian, X.-P. Wang, and P. Sheng. Hydrodynamic slip boundary condition at chemically patterned surfaces: A continuum deduction from molecular dynamics. *Phys. Rev. E*, 72:022501, 2005.
- [55] L. Wu. A slip model for rarified gas flows at arbitrary knudsen number. *Appl. Phys. Lett.*, 93:253103, 2008.
- [56] T. A. Ho, D. V. Papavassiliou, and A. Striolo. Liquid water can slip on a hydrophilic surface. *Proc. Natl. Acad. Sci. USA*, 108:16170, 2011.
- [57] Author contributions: O.B. designed and conducted the research, analyzed the data and

wrote the paper. I.K. contributed with discussions and by revising the paper. T.L. and F.C.F. contributed by revising the paper and with funding sources.

Progress Report on Numerical Modeling of a Prototype Fuel Cell:

2. Grid Convergence Study

Otávio Beruski,^{1,*} Ivan Korkischko,¹ Thiago Lopes,¹ and Fabio Coral Fonseca¹

¹*Instituto de Pesquisas Energéticas e Nucleares,
IPEN/CNEN-SP, 05508-000, São Paulo, São Paulo, Brazil*

Abstract

Progress on the numerical modeling of a prototype fuel cell is reported. Some known limitations of the previously published Alpha model are addressed, and the numerical uncertainty due to discretization of the improved model, Beta, was estimated. In this part, a mesh convergence study is carried out to estimate the discretization error of Beta. A reduced, proxy geometry and two extrapolation schemes are used to estimate the exact solution, which is then used to estimate the model's uncertainty through the Grid Convergence Index framework. Qualitatively, non-monotonic behavior is seen for the response variables as function of effective grid spacing. As such, the mixed-order extrapolation is favored over the generalized Richardson extrapolation in order to estimate the exact solution. Quantitatively, error estimates are on average $\sim 10\%$ for the flow rate range simulated, larger than experimental ones available. Results suggest a difficulty in achieving mesh convergence in fuel cell-like models, even in simpler cases. Caution is thus suggested during validation or when devising predictions from numerical models.

I. INTRODUCTION

Mathematical models are extremely important in basic and applied research, helping understand physical processes and allowing optimization of processes of interest. Models are based on observations of natural phenomena or controlled experiments, and as such must be validated, that is, must be compared to empirical data in order to assess its accuracy in reproducing the system of interest. Given this fundamental dependence on observations, it is crucial that one understands, and preferably quantifies, the uncertainties involved in the validation process. While it is common to think of uncertainties in experimental data, it is also imperative to identify, and quantify whenever possible, the uncertainties in mathematical models. Roache[1] gives an authoritative review on the subject, with more modern aspects discussed by, for example, Roy and Oberkampf[2].

Focusing on numerical procedures, particularly computational fluid dynamics (CFD), a key source of uncertainty is the discretization of the model's variables, e.g. spatial and time variables[3]. This discretization error arises from the approximation of continuous variables to discrete ones, for instance by stipulating that time t runs in small, finite steps δt . This

* oberuski@alumni.usp.br

leads to a dependency of the model’s variables of interest, say a scalar $\phi = \phi(t)$, on the size of δt , with the exact result being obtained in the limit of $\delta t \rightarrow 0$, in this example. Thus, it becomes important to establish that numerical results are independent of the discretization of independent variables, in order that the model represents the actual physical processes being studied, and not the approximations used to solve the underlying equations. Demonstrating this so-called grid convergence is, in practice, challenging, being untenable for most real-world scenarios[1], particularly for systems with complex geometry and physical processes[3] (fuel cells come to mind). The accepted practice is then to treat this as an uncertainty in the model’s results.

There are several methods to estimate discretization error in CFD. Following Roy[3], two broad classes may be defined: *a priori* and *a posteriori* methods, with *a posteriori* methods being more widely used. These are further divided in two branches: i) higher-order estimates, which relies on estimates of the exact solution, and may be applied in a post-processing manner after the solution has been computed; and ii) residual-based methods, which generally require the solution of an adjoint problem, specific to the system under study. While the latter has the potential of providing more detailed information on the error and its sources, it is in general more difficult to implement. The former methods are in general simpler to perform, however it may be necessary to obtain several solutions using systematically-refined, or coarsened, meshes. Among the higher-order methods, the Richardson extrapolation along with the Grid Convergence Index (GCI) framework[1, 4] are widely used, given its ease of application and applicability to any discretization scheme.

In the field of fuel cells, mathematical models play a significant role, with increasing complexity and spatial and time resolutions (see for instance [5–7] and references therein). Given that the complexity of fuel cell models and the computational resources employed have increased, while the precision and diversity of experimental data has also increased[7], it becomes particularly important to assess the uncertainties that invariably follow in order to properly validate a given model and use it for prediction. Uncertainty assessments in fuel cells are relatively uncommon, understandably so given the complexity of these devices and the costs associated with both empirical and numerical experiments. Concerning discretization error, when assessed, it is typically done through mesh refinement methods using a single response quantity, however usually without the higher-order extrapolate and the error estimate (see for example [8–11]). One exception, while not of a full device, is the work

of Tranter and colleagues[12], who used the GCI framework[4] to estimate the discretization error in a 2D model of a fibrous medium, representing the gas diffusion layer of a fuel cell. On the other hand, Kjeang and colleagues[13] provide an upper bound for the error when using a given mesh, possibly using an *a priori* method, and then proceed to compare the result of a single response quantity to the analytical solution of an approximate formulation of the problem. It is also worth noticing that the work of Beruski and colleagues[14], on which this work is based, also lacks the description of a discretization error estimate, like so many in the fuel cell literature.

We build on the previously published model for the aforementioned prototype fuel cell cathode[14], with the main goals of improving the mathematical framework, and therefore its accuracy, and estimating the discretization error, thus assessing its precision. In this part[15], a mesh convergence study has been carried out in order to assess the model’s uncertainty due to discretization, and thus provide an estimate of its precision. A reduced, proxy geometry was used to fully explore the feasible range of mesh density, and the convergence behavior of the chosen response variables was evaluated with respect to an effective element spacing. Two extrapolation schemes were then used and compared in order to assess the most appropriate given the convergence behavior observed. The error estimates for the proxy geometry were then calculated within the GCI framework[1, 4], while the error for the geometry of interest was further estimated from correlations with the proxy geometry. In this way, the remainder of this work is organized as follows. Section II provides an overview of the experimental significance and mathematical formulation of the model, as well as a description of the mesh convergence study. Section III first presents a qualitative assessment of the convergence behavior of relevant variables with mesh resolution, proceeding to a quantitative estimation of the discretization error. Finally, Section IV concludes with a summary of the results and brief remarks on future studies.

II. METHODS

We first present a brief description of the experimental device that is simulated by our model, first described by Lopes *et al.*[16], followed by the computational methods used for the development of this work.

The device is a prototype polymer electrolyte fuel cell (PEFC), more specifically a ca-

thodic half-cell, which allows *in situ* observation of reactive fluid flow in a porous medium. Ozone-enriched air is used as tracer in a carrier fluid, and a coumarin-based dye is used as the sensor to map the local concentration of O_3 . The O_3 interacts with the dye anchored on silica particles, akin to electrocatalysts dispersed in a porous layer, resulting in the emission of photons and the degradation of both reactant and dye. Measuring the light emission from this “catalyst layer” allows determination of the local O_3 concentration and, thus, the species and fluid dynamics. Global variables, such as pressure drop and total reactant drop, provide additional information on the inner workings of the device.

Thus, considering the experimental device, the proposed computational model covers momentum and species transport, while assuming thermal equilibrium and steady state. The computational domains included are: i) the flow channel (Ch), in this case a single serpentine geometry, ii) the porous transport layer, here comprising only a macroporous substrate (MPS) made of carbon paper (representing Toray TGH-060 with a 10% PTFE hydrophobic treatment), and iii) the catalyst layer (CL), where the catalyst and substrate particles are considered homogeneously distributed (representing Sigma Aldrich Nano Silica Gel on TLC plates, see [16] for details). Domains ii) and iii) comprise the porous media domains (Pm). Figure 1 shows the domains’ disposition and Table I presents the geometrical parameters.

The setup used for all simulations was a workstation with two Intel® Xeon® E3 processors and 128GB of RAM, operated with a 64 bits Debian9 distribution, Linux kernel v. 4.9.0-4. The software used was the commercial package COMSOL Multiphysics®, v.5.1.0.234, along with the Batteries and Fuel Cell, CFD, and Chemical Engineering modules. All data handling and processing was done using GNU Octave v.4.2.1[17], while image processing was done using GIMP v.2.10.14[18].

A. Mathematical Formulation

The vintage mathematical formulation, Alpha, can be found in [14], while the improved formulation, Beta, is detailed in Part 1. In this part, only the Beta model was used, and a brief description will be given below.

The momentum transport is described using the (compressible) Darcy-Brinkman formu-

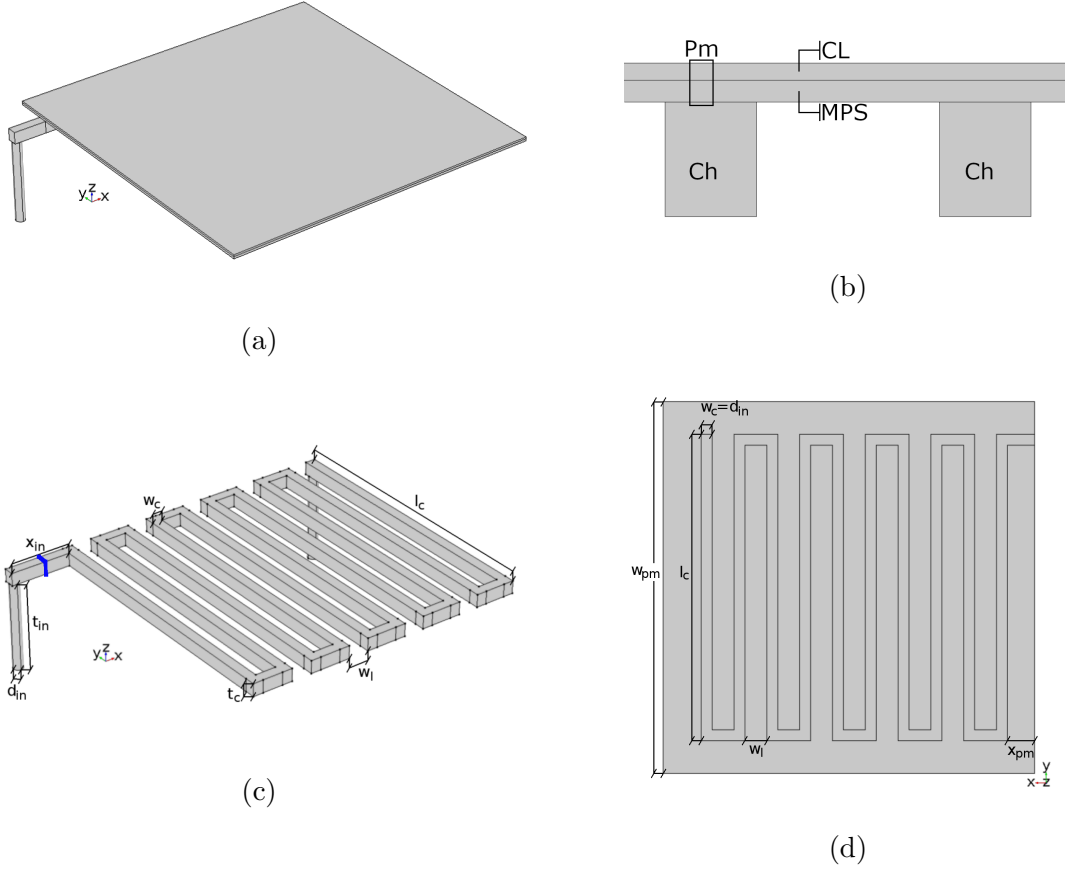


FIG. 1: Geometry used in the proto-cell simulations: **(a)** full geometry, showing the flow channel (Ch) and porous media (Pm) domains; **(b)** cross-section in the xz plane, showing the structure along the z axis; **(c)** Ch domain, with the segmentation edges shown in blue (see text), and **(d)** lower boundary of the MPS domain, showing the projection of the Ch domain.

lation (DB), which covers both free and porous media flow[19]:

$$\frac{\rho}{\epsilon} (\mathbf{u} \cdot \nabla) \left(\frac{\mathbf{u}}{\epsilon} \right) = \nabla \left[-P\mathbf{I} + \frac{\mu}{\epsilon} (\nabla \mathbf{u} + (\nabla \mathbf{u})^T) - \frac{2\mu}{3\epsilon} (\nabla \cdot \mathbf{u}) \mathbf{I} \right] - \frac{\mu}{\kappa} \mathbf{u}, \quad (1)$$

where ρ and μ are the fluid's density and kinematic viscosity, respectively, \mathbf{u} is the velocity field vector, P is the relative pressure, and ϵ and κ are the domain's porosity and permeability, respectively ($\epsilon = 1$ and $\kappa \rightarrow \infty$ for free flow). The parameters are shown in Table II, chosen in order to describe the materials and conditions used (see [16] and [14] for additional information). The inlet boundary condition is a (standard) mass flow rate condition:

$$-\int_{\partial\Omega} \frac{\rho}{\rho_{std}} (\mathbf{u} \cdot \mathbf{n}) dS = Q \quad (2)$$

TABLE I: Geometrical parameters of the computational domains.

Parameter	Symbol	Value
Channel width	w_c	0.8 mm
Land width	w_l	1.6 mm
Channel depth	t_c	1.0 mm
Channel section length	l_c	22.4 mm
Inlet/outlet diameter	d_{in}	0.8 mm
Inlet/outlet length	t_{in}	7.0 mm
Inlet offset	x_{in}	0.188 in
Porous media edge	w_{pm}	$(l_c + x_{\text{in}})$
Porous media offset	x_{pm}	$(x_{\text{in}} - w_w)/2$
MPS thickness	t_{MPS}	190 μm
CL thickness	t_{CL}	150 μm

with dry air at $T_{\text{std}} = 273.15$ K and $P_{\text{std}} = 1$ atm defining the standard density $\rho_{\text{std}} = P_{\text{std}} M_{\text{air}} / RT_{\text{std}}$. A constant pressure $P = P_{\text{out}}$ was used as the outlet boundary condition. The fluid's density is a function of the composition, calculated using the ideal gas law, while the viscosity is given by a constitutive relation for air, from the software:

$$\begin{aligned} \mu_{\text{air}}(T) = & -8.38278 \times 10^{-7} + 8.35717342 \times 10^{-8}T - 7.69429583 \times 10^{-11}T^2 \\ & + 4.6437266 \times 10^{-14}T^3 - 1.06585607 \times 10^{-17}T^4, \end{aligned} \quad (3)$$

where μ_{air} has units of Pa s and T of K.

The mass fraction formulation of the advection-reaction equation was used for the species transport, in a concentrated-mixture fashion, of an O_3/air gaseous mixture:

$$\nabla \cdot \mathbf{J}_i + \rho(\mathbf{u} \cdot \nabla)\omega_i = R_i \quad (4)$$

where ω_i is the mass fraction of the i -th species. In this model, the relative composition of O_2 and N_2 in the carrier gas, air, is taken to be constant. As such an effective species, “air”, with molar mass M_{air} , was used instead of the explicit components (see Part 1 for additional information on this subject). The mass diffusive flux was given by the Maxwell-Stefan (MS)

TABLE II: Parameterization of the model.

Parameter	Symbol	Value	Reference
Reference pressure	P_{ref}	1.027 bar	[14]
Cell back pressure	P_{out}	$1.0994 \text{ bar} - P_{\text{ref}}$	[14]
Carbon paper porosity	ϵ_{MPS}	0.801	[20]
Carbon paper permeability	κ_{MPS}	$9.18 \times 10^{-12} \text{ m}^2$	[21]
Carbon paper tortuosity	τ_{MPS}	1.199	[21]
Catalyst layer porosity	ϵ_{CL}	0.497	[14]
Catalyst layer permeability	κ_{CL}	$8.82 \times 10^{-11} \text{ m}^2$	[14]
O ₃ diffusion coefficient in N ₂	D_{O_3}	$0.16 \text{ cm}^2\text{s}^{-1}$	[22, 23]
Average molar mass of dry air	M_{air}	$28.96546 \text{ g mol}^{-1}$	[24]
O ₃ adsorption reaction rate constant	k_1	100 s^{-1}	see part I
O ₃ (ads) decomposition reaction rate constant	k_2	10 s^{-1}	see part I
Average silica particle radius	r_p	$6.5 \text{ }\mu\text{m}$	see part I
Quantity of dye deposited on the CL	Γ_{dye}	$3 \text{ }\mu\text{mol cm}^{-2}$	[16]

model:

$$\mathbf{J}_i = - \left(\rho \omega_i \sum_k D_{ik} \mathbf{d}_k \right) \quad (5)$$

$$\mathbf{d}_k = \nabla \chi_k + \frac{[(\chi_k - \omega_k) \nabla P_A]}{P_A} \quad (6)$$

where D_{ik} are multi-component diffusivities, \mathbf{d}_k is a so-called diffusional driving force, χ_k is the molar fraction and P_A is the absolute pressure. The Knudsen regime was included for porous media transport:

$$D_{ij} = \left[\frac{1}{D_{ij}^{\text{Pm}}} + \frac{1}{D_{ij}^{\text{K}}} \right]^{-1} \quad (7)$$

Here two effects are added in a parallel-resistances fashion: i) the porous media diffusion coefficient, $D_{ij}^{\text{Pm}} = f_{\text{Pm}} D_{ij}^{\text{free}}$, which applies a correction f_{Pm} , function of the porosity and tortuosity of the porous medium, to the “free” diffusion coefficient D_{ij}^{free} ; and ii) the Knudsen regime diffusivity, obtained through kinetic theory using the average pore diameter, d_p , instead of the mean free path in porous media. In this case, d_p was obtained using the Millington & Quirk model for cemented particle beds[25] for simplicity.

The reaction kinetics involving ozone degradation, and hence light emission, was modeled using an adsorption-decomposition scheme:



where the dye molecule is 7-diethylamino-4-methylcoumarin[16] and the desorption step was ignored. A differential equation involving the surface cover of O_3 , θ_{O_3} , was solved along the fluid and species dynamics:

$$\frac{d\theta_{\text{O}_3}}{dt} = k_1\chi_{\text{O}_3}(1 - \theta_{\text{O}_3}) - k_2\theta_{\text{O}_3} \quad (10)$$

where k_1 and k_2 are reaction rate constants for the adsorption and decomposition reactions, respectively. To couple with Eq. 4, one may write:

$$R_{\text{O}_3} = -M_{\text{O}_3}A_v\Gamma_s^*k_1\chi_{\text{O}_3}(1 - \theta_{\text{O}_3}) \quad (11)$$

where A_v is the total surface area by unit volume and Γ_s^* is the total surface concentration of active sites, i.e. dye molecules. The total surface concentration of adsorption sites can be obtained with:

$$\Gamma_s^* = \frac{\Gamma_{\text{dye}}}{t_{\text{CL}}A_v} \quad (12)$$

where Γ_{dye} is the reported[16] quantity of dye deposited over a given geometric area of CL with thickness t_{CL} . The A_v is calculated using a simple model:

$$A_v = \frac{3\epsilon_{\text{CL}}}{r_p} \quad (13)$$

where r_p is the average particle radius, in this case the silica particles where the dye were anchored on (Nano Silica Gel, Sigma Aldrich).

The solver configuration used depends on the actual mesh used, however it followed a general configuration according to the number of mesh elements. A detailed description, as much as possible, can be found in Section SII A of the Supplemental Material[26] (SM). The general outline is the following: a segregated 3-steps solver was employed, with step i) solving for θ_{O_3} , step ii) solving for \mathbf{u} and P , and step iii) solving for ω_{O_3} . Step i) always employed a direct solver, based on MUMPS[29, 30], while step ii) always employed an iterative solver based on GMRES[31], a multigrid scheme with a number of levels and mesh

coarsening scheme depending on the number of mesh elements. Step iii) either employed a direct solver, also MUMPS-based, or a GMRES-based iterative solver using the domain decomposition method[32]. The direct solver was employed for the cases where $\lambda \leq 4$, otherwise the iterative solver was used, with the number of sub-domains depending on the number of mesh elements. All steps used a constant dampening factor in all cases, being 1.0, 1.0 and 0.7 for steps i), ii) and iii), respectively. In addition, a parametric solver was used to vary Q from 200 to 450 cm³ min⁻¹ with a step of 50 cm³ min⁻¹, with the previous solution used as initial value for the next one.

Finally, the use of an assembly for the computational geometry allowed greater control of the meshing procedure. As a consequence, explicit coupling between the geometric entities was needed to ensure the proper continuity of the model’s variables, i.e. the flow field, \mathbf{u} , and ozone mass fraction, ω_{O_3} . This was accomplished via an identity pair. Since the relevant boundaries were sectioned to properly match one another (at the Ch and MPS domains, see Fig. 1), no fallback features were necessary.

B. Mesh Convergence Study

1. Algorithm and refinement procedure

As mentioned above, the model’s geometry was an assembly of two geometric entities, the flow channel (Ch) and the porous media (Pm). This separation was used in order to achieve a larger degree of control with respect to the meshing procedure, allowing, for example, meshing the Ch and Pm domains separately in order to investigate the effects of each mesh individually. Following much experimentation, a protocol was established in order to assess mesh convergence in all domains, with respect to a single index, λ , which is somewhat connected to the more usual element spacing h in structured meshes. The meshing algorithm, briefly, had the following outline:

1. Meshing of the Ch domain with tetrahedral elements, with scaling factor λ .
2. Splicing the boundary-adjacent elements to add 3 hexahedral elements (“boundary layer elements”, BLEs).
3. Copying the upper boundary of the Ch mesh to the projection onto the lower MPS

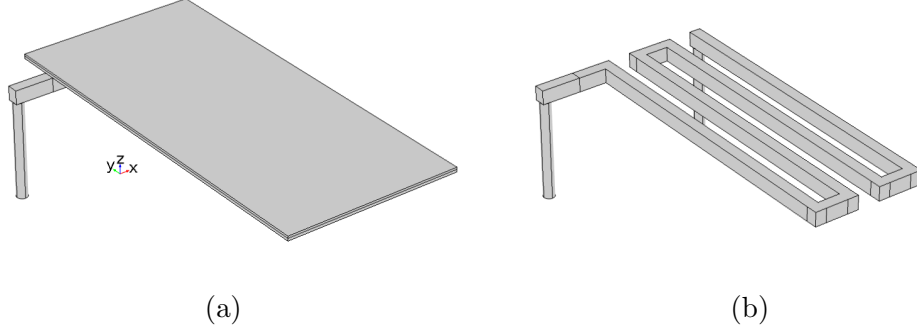


FIG. 2: Reduced geometry used in the proto-cell simulations using dense meshes: **(a)** full geometry, showing both Ch and Pm domains, and **(b)** Ch domain.

boundary.

4. Meshing the remainder of the lower MPS boundary with triangular elements, with scaling factor 1.
5. Extruding the lower boundary elements throughout the Pm domains, with λ elements in each domain.

The element size parameters used in steps 1 and 4 were based on software recommendations, which in turn are believed to be based on the size of the full geometry. The so-called BLEs of step 2 are a software recommendation when dealing with relatively coarse meshes. A variant of this meshing algorithm without step 2 was also used. Details of the algorithm and of each mesh are given in Section SII B of the SM[26], along with Fig. S1 illustrating the meshes built.

Given the current computational resources available, a reduced version of the geometry was employed to solve the model when using dense meshes. The Ch domain was shortened to 4 horizontal sections of the serpentine geometry, down from 10, as shown in Figure 2. The Pm domains were reduced accordingly, with the remaining geometric parameters kept constant. As such, the scaling factor λ for the reduced geometry takes the values $\lambda \in [2, 4, 8, 10, 12, 16]$, while for the full geometry it reduces to $\lambda \in [2, 4, 8, 12]$.

2. Convergence analysis

Four quantities were chosen as response variables in order to assess mesh convergence. These are of experimental interest, and, with the exception of the speed profiles, are readily available given the experimental setup[16] and improvements being sought. These were selected to allow comparison between the reduced and full geometries, as well as between previous and present model formulations (see Part 1). It is understood that some variables are functionals of the base variables solved in the model, and thus might not be as sensitive to the mesh. The response variables are the following:

- the ratio K' between reactant consumption, $\Delta\chi_{\text{O}_3}$, and the apparent reaction rate R'_{O_3} ;
- the pressure drop, ΔP , normalized by the inlet pressure, P_{in} ;
- the flow speed profile, U , along the x and z axes; and
- the ozone partial pressure, P_{O_3} , along the x axis.

Concerning the acquisition of the data from the model, Figure 3 shows, for the reduced model, the relevant geometric entities used. The same are used for the full model, when appropriately scaled. A brief description of the adopted procedure follows. $\Delta\chi_{\text{O}_3}$ and ΔP are simply the differences in value between inlet and outlet averages, while P_{in} is the inlet average pressure. R'_{O_3} is given by integration over the upper CL boundary (Fig. 3a) of the term $A_v\Gamma_s^*k_2\theta_{\text{O}_3}$, which is the volume-averaged decomposition term for θ_{O_3} . The U profiles were obtained at mid-length of the third horizontal section (Figs. 3b and 3c), where the x axis profile was obtained at mid-height, while the z axis profile was obtained at mid-width. The P_{O_3} was obtained at the upper CL boundary (Fig. 3d), along a line parallel to the x axis, passing over the turn sections of the flow channel.

Additional information and results associated with the response variables may be found in Part 1. It should be noted that, in this part, the apparent reaction rate R'_{O_3} is not normalized by the inlet concentration as in Part 1, and consequently neither is the K' ratio. This was done in order to maximize sensitivity to the mesh resolution in the response variables. In any way, as a matter of completeness, the SM[26] provides relevant data for the quantification of the discretization error for the O_3 inlet concentration $C_{\text{O}_3,\text{in}}$, the normalized apparent

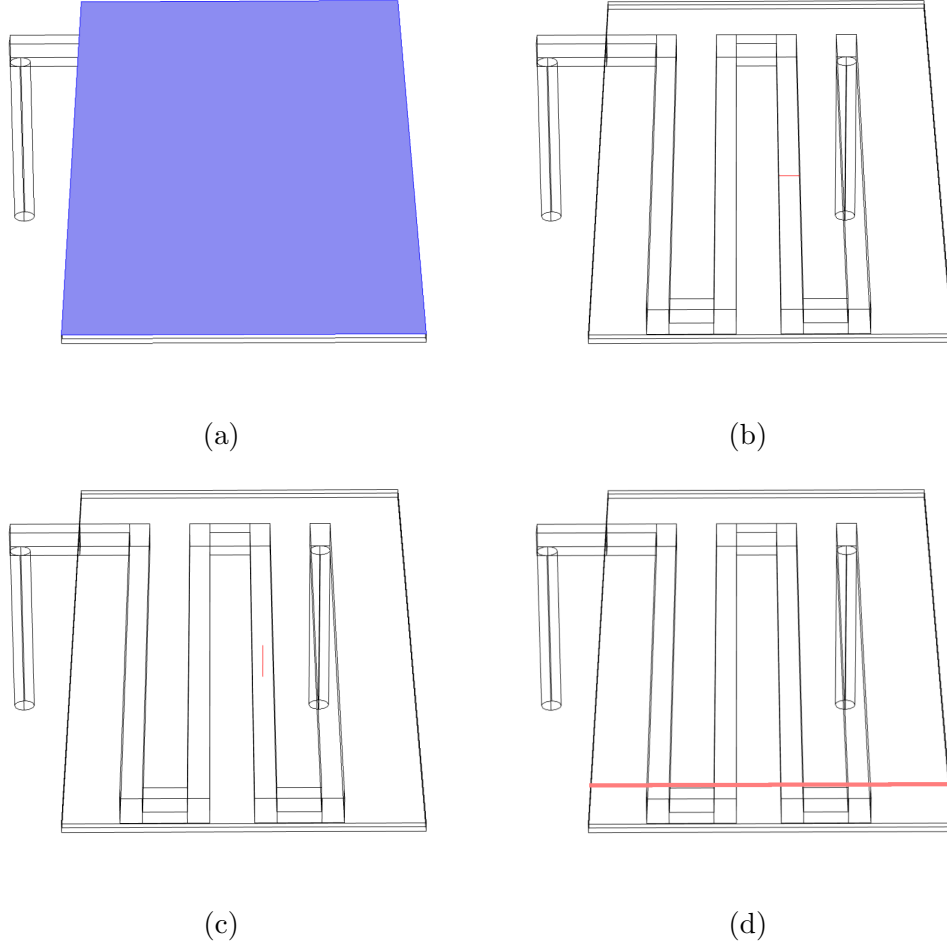


FIG. 3: Geometrical entities used to obtain the variables relevant for mesh convergence, shown for the reduced geometry: **(a)** **surface** used to obtain the apparent reaction rate, corresponding to the upper boundary of the CL domain; **(b,c)** **lines** used to track the flow speed x and z profiles, respectively; and **(d)** **line** used to track the ozone partial pressure profile atop the CL domain.

reaction rate $R'_{\text{O}_3}/C_{\text{O}_3,\text{in}}$ and the corresponding ratio K' , as well as the real and apparent stoichiometries (λ and λ' , respectively, in Part 1). Thus, if needed, it is possible to convert between response variables with the appropriate error estimate.

In addition to the response variables mentioned above, some spatially-resolved quantities were also acquired, albeit mainly as illustrations of the effects of the grid resolution. These are the ozone partial pressure \mathbf{P}_{O_3} , obtained at the upper CL boundary, and U surfaces, obtained with a xy plane mid-height of the Ch domain and a yz plane cutting the middle of the second turn, before the section where the U profiles were taken. Finally, some quantities

were obtained to explore secondary issues, not related to mesh convergence. These were i) additional P_{O_3} profiles, parallel to the one shown in Fig. 3d, obtained at different y values: $y_1 = (l_c - w_c)/2$ (shown in Fig. 3d), $y_2 = y_1 - (w_c + w_l)$ and $y_3 = 0$. And ii) components of the ozone total molar flux vector, i.e. diffusive and convective, given by the 1st and 2nd terms of Eq. 4 respectively. These were acquired in the following situations: the z -component of a given molar flux vector, integrated over the boundary between Ch and MPS domains, or MPS and CL domains; and the magnitude of a given molar flux vector, averaged over the MPS or CL domains.

In order to quantitatively assess mesh convergence, the scalar response variables, i.e. K' and $\Delta P/P_{in}$, were analyzed within the framework of the grid convergence index (GCI), as reviewed by Roache[1]. Thus, the generalized Richardson extrapolation was employed to provide an estimate on the error given by the discretization of the computational domains. First, the effective refinement factors were calculated using[1]:

$$r_{\text{eff}} = \left(\frac{N_{\text{finer}}}{N_{\text{coarser}}} \right)^{1/D} \quad (14)$$

where N is the number of elements in a given mesh and $D = 3$ is the dimensionality. Eq. 14 was also used to calculate an effective, normalized element spacing, h , used to plot and visually analyze the mesh convergence of the selected variables. For such effect, a mesh is chosen such that $r_{\text{eff}} = h = 1$, thus coarser meshes are given by $h > 1$. For the reduced geometry, $\lambda = 16$ was used, while for the full geometry $\lambda = 12$ was used. The orders of accuracy were all calculated iteratively following the suggestion given in [1] (Eq. 15 of [1]), as the refinement ratios were non-integers and not constant. The generalized Richardson extrapolation was then used to estimate the exact value for a given variable f , by comparing the finest grid solution with a coarser one:

$$\bar{f}_R = f_1 + \frac{\epsilon_{21}}{1 - r_{12}^p} \quad (15)$$

where we use the commonly employed convention of referencing the finer mesh with index 1, and progressively coarser meshes as 2, 3 and so on; $\epsilon_{21} = f_2 - f_1$ is the error, while r_{12} is the (effective) refinement factor between meshes 1 and 2. The GCI is then given by:

$$\text{GCI} = F_s |\bar{f}_R - f_1| \quad (16)$$

where F_s is a safety factor, taken as $F_s = 1.25$ in this case[1]. As mentioned above, the GCI is

then used as an estimate to the error of the model due to discretization of the computational domains.

In addition to the generalized Richardson extrapolation, a mixed-order extrapolation, described by Roy[33], was also employed. This extrapolation scheme has the advantages of not requiring the calculation of the order of accuracy or assuming the variables are in the asymptotic range, thus potentially allowing non-monotonic behavior and singularities in the grid convergence analysis. In this case, the discretized solution is given by a power series in h [33]:

$$f_k = f_{\text{exact}} + g_1 h_k + g_2 h_k^2 + \mathcal{O}(h_k^3) \quad (17)$$

where k stands for a given mesh index following the convention pointed out above. In [33], a 1st- and 2nd-order scheme is presented, with $\bar{f}_M \approx f_{\text{exact}}$ being obtained by solving a set of three linear equations up to powers in h_k^2 . It is also mentioned[33] that it is possible to include higher-order terms by coupling additional equations, and thus meshes, in order to increase the order of the extrapolation. The set of linear equations was solved using the *linsolve* function of Octave[17], without any additional options. The error estimate is then calculated following a simple error calculation:

$$\epsilon_M = F_s |\bar{f}_M - f_1| \quad (18)$$

where it can be seen that it is essentially the same as Eq. 16, when using the Richardson extrapolation to estimate the exact value.

III. RESULTS

First a qualitative analysis of the convergence behavior of the response variables will be given in Sections III A and III B, focusing at the reduced and full geometries respectively; followed by Section III C with a quantitative estimation of the discretization error and, therefore, the convergence of the variables with respect to the mesh. The different mesh schemes and relevant response variables analyzed are described in Section II B, and additional details can be found in the SM[26].

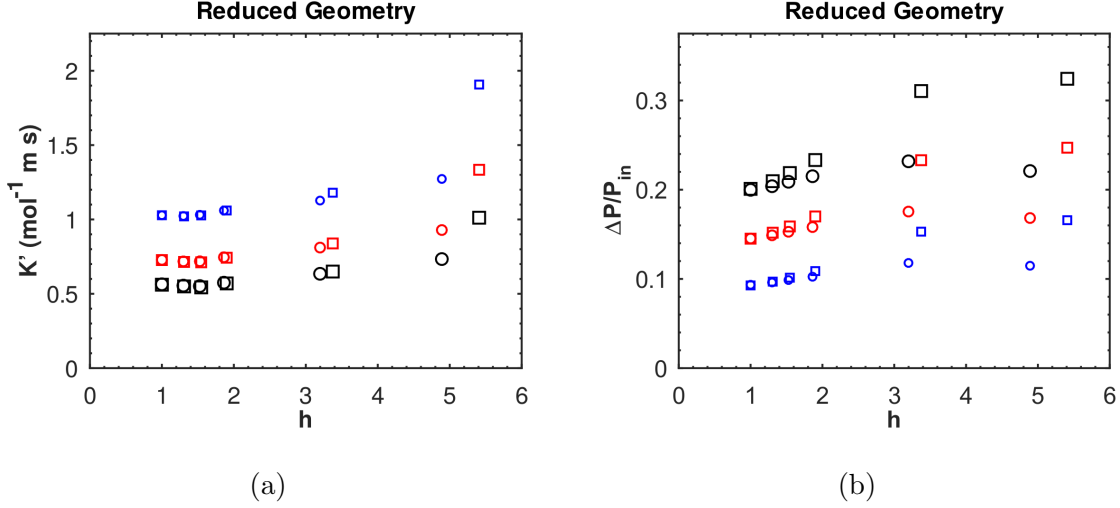


FIG. 4: Scalar response variables as functions of the normalized effective element spacing, for the reduced geometry: **(a)** $K' = \Delta\chi_{\text{O}_3}/R'_{\text{O}_3}$ and **(b)** $\Delta P/P_{\text{in}}$. The following values of inlet flow rate Q are shown, with marker size increasing with Q : 250, 350 and $450 \text{ cm}^3 \text{ min}^{-1}$. Both mesh variants are shown: with (\circ) and without (\square) BLEs.

A. Reduced Geometry

We start with the analysis of the reduced model in order to cover the full range of λ studied. Following Section II B 2, first the scalar response variables will be analyzed, followed by the speed and partial pressure profiles and finally the partial pressure surfaces. Thus, Figures 4a and 4b present the ratios $K' = \Delta\chi_{\text{O}_3}/R'_{\text{O}_3}$ and $\Delta P/P_{\text{in}}$, respectively, as a function of h . In each case both BLEs and no-BLEs study variants are shown (See Section II B 1). Individual variables are left to Section SIII of the SM[26] (Fig. S2).

Readily apparent features of Fig. 4 are the large differences between the BLE and no-BLE variants at coarser meshes, i.e. high h , and the convergence of values at finer meshes, particularly for the K' ratio. In addition, it is seen that, for the $\Delta P/P_{\text{in}}$ ratio, the existence of BLEs leads to a non-monotonic behavior at high h . Indeed, this is also seen for $\Delta\chi_{\text{O}_3}$ (Fig. S2a) and ΔP (Fig. S2c), while, notably, R'_{O_3} (Fig. S2b) shows such behavior for both mesh variants. The differences caused by the existence of BLEs, or likewise the absence of BLEs, are linked to a much better description of the velocity field \mathbf{u} in coarser meshes, as will be clear when discussing speed profiles. Likewise, the non-monotonic behavior seen with R'_{O_3} is linked to the poor description of \mathbf{u} along the thickness of the Pm domains, and,

consequently, to that of the ozone mass fraction ω_{O_3} .

Additional features of Fig. 4 are the non-monotonic behavior of K' at low h , and a relatively slow convergence of $\Delta P/P_{\text{in}}$. It is not clear why K' , and likewise $\Delta\chi_{\text{O}_3}$, shows such behavior, or why is it dependent on Q . Suspicion once again resides with \mathbf{u} , as does with the reason behind the slow convergence of $\Delta P/P_{\text{in}}$ (and also of ΔP), and will be further explored below. Nevertheless, Roache[1] does point out that, far from the asymptotic regime, a variable can show non-monotonic behavior as function of element spacing. Indeed, considering the apparent lack of studies exploring mesh convergence in models of fuel cells and similar devices, an important result of this work is exactly the demonstration that experimentally relevant response variables, even functionals of base variables, show non-monotonic behavior in a relatively wide range of h for 3D unstructured meshes. Thus, rather unfortunately, demonstrating mesh convergence for experimentally relevant variables in fuel cells may be a harder case than usually assumed.

We now proceed to analyze the profiles, starting with the speed profiles, U . Figure 5 shows the U profiles parallel to x and z axes, at $Q = 350 \text{ cm}^3 \text{ min}^{-1}$. Once again a marked difference is seen between meshes with and without BLEs at high h (low λ). As pointed out above, such marked differences at high h are thought to be responsible for the distinct behaviors seen for each mesh variant in Figs. 4 (likewise in Fig. S2). The absence of BLEs leads to a large underestimation of U in the Ch domain, which is known to contribute significantly to reactant transport to the Pm domains[14], thus affecting total reaction rate and reactant consumption. It is clear, then, from Figs. 5a and 5b that the presence of BLEs provides a much needed resolution close to the Ch walls, however that necessity fades as the mesh improves. Indeed, at $\lambda = 12$ the mesh variants display close similarity, with an average difference of $\approx 3.5\%$ for both x and z profiles.

Concerning the dependence of U with h , it can be seen that, as $h \rightarrow 0$, the flow in the Ch domain assumes a Poiseuille-like shape, i.e. parabolic as function of wall distance. This is of course expected at the center of the channel, for a well-developed flow field, and suggests that meshes with $\lambda \geq 12$ provide a good description of the flow field. A similar trend is seen in Fig. 5c for the CL, however with an initial overestimation of U and a sharp gradient along z . This poor description of U , when comparing $\lambda = 2$ to 16, might be related to the non-monotonic behavior observed for R'_{O_3} (Fig. S2b) at high h : while U is overestimated at the peak, the sharp gradient leading to $U = 0$ at the CL upper boundary might contribute

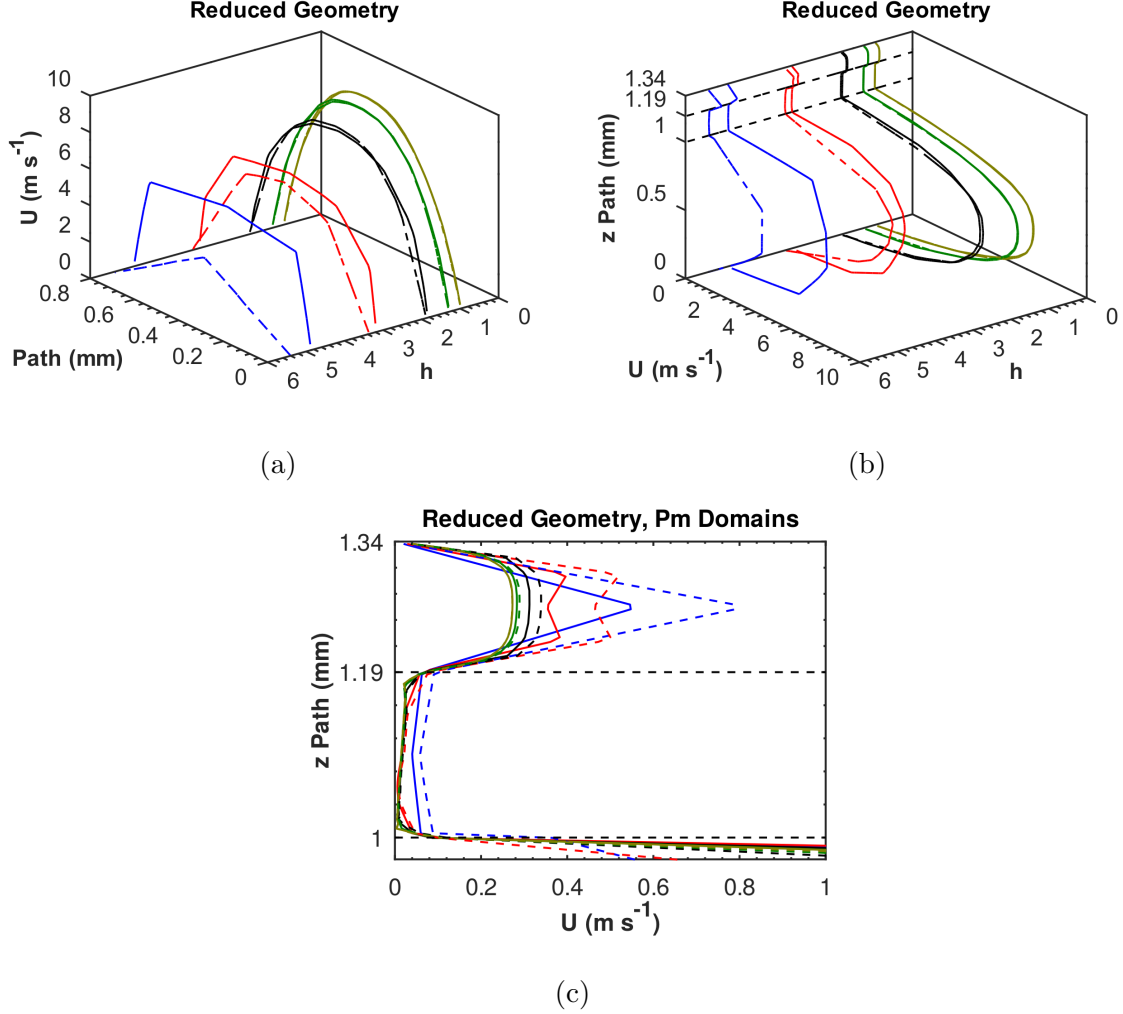


FIG. 5: Flow speed profiles as functions of the normalized effective element spacing, for $Q = 350 \text{ cm}^3 \text{ min}^{-1}$: **(a)** profile along the x axis, **(b)** along the z axis, with **(c)** zoom in on the Pm domains. Both BLE (full lines) and no-BLEs (dashed lines) mesh variants are shown. The following values of λ are shown: 2, 4, 8, 12, and 16. In **(b-c)** the dashed black lines in the $y = 0$ plane correspond to the boundaries between Ch and MPS, and MPS and CL domains, while in **(c)** the MPS-CL boundary is depicted.

to lower rates of O_3 transport to the surface, thus reducing the observed value of R'_{O_3} . For the MPS, on the other hand, U takes a more complex shape that is quite inappropriately modeled for $\lambda \leq 4$. Such profile is thought to result from the interaction with the Ch and CL domains, where both have larger permeabilities than the MPS (with $\kappa_{\text{Ch}} \rightarrow \infty$). While the case of coupled free and porous media flow is widely studied in general, when approaching the problem analytically it is common to assume a semi-infinite porous medium domain (see

for instance [19, 34]), which leads to a transition zone at the boundary and a plug-flow-like front in the porous medium that is typical of Darcy’s law. Interactions between porous media, or walls, are less explored and possibly quite idiosyncratic, leading to unconventional effects (see for instance [35]). Thus, it is difficult to judge if the U profile in the Pm is well-described, as some changes are still noticeable between $\lambda = 12$ and 16.

Another point worth noticing concerns the symmetry of the U profiles with wall distance. While it is not clear in Fig. 5, and the effect is somewhat subtle, the improved description of \mathbf{u} as λ increases allows modeling finer structures that might provide additional insight on the interpretation of experimental results. Figure 6 shows superimposed U profiles of the no-BLEs mesh variant, for $\lambda \geq 8$ and selected values of Q . For the sake of visibility the BLEs variant is not shown, however it does show the same trends discussed below, as suggested by the close agreement between mesh variants shown in Fig. 5. For the x profiles (Fig. 6a) it can be seen that, for $\lambda = 8$, U is virtually symmetric around the center of the channel, even as Q increases. As λ increases, however, it becomes increasingly apparent that U is not symmetric, in particular for high Q . It is noteworthy that for $\lambda = 16$ the U profile is asymmetric throughout the Q range simulated. This is likely to be an effect of secondary flows at the turns of the channel, which are better resolved the finer the mesh. This will be further explored below, but it already points out that the turns of a serpentine flow channel have far-reaching effects on the flow field, besides the fact that it greatly contributes to the convective transport in porous media[14]. Regarding the z profiles (Fig. 6b), the asymmetry in U is much more subtle: there are virtually no deviations for $\lambda = 8$ and 12 throughout the Q range, while $\lambda = 16$ shows some asymmetry at $Q \geq 350 \text{ cm}^3 \text{ min}^{-1}$, becoming apparent at $450 \text{ cm}^3 \text{ min}^{-1}$. This effect appears to be caused by the porous interface, between Ch and MPS domains, as no such asymmetry is seen when a no-slip boundary condition is set instead (not shown). It is not clear, however, if it is also related to the turns of the flow channel.

We sidetrack now for a moment to consider the spatially-resolved U surfaces, in order to get a glimpse of the effects of the mesh on \mathbf{u} as mentioned above. Figure 7 shows U surfaces, for $\lambda \in [8, 12, 16]$ and $Q = 350 \text{ cm}^3 \text{ min}^{-1}$, at the second turn of the serpentine Ch domain. Figures 7a to 7c show a mid-height xy plane, where it is readily noted the existence of known secondary flows, due to the corners and from boundary layer separation (BLS). While real turns are not 90° sharp, it has been shown, albeit indirectly, that the simulated

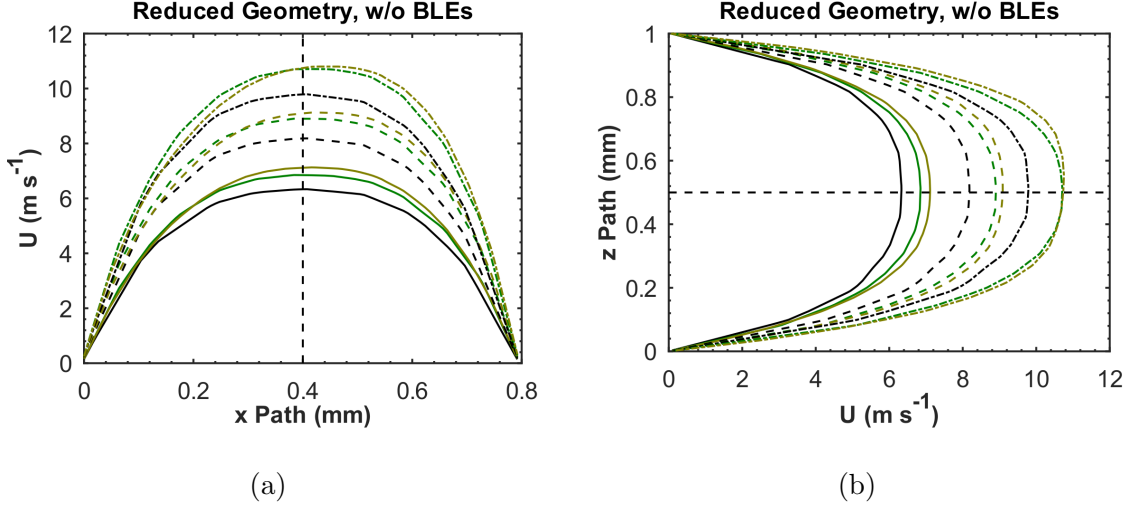


FIG. 6: Flow speed profiles for selected values of λ and Q , using the no-BLEs mesh variant: (a) profile along the x axis and (b) along the z axis. The following values of λ are shown: 8, 12, and 16. The following values of Q are shown: 250 (full), 350 (dash), and 450 $\text{cm}^3 \text{min}^{-1}$ (dash-dot). The dashed black lines parallel to the U axes are visual guides stressing the middle of the path along the Ch domain.

flow field correlates quite well with experiments[14, 16]. As λ increases, a larger effect of the BLS is noticed, and recirculation at the corners become better resolved. Better resolution is of course the whole point, however it is noteworthy how the improved description of the BLS significantly changes the flow field after the turn: at $\lambda = 8$, the flow field is almost completely re-developed at the end of the Ch section shown, while at $\lambda = 16$, there is a significant shift of the flow field to the right. This builds upon the discussion around Fig. 6a, establishing that BLS is a major source of the U profile asymmetry observed, and that fine grid resolution is needed to properly describe such effects. In addition to effects at the Ch domain, BLS is thus expected to impact on reactant distribution at the Pm domains. As shown in [14], secondary flows at the turns of serpentine Ch are major drivers of reactant distribution, therefore one would expect that the effect caused by BLS just uncovered might have implications as well. One such implication is a discrepancy between experimental and simulated P_{O_3} surfaces, noted in [14], concerning a broader plume of O_3 along each horizontal section of the Ch in the experimental device. We shall come back to this point below, when analyzing O_3 partial pressure.

It is also worth looking at the cross-section of the turn. It was shown in [14] that the turns

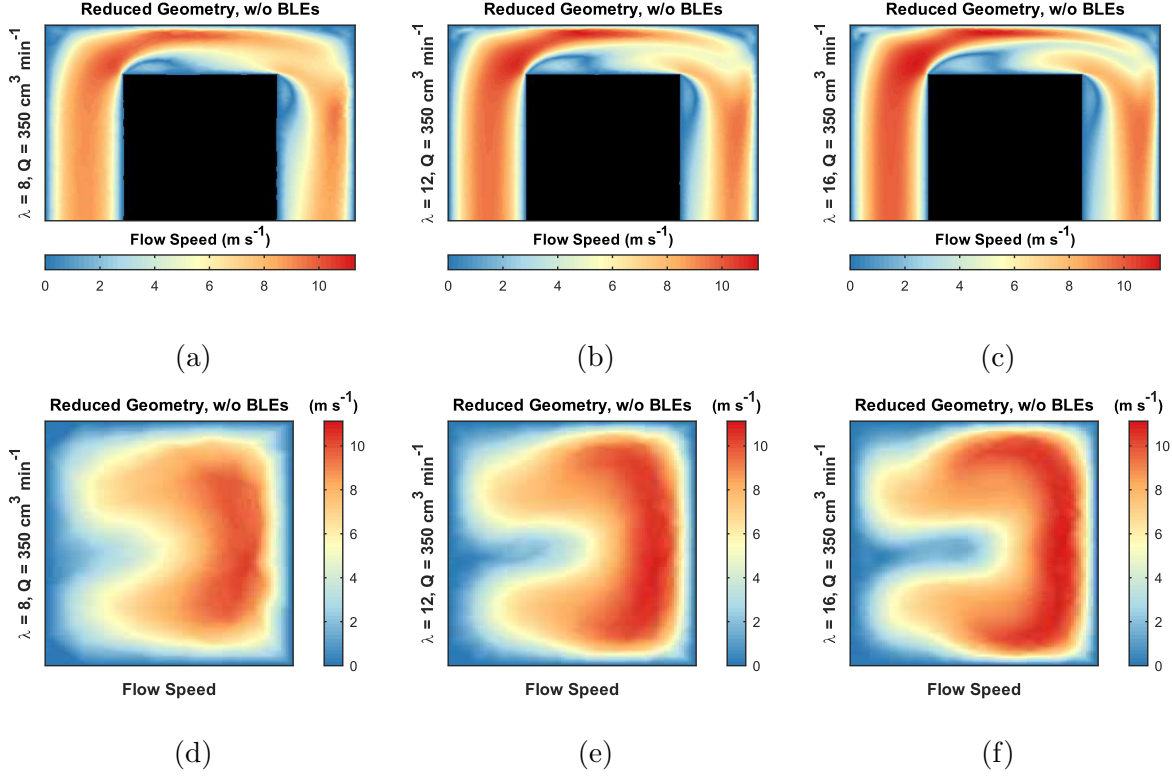


FIG. 7: Flow speed surfaces for selected values of λ and $Q = 350 \text{ cm}^3 \text{ min}^{-1}$, using the no-BLEs mesh variant: **(a-c)** xy plane mid-height of the 2nd turn of the Ch domain and **(d-f)** yz plane cutting through the middle of the turn. The values of λ sampled are indicated, and include $\lambda = 8, 12$, and 16 .

of the serpentine Ch creates vortices, which are thought to contribute to reactant transport to the Pm domains. Figures 7d to 7f show U at a yz plane at the middle of the turn, also for $\lambda \in [8, 12, 16]$ and $Q = 350 \text{ cm}^3 \text{ min}^{-1}$. Far from being a numerical artifact, it is indeed seen that these vortices are robust, and that increased grid resolution shows better defined structures, with higher U and possibly greater contribution to reactant transport.

In all, Figs. 6 and 7 provide further evidence that the flow field in fuel cell flow channels, in particular serpentine ones, are rather complex and require good grid resolution to properly capture its features. It also sheds some light on the convergence behavior of the scalar variables analyzed above (Fig. 4): i) there is a significant change in \mathbf{u} at $\lambda > 8$, which might underlie the non-monotonic behavior of the K' ratio at low h (or the individual variables), and ii) the grid resolution necessary to resolve such relatively small-scale structures might underlie the slow convergence rate of $\Delta P/P_{\text{in}}$. Thus, it is of utmost importance that grid

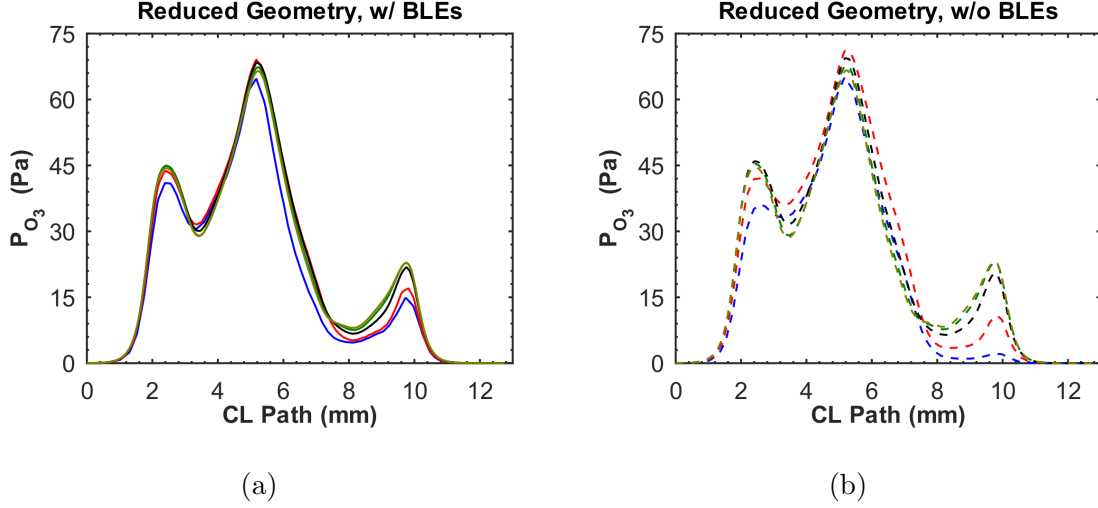


FIG. 8: Ozone partial pressure profiles, at $Q = 350 \text{ cm}^3 \text{ min}^{-1}$, for both mesh variants: **(a)** with BLEs (full line) and **(b)** without BLEs (dashed line). The following values of λ are shown: 2, 4, 8, 12, and 16.

convergence studies be performed before validating and actually employing fuel cell models for predictions.

Resuming our analysis, we move to the ozone partial pressure profiles, P_{O_3} . Figure 8 shows the profiles obtained at the upper CL boundary, along the x axis, for $Q = 350 \text{ cm}^3 \text{ min}^{-1}$. Analyzing each mesh variant individually at first, it is observed that the BLEs variant (Fig. 8a) shows relatively little qualitative change, and progressively small changes as λ increases. On the other hand, the no-BLEs variant (Fig. 8b) show a marked increase in P_{O_3} at the end of the flow path, as λ increases. Nevertheless, when comparing both mesh variants, it can be noticed that their profiles are very similar at $\lambda = 16$, although their dependency on h is somewhat different. This is further illustrated on Fig. S10, where fewer values of λ are shown, and very small differences are seen between the variants at $\lambda = 16$. It is thus seen that the P_{O_3} profiles benefit from BLEs at high h , particularly at the end of the flow path.

Finally, in order to provide a broader, albeit qualitative view on the effects of the mesh on P_{O_3} , we will briefly analyze the ozone partial pressure surfaces, \mathbf{P}_{O_3} . Figure 9 presents such surfaces for selected values of λ , with $Q = 350 \text{ cm}^3 \text{ min}^{-1}$. The no-BLEs mesh variant is shown in order to highlight the changes as λ increases, however, in general, the changes follow those seen in Fig. 8. There are several trends that can be observed as λ increases: i) the increased P_{O_3} values at the end of the flow path, after the last turn; ii) an improved

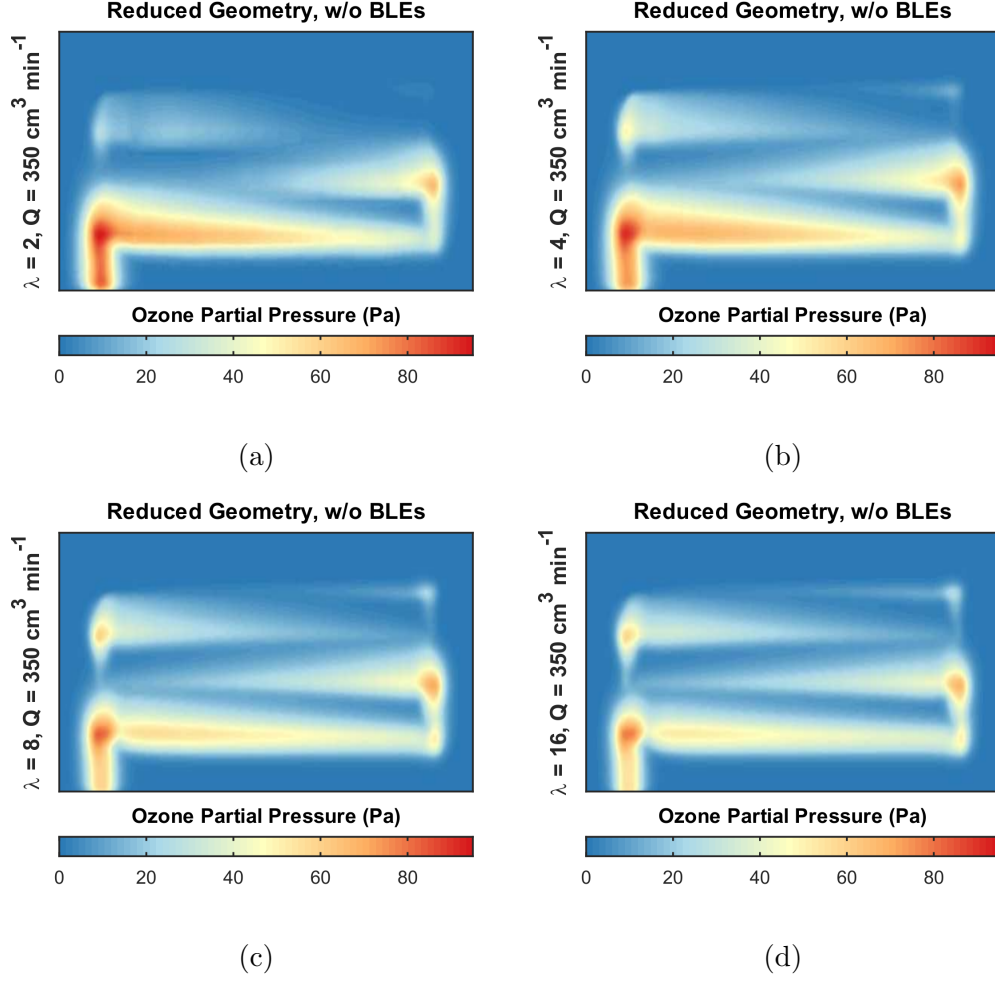


FIG. 9: Ozone partial pressure surfaces for selected values of λ and $Q = 350 \text{ cm}^3 \text{ min}^{-1}$, using the no-BLEs mesh variant: (a) $\lambda = 2$, (b) $\lambda = 4$, (c) $\lambda = 8$, and (d) $\lambda = 16$.

description of the local P_{O_3} maxima after each Ch turn; iii) a narrowing of the ozone plume along each horizontal section; and iv) a decrease of maximum P_{O_3} values. Trends i) and ii) are directly related to the improved description of \mathbf{u} , as seen in Figs. 5 and 7, which impacts not only P_{O_3} through better resolution, but also by reducing $\Delta\chi_{\text{O}_3}$ (Figs. 4 and S9) and consequently allowing increased concentrations of ozone to reach the end section of the Ch domain. Skipping to trend iv), reduced P_{O_3} values might also be connected to \mathbf{u} , although it is thought that the increased resolution at the Pm domains might play a larger role in this case. In addition, smaller P_{O_3} values might also be related to the reduced $\Delta\chi_{\text{O}_3}$ values at high λ , suggesting that increased influence of \mathbf{u} , possibly in the form of convective transport, impacts reactant distribution, thus reducing local P_{O_3} maxima.

Trend iii) is also thought to be connected to the improved description of \mathbf{u} , as well as improved resolution across the Pm domains' thickness. However it provides a counter-evidence to the point raised when analyzing Figs. 6 and 7. It was suggested that the effect the BLS has on \mathbf{u} after each turn, that of deforming its x profile towards the wall, could underlie the broader reactant plume observed in the experimental P_{O_3} surfaces (see [16] for the original data and [14] for a comparison between experimental and numerical data). While \mathbf{u} at the Ch domain has a large influence on the Pm domains, and refining the grid indeed corroborates this point, it appears that this discrepancy between experimental and numerical data is not yet settled.

Trends iii) and iv) warrant some additional inspection, as it might be useful when considering numerical results with lower grid resolution. Following the inverted analysis of trends iii) and iv), we start by further analyzing trend iv), by looking into the reactant transport. Figure 10 presents the diffusive and convective contributions to O_3 transport for selected values of λ , for the cases described in Section II B 2. From Figs. 10a and 10b it is seen that convective transport between domains increases with Q , as expected, while diffusive transport shows a maximum around $Q = 300 \text{ cm}^3 \text{ min}^{-1}$, between the Ch and MPS domains, and a slight increase with Q between MPS and CL domains. Concerning molar flux inside each Pm domain, Figs. 10c and 10d show that convective transport is the dominant process, observed the difference in permeability between domains and thus \mathbf{u} (see Fig. 5), showing large increase with Q , while the diffusive transport shows relatively little increase with Q . Overall, this picture corroborates the conclusions drawn from the previous study[14], where the convective transport is found to be a large contributor to reactant transport in all domains of the device. Concerning this work, Fig. 10 adds to the picture, showing that, in general, increased grid resolution ($h \rightarrow 0$) leads to a decrease in convective transport, while the diffusive contribution slightly increases. This has the overall effect of reducing total O_3 transport to the CL, and thus reducing P_{O_3} at the CL, as well as $\Delta\chi_{\text{O}_3}$ and R'_{O_3} (see Fig. S4 for the explicit dependency on h).

Returning once again to trend iii), additional insight may be obtained by considering P_{O_3} profiles normalized by R'_{O_3} . Figure 11 shows the $P_{\text{O}_3}/R'_{\text{O}_3}$ profiles at three parallel lines along the x axis, described in Section II B 2 by y_1 , y_2 , and y_3 . Shown are selected values of λ and Q for the no-BLEs mesh variant, in order to illustrate the changes as either λ or Q increases. In all profiles it is seen that, contrary to Fig. 8, the local maxima corresponding

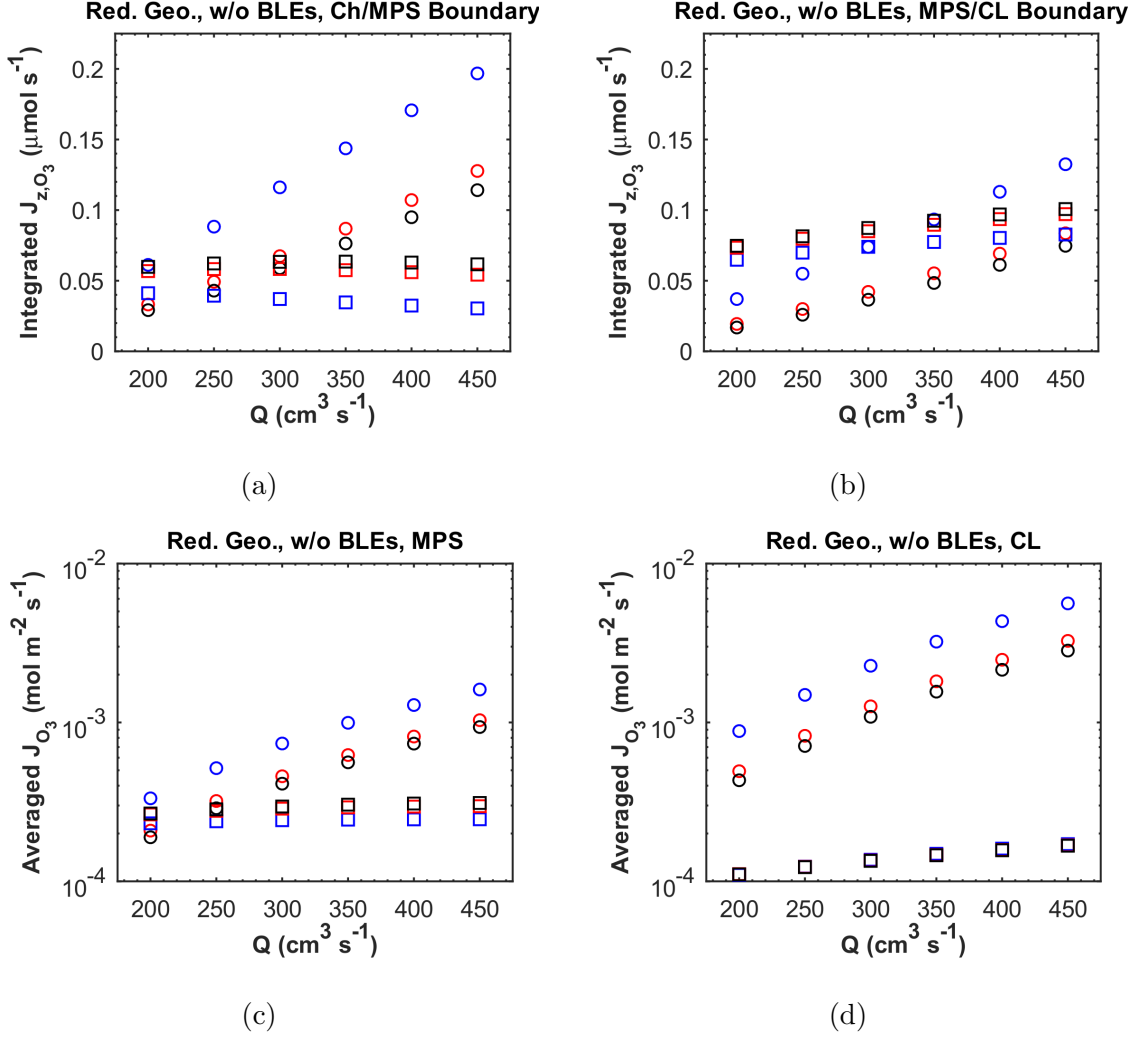


FIG. 10: Contributions to ozone molar flux as function of the flow rate, using the no-BLEs mesh variant, for selected values of λ : 4, 8, and 16. (a) integrated z component of the molar flux over the boundary between Ch and MPS domains, and (b) between MPS and CL domains; (c) average magnitude of the molar flux over the MPS and (d) domains. Both convective (\circ) and diffusive (\square) contributions to the total molar flux are shown.

to the Ch domain increases: while the absolute value of P_{O_3} may decrease as λ increases, the value relative to R'_{O_3} increases. This corroborates the scenario that, while the magnitude of the convective transport of reactant may decrease with λ , the improved description of \mathbf{u} given by the finer grids better capture the reactant distribution in the device. This is seen to be particularly important at the end of the flow path, where $\lambda = 4$ greatly underestimates the local reactant distribution. Regarding trend iii) and the hypothesis discussed before,

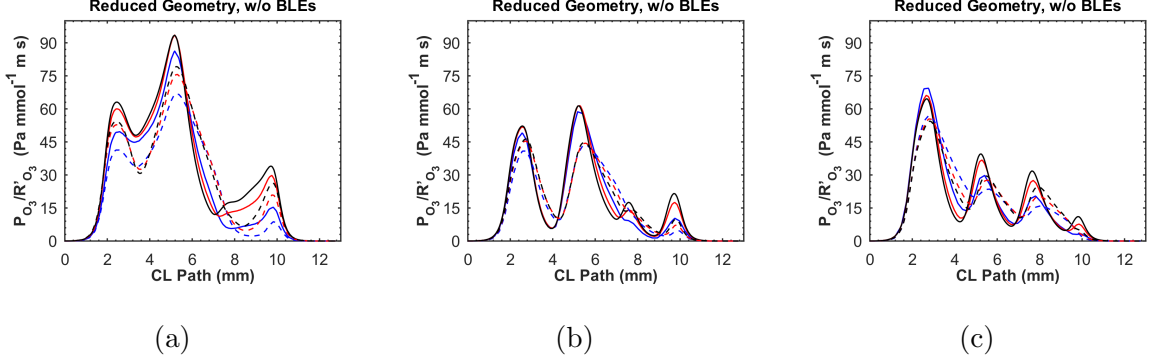


FIG. 11: Ozone partial pressure profiles, using the no-BLEs variant, for selected values of λ : 4, 8, and 16; and Q : 250 (full line) and 450 $\text{cm}^3 \text{min}^{-1}$ (dashed line). The profiles were obtained at the upper boundary of the CL , parallel to the x axis, according to Section II B 2: (a) y_1 , shown in Fig. 3d; (b) y_2 ; and (c) y_3 .

Fig. 11 settles the issue, showing that in fact the spread of the reactant plume, between Ch sections, decreases with λ . Increasing Q also increases the plume spread, as already seen in Fig. 9, as well as slightly shifting the local maxima towards higher x values, corroborating the effects of the shifted U maximum seen in Fig. 6. Thus, while the improved description of \mathbf{u} in the Ch domain has effects throughout the Pm domains, it does not seem to be responsible for the reactant plume spread seen in the experimental data.

B. Full Geometry

We complete this first analysis with a brief comparison between the behavior of the reduced geometry, analyzed above, and that of the full geometry. Focus will be given to the largest values of λ used in the full geometry, 8 and 12, as well as the largest value used in the reduced geometry, $\lambda = 16$. In addition, only the no-BLEs mesh variant will be used, as the analysis above already shows that both mesh variants provide very similar results for $\lambda \geq 12$. The entire range of λ for the full geometry, as well as the BLEs mesh variant can be found in Section SIII B of the SM[26] (Figs. S5 to S12).

Once again we follow the order previously established, starting with the scalars described on Section II B 2. Figure 12 presents the $K' = \Delta\chi_{\text{O}_3}/R'_{\text{O}_3}$ and $\Delta P/P_{\text{in}}$ ratios for both reduced and full geometries, as functions of a normalized effective element spacing h' , calculated with reference to the meshes with $\lambda = 12$. It can be seen that, for both scalars, the convergence

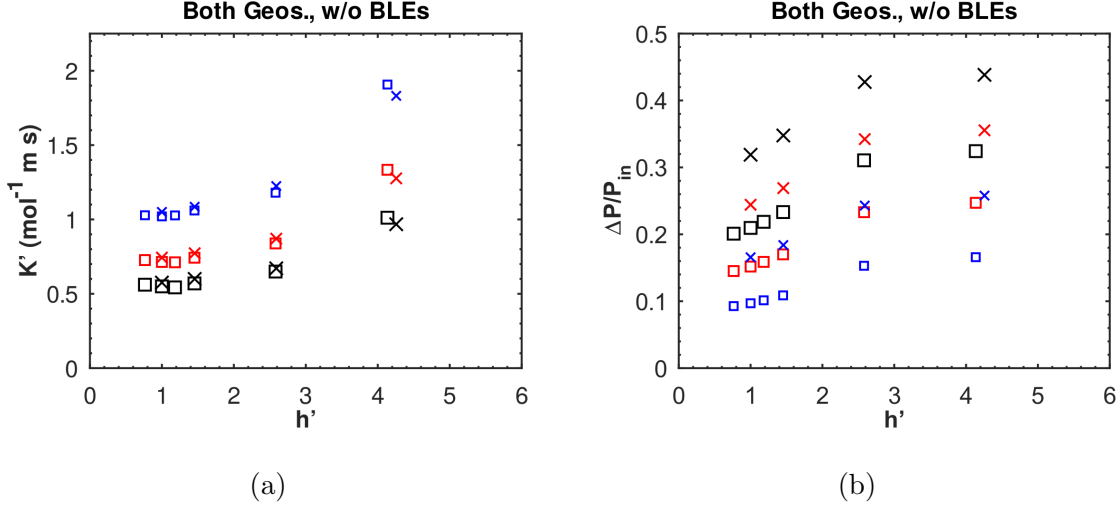


FIG. 12: Scalar variables as functions of the normalized effective element spacing, obtained for both reduced (\square) and full (\times) geometries: **(a)** $K' = \Delta\chi_{\text{O}_3}/R'_{\text{O}_3}$ and $\Delta P/P_{\text{in}}$. The following values of inlet flow rate Q are shown, with markers increasing in size with Q :
250, 350 and $450 \text{ cm}^3 \text{ min}^{-1}$.

behavior is very similar between reduced and full geometries. It should be pointed out, however, that the K' ratio displays a monotonic behavior for the full geometry. An additional mesh with $\lambda = 10$ might help to draw this behavior out, although it is unnecessary given that R'_{O_3} display non-monotonic behavior with h' (Fig. S5b). Care must be taken, therefore, in order to realize a fuller picture before drawing conclusions on grid convergence. Small differences in value, mainly seen in Fig. 12b, are likely due to the fact that the corners in the Ch domain contribute non-linearly to the overall results of the device, particularly for ΔP . This is another evidence to the well-known fact that the scaling of fuel cells is not linear, in particular for serpentine-type flow channels.

Moving on to the U profiles, Figure 13 shows the x and z profiles for both geometries, superimposing values of λ and with $Q = 350 \text{ cm}^3 \text{ min}^{-1}$. It can be observed that both geometries have very similar U profiles, both in x and z , with the largest differences at the CL domain, while the MPS domain shows the smallest. This result is expected, given that the characteristic dimensions of the flow and Q are the same for both geometries. It is important nevertheless to be assured of this, given the already pointed out non-linear scaling of fuel cells, but also due to possible numerical artifacts.

Finally, the P_{O_3} profiles are compared in Figure 14, while the \mathbf{P}_{O_3} surfaces for the full

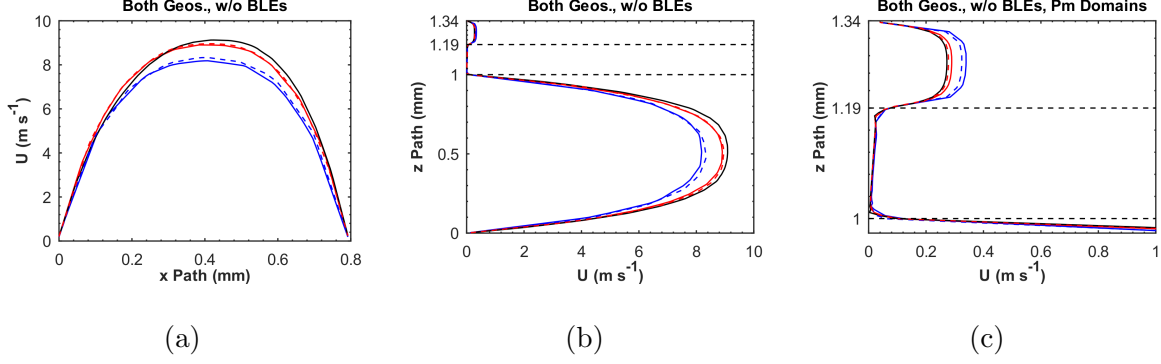


FIG. 13: Flow speed profiles for the reduced (full lines) and full (dashed lines) geometries, using the no-BLEs mesh variant, for $Q = 350 \text{ cm}^3 \text{ min}^{-1}$: (a) profile along the x axis, (b) along the z axis, with (c) zoom in on the Pm domains. The following values of λ are shown: 8, 12, and 16.

geometry are shown in Figure 15, comparing them with the reduced geometry for $\lambda = 12$ (see also Fig. 9). Regarding the P_{O_3} profiles, Fig. 14a shows close similarities between reduced and full geometries at the beginning of the flow path, with a marked distinction at the last local peak. The similarities are once again to be expected, given the geometrical and operational parameters of each model. The significant difference at the last peak in Fig. 14a, while at first may stand out, is readily understood when noticing that in Fig. 14b the same happens for the full geometry: the last channel of the Ch domain has no gradients driving the reactant forward in the CL domain, thus acting only as the final sink. Fig. 14 thus shows once again that both reduced and full geometries have similar grid convergence behavior, while at the same time further illustrating the non-linear scaling of fuel cell devices.

Regarding the \mathbf{P}_{O_3} surfaces, shown in Fig. 15, the same behavior observed for the reduced geometry is seen when comparing $\lambda = 8$ and 12 for the full geometry, however in smaller magnitude, given the smaller grid refinement between them. The clearer aspect to be seen is the decrease in maximum P_{O_3} , which follows the behavior seen in Fig. 9. When comparing both geometries, with the reduced one shown scaled in Fig. 15c for better comparison, it can be seen that the \mathbf{P}_{O_3} surfaces are very similar. The major difference is at the spread of the plume after the third peak in the reduced geometry, however that is clearly due to the interaction with the last section of the Ch, as pointed out above when analyzing Fig. 14. Indeed, the same behavior, albeit with much smaller P_{O_3} values, is seen at the ninth peak.

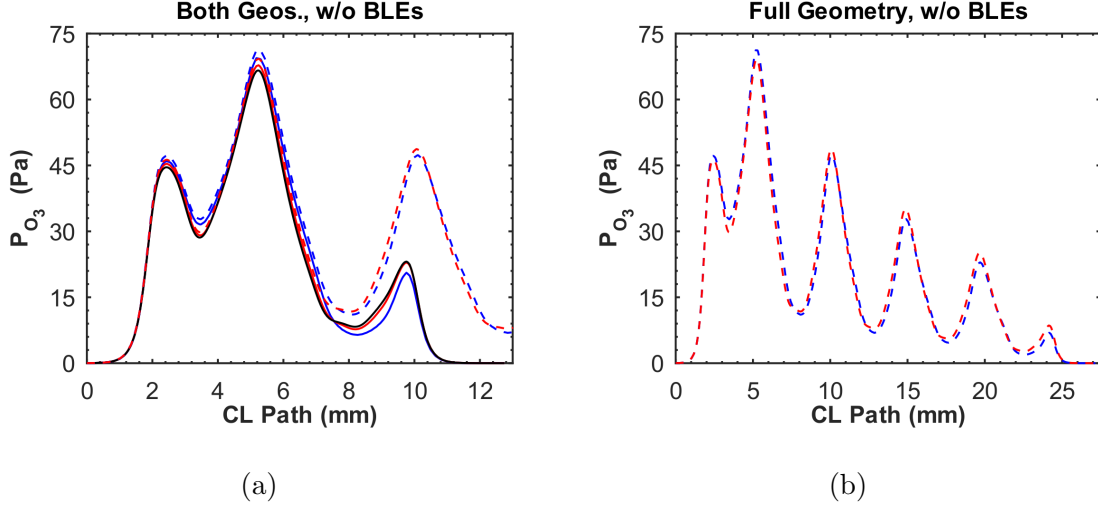


FIG. 14: Ozone partial pressure profiles, at $Q = 350 \text{ cm}^3 \text{ min}^{-1}$, using the no-BLEs mesh variant for selected values of λ : 8, 12, and 16. **(a)** Comparison between reduced (full lines) and full (dashed lines) geometries; **(b)** full view of the profile for the full geometry.

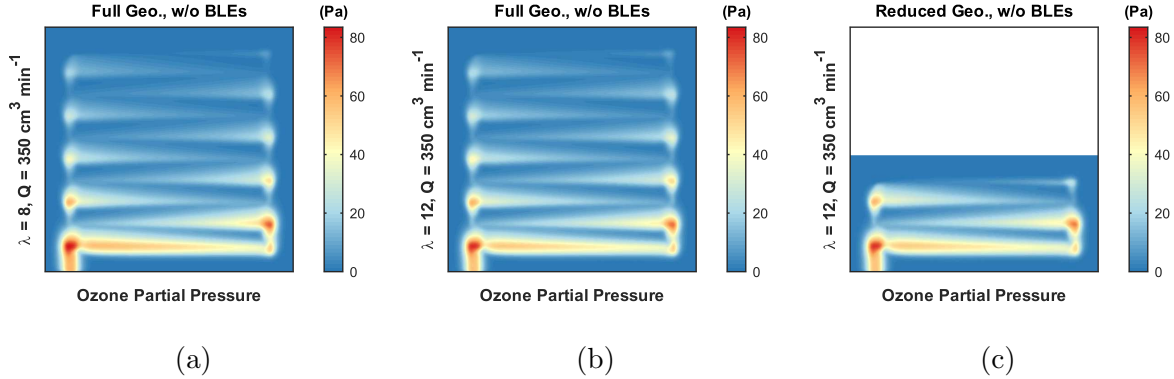


FIG. 15: Ozone partial pressure surfaces for selected values of λ and $Q = 350 \text{ cm}^3 \text{ min}^{-1}$, using the no-BLEs mesh variant: **(a)** full geometry, $\lambda = 8$ and **(b)** $\lambda = 12$, and **(c)** reduced geometry, $\lambda = 12$.

The data show that the reduced geometry is a good proxy to study mesh convergence in the fuel cell prototype's model, given that we are currently unable to simulate meshes with $\lambda > 12$ for the full geometry. Having shown this correlation between geometries, it opens up the possibility of further studying the numerical aspects of the model as function of the mesh, extending the current analysis to structured meshes and improved unstructured mesh schemes that may allow denser meshes with comparable computational resources.

C. Estimation of Discretization Error

Given the qualitative analysis of Sections III A and III B, it might be argued that the variables chosen to track mesh convergence do not, in fact, show convergence. Not only the convergence appears to be relatively slow, some variables also show non-monotonic behavior depending on the mesh scheme. While a robust sign of convergence would be ideal, given the computational resources and accuracy of experimental data available, it is important to point out, as did Roache[1], that most of the time actual mesh convergence is impractical. Thus, instead of going further down this rabbit hole, we chose to accept the fact that the model has some error due to discretization, and tried to estimate that. We will now present the results from the generalized Richardson extrapolation (GRE), following Roache[1], and the mixed-order extrapolation (MOE), following Roy[33], used to estimate the discretization error of the scalar variables, according to Section II B 2.

First and foremost, it should be pointed out that, given the convergence behavior observed in Section III A and the refinement ratios used in this study, it was not clear which set of meshes should be used in the extrapolations in order to accurately reproduce the behavior seen. It is pointed out by Roache[1] that the refinement ratio between grids, r , should be $r > 1.3$, in order to be able to minimize other possible numerical errors when performing the convergence study. Thus, some tests were done with the reduced geometry following this suggestion, and the following was concluded: i) the extrapolation schemes show different results depending on the mesh scheme, i.e. with or without BLEs, although the differences are relatively small and mainly concerns the region at high h ; ii) when the dataset used to calculate the extrapolate display non-monotonicity, the GRE returns complex values for the accuracy order and, consequently, to the extrapolate, although the magnitude of the imaginary term is relatively small; iii) the GRE and the MOE show different behavior according to which scalar is being analyzed, with both schemes showing similar results for the $\Delta P/P_{\text{in}}$ only; iv) the GRE appears to converge as finer meshes are used to calculate it, in particular for the K' ratio, while the MOE appears to exaggerate the non-monotonic behavior in these cases; and v) including a third-order term in the MOE improves its results over the whole h range. The trends observed when evaluating the extrapolation schemes are likely to be related to the non-monotonicity of the data, as suggested in [33], particularly the fact that the MOE deals, in principle, with such data sets, while the GRE assumes the

data are in the asymptotic range. In these cases where the GRE returned complex values, only the real part was used to calculate the GCI. Additional information can be found in Section SIV A of the SM[26], while Figs. S13 and S14 show selected results of the tests done over the extrapolation schemes.

From the conclusions drawn, it was established that for the GRE the meshes to be used, for both mesh variants, were $\lambda \in [8, 12, 16]$, while for the MOE $\lambda \in [2, 4, 10, 16]$ were used, with $[4, 10, 16]$ used for the MOE up to h_k^2 . The same schemes were also used to estimate the discretization error on the individual variables, $\Delta\chi_{O_3}$, R'_{O_3} , and ΔP . We proceed now to evaluate the results of using the GRE and MOE schemes with the aforementioned meshes, in order to establish the best estimate of the discretization error of the reduced and full geometries of the model under study.

We start with the scalar response variables already discussed in Sections III A and III B. Figure 16 shows the scalars as function of h , with the three extrapolation schemes: GRE, 1st- and 2nd-order MOE (MOE-12), and 1st-, 2nd- and 3rd-order MOE (MOE-123). Concerning the K' ratio, Figs. 16a and 16b show that the MOEs show better agreement with the numerical results, while the GRE clearly overestimates the convergence of the variable, with very small differences between $h = 1$ to 0. In particular, the MOE-123 shows the best fit to the entire h range, which is expected given the choice of meshes to calculate the coefficients and extrapolate. MOE-12 shows good agreement, despite the poor description at high h , in particular for the BLEs variant. However, when comparing MOE-123 to MOE-12 for the BLEs mesh variant, it appears that the derivative between $h = 1$ and 0 is somewhat overestimated, however that is based on the assumption that for $\lambda \geq 10$ ($h \approx 1.5$) the variable is in the asymptotic range.

For the $\Delta P/P_{in}$ ratio, Figs. 16c and 16d show better agreements between the GRE and MOE schemes, however it is still clear that the GRE greatly overestimates the convergence of the variable. Like with the K' ratio, both MOE schemes show good agreement with the numerical results, with MOE-12 showing relatively large differences for $h > 3$. Likewise, MOE-123 once again predicts a seemingly odd behavior at $h < 1$, in particular for the no-BLEs variant. It is not inconceivable that for $h < 1$ a faster rate of convergence might be observed for $\Delta P/P_{in}$, as predicted by both GRE and MOE-123 when compared to MOE-12. However given the slow rate observed for the numerical results available, and the monotonic behavior at $h < 4$, it appears that the MOE-12 estimate is more plausible, particularly for

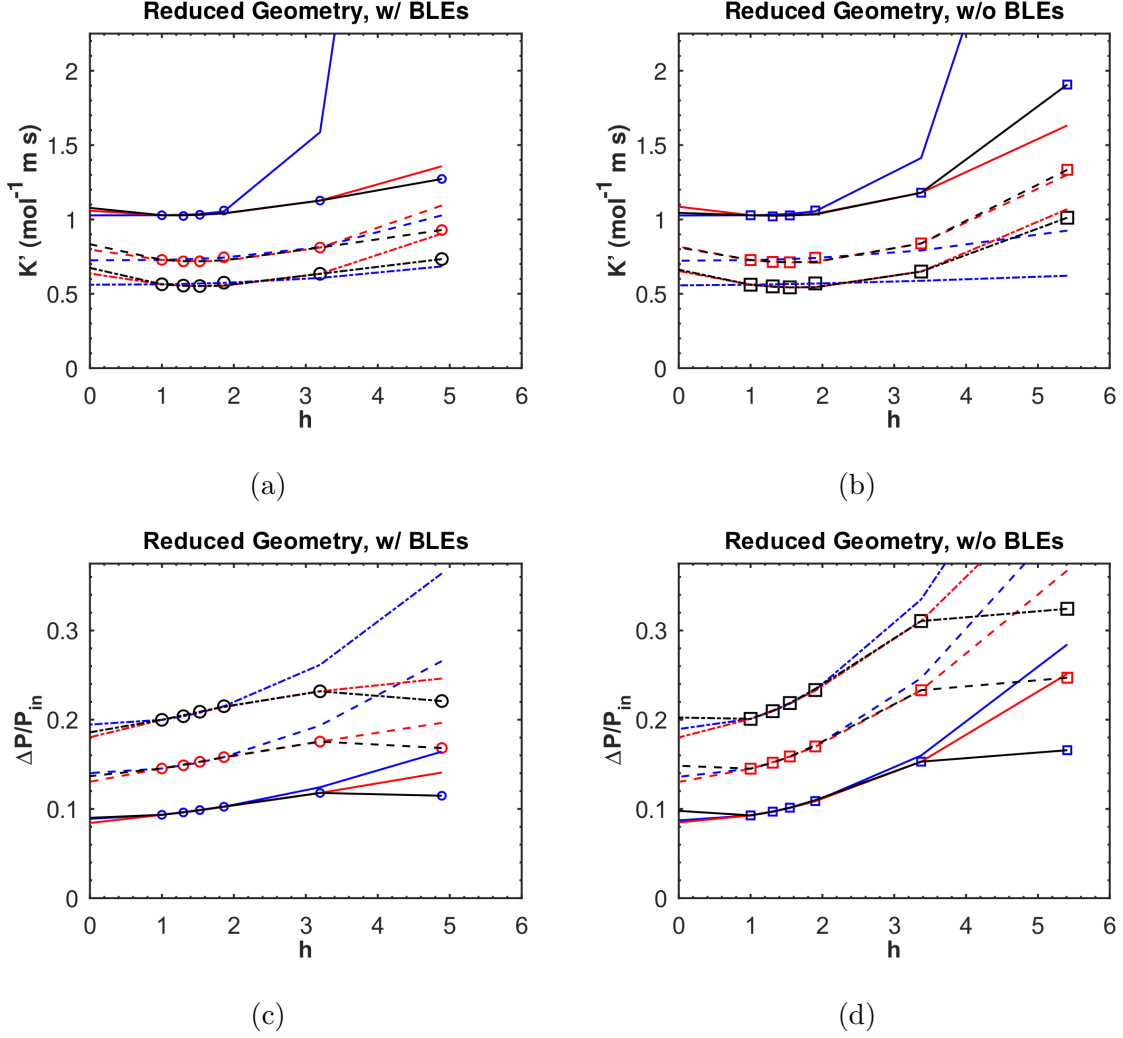


FIG. 16: Scalar response variables and their respective extrapolations as functions of the normalized effective element spacing, obtained at the reduced geometry: GRE (full line), MOE-12 (dashed line), and MOE-123 (dash-dot line) (a) $K' = \Delta\chi_{O_3}/R'_{O_3}$ for the BLEs (○) and (b) no-BLEs (□) mesh variants; and (c) $\Delta P/P_{in}$ for the BLEs and (d) no-BLEs mesh variants. The following values of inlet flow rate Q are shown, with marker size increasing with Q : 250, 350 and 450 cm³ min⁻¹.

the no-BLEs variant.

From Fig. 16 it is concluded that the MOE-12 scheme applied to the no-BLEs mesh variant provides the best agreement between extrapolation scheme and numerical results available. In addition, it was already shown that the results of both BLEs and no-BLEs mesh variants converge at low h (Fig. 4). Thus, given the smaller, albeit slightly, compu-

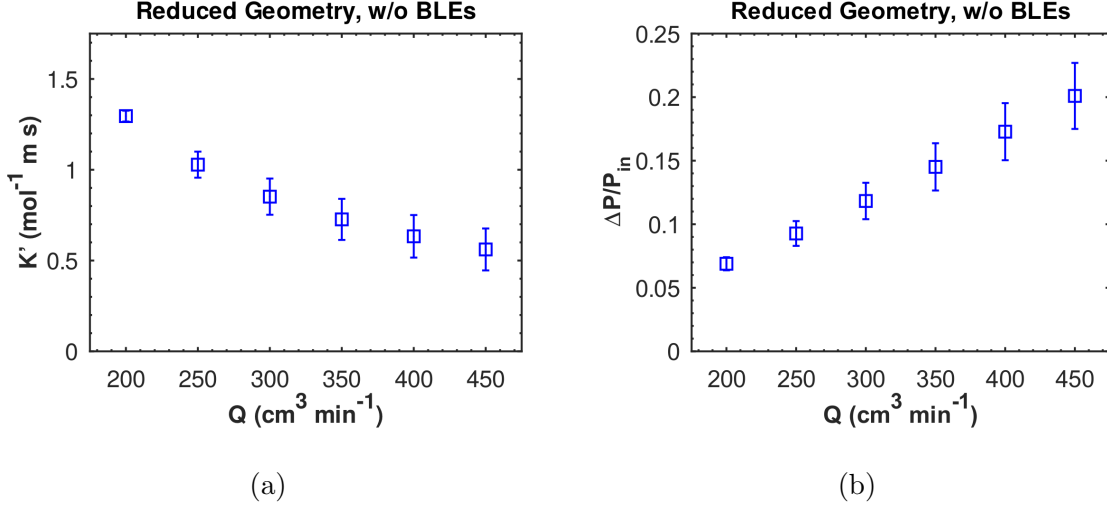


FIG. 17: Scalar response variables as functions of the inlet flow rate, using the no-BLEs mesh variant with the reduced geometry: **(a)** $K' = \Delta\chi_{\text{O}_3}/R'_{\text{O}_3}$ and **(b)** $\Delta P/P_{\text{in}}$. Error bars show the estimated discretization error as given by Eq. 18.

tational cost of using the no-BLEs mesh variant, we now establish it as the standard for further studies and to estimate discretization error for the individual variables and the ratios analyzed so far. Estimation of discretization errors for the BLEs mesh variant can be found in Section SIV B of the SM[26] (Fig. S15 and Table S5).

Carrying on, then, with the error estimate, Figure 17 shows the K' and $\Delta P/P_{\text{in}}$ ratios as function of Q , with the estimated error bars, as given by Eq. 18. As it can be seen, the estimated error interval increases with Q for both variables, as already observed from Fig. 16. The estimated relative errors span the following intervals, with the respective averages:

$$2.25\% \leq \% \epsilon_{\text{M}}[K'] \leq 17.7\%, \% \bar{\epsilon}_{\text{M}} = 11.2\%$$

$$7.98\% \leq \% \epsilon_{\text{M}}[\Delta P/P_{\text{in}}] \leq 14.5\%, \% \bar{\epsilon}_{\text{M}} = 12.7\%$$

For the sake of completeness, and also due to experimental interest, we also briefly report the error estimate for the individual variables. Figure 18 shows the estimates for $\Delta\chi_{\text{O}_3}$, R'_{O_3} , and ΔP , as function of Q . It appears at once that the error estimates for $\Delta\chi_{\text{O}_3}$ (Fig. 18a) are rather large. However that is only because $\Delta\chi_{\text{O}_3}$ spans a relatively small interval for the range of Q simulated. The calculated relative error spans the interval

$$1.03\% \leq \% \epsilon_{\text{M}}[\Delta\chi_{\text{O}_3}] \leq 14.8\%, \% \bar{\epsilon}_{\text{M}} = 8.06\%,$$

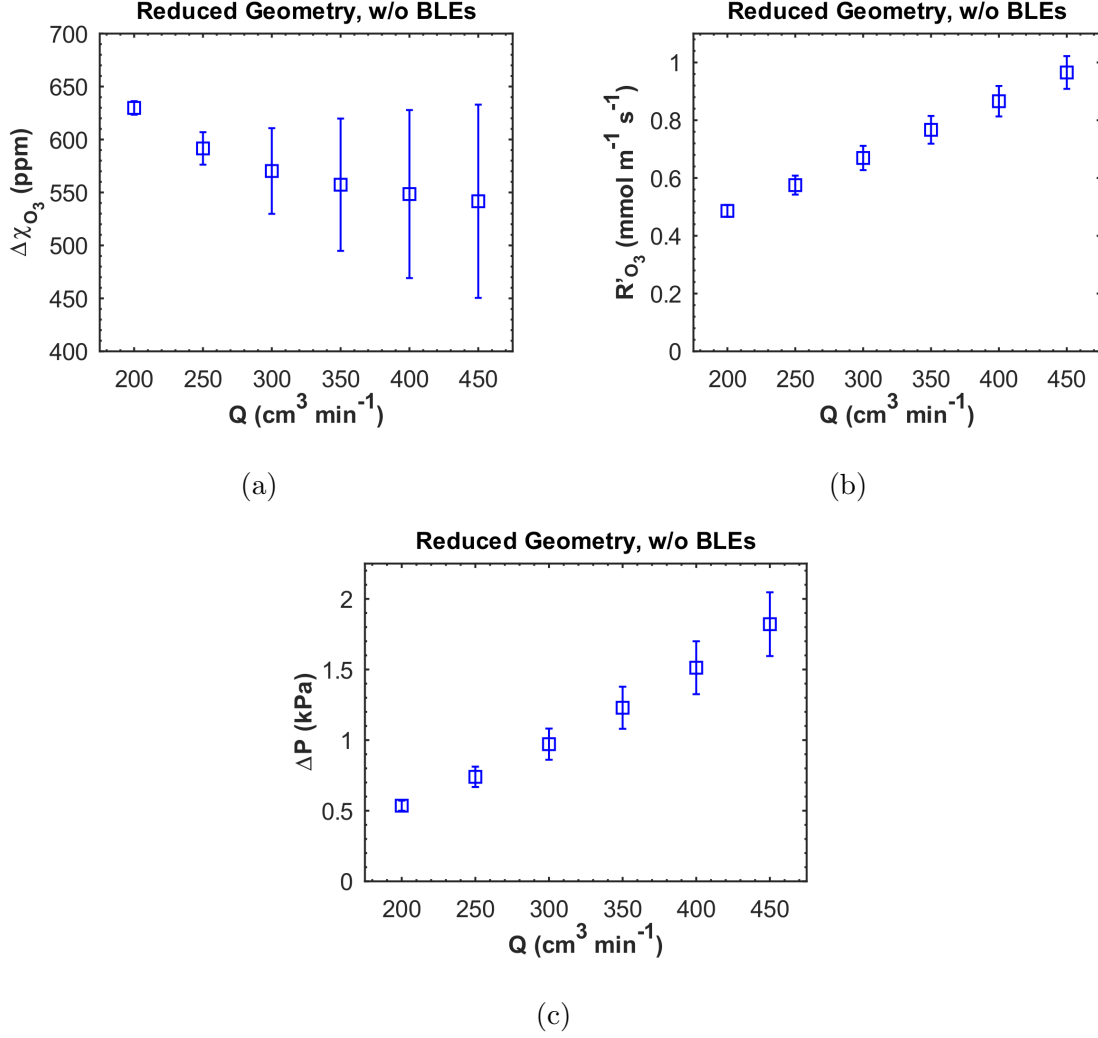


FIG. 18: Scalar response variables as functions of the inlet flow rate, using the no-BLEs mesh variant with the reduced geometry: **(a)** $\Delta\chi_{\text{O}_3}$, **(b)** R'_{O_3} , and **(c)** ΔP . Error bars show the estimated discretization error as given by Eq. 18.

smaller than for the K' ratio. The remaining error estimates are the following:

$$4.33\% \leq \% \epsilon_{\text{M}} [R'_{\text{O}_3}] \leq 6.61\%, \% \bar{\epsilon}_{\text{M}} = 6.01\%$$

$$7.11\% \leq \% \epsilon_{\text{M}} [\Delta P] \leq 13.8\%, \% \bar{\epsilon}_{\text{M}} = 11.9\%$$

While the magnitude of the error estimates might be one order too high, errors of $\sim 10\%$ are not absurd, in particular considering the lower values estimated for the directly comparable scalar variables, $\Delta\chi_{\text{O}_3}$, R'_{O_3} , and ΔP . Two points should be noticed, however. First, it is once again pointed out that the goal of this work is, in part, to estimate the discretization error of the model under discussion, not to prove a point regarding its accuracy. Mathemat-

ical framework aside, these errors are in principle improvable with additional computational resources.

Secondly, these are the estimates for the reduced geometry, which allows a significantly finer mesh and, given the behavior seen in Fig. 16, should present smaller error estimates than the full geometry. Estimating the errors for the full geometry is not straightforward, however, given what is now known of the behavior of the scalar variables as functions of h and the effect different mesh schemes have on the extrapolates. An option is to use the estimates for the reduced geometry: given the estimate of the exact value using the MOE-12 scheme, one may estimate the error at a given h for the reduced geometry using Eq. 18, and thus for the full geometry. Scaling between the reduced and full geometries might be necessary, however, as the scalar ratios used to track convergence are not entirely independent of the geometry. Fig. S16 shows that, for a good approximation, the K' and $\Delta P/P_{\text{in}}$ ratios for the full geometry are linear functions of the ones for the reduced geometry. In particular, as can be expected from Fig. 12, the K' ratio is, to a very good approximation, related by $f_{\text{full}} = f_{\text{reduced}} + C$, where in this case $C \approx 0.028$ (red line in Fig. S16). Thus, the error estimates obtained for the reduced geometry, at $\lambda = 12$, are good estimates for the full geometry. For $\Delta P/P_{\text{in}}$, $f_{\text{full}} \approx 0.030 + 1.39f_{\text{reduced}}$, thus a scaling coefficient of 1.39 should provide an estimate for the full geometry based on the reduced one, albeit not a rigorous one. Similar procedures were taken for the individual variables, where it was found that $\Delta\chi_{\text{O}_3}$ shows a scaling coefficient of 0.96, while for both R'_{O_3} and ΔP it is 1.72 (See Section SV of the SM[26]).

With these points in mind, Figures 19 and 20 present the scalar variables of interest, respectively the ratios and individually, for the full geometry using the no-BLEs mesh variant. In Fig. 19 it can be seen that the error estimates for the ratios are quite similar for both geometries, albeit higher. This is expected given how the estimate was taken and the small differences already seen between meshes with $\lambda = 12$ and 16 (Fig. 4). The error estimates span the intervals:

$$\begin{aligned} 2.14\% \leq \% \epsilon_{\text{M}} [K'] &\leq 19.0\%, \% \bar{\epsilon}_{\text{M}} = 12.2\% \\ 10.2\% \leq \% \epsilon_{\text{M}} [\Delta P/P_{\text{in}}] &\leq 18.2\%, \% \bar{\epsilon}_{\text{M}} = 15.9\% \end{aligned}$$

For the individual variables, Fig. 20 also shows the available experimental data, previously reported in [14]. Again the pattern follows closely that of the reduced geometry, with

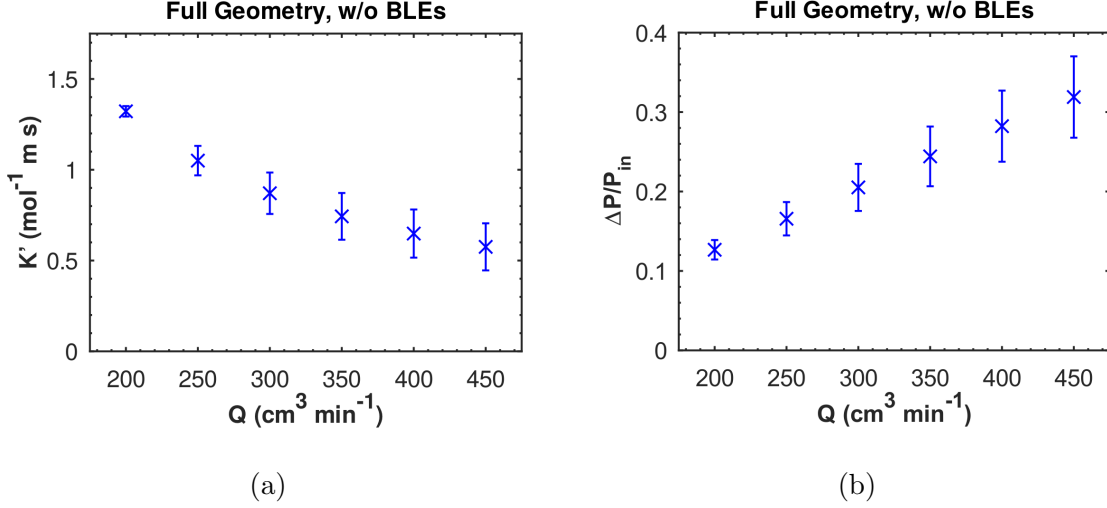


FIG. 19: Scalar response variables as function of the inlet flow rate, using the no-BLEs mesh variant with the full geometry: **(a)** $K' = \Delta\chi_{\text{O}_3}/R'_{\text{O}_3}$ and **(b)** $\Delta P/P_{\text{in}}$. Error bars show the estimated discretization error as given by Eq. 18.

slightly higher error estimates. The calculated error estimates span the following intervals:

$$0.878\% \leq \% \epsilon_{\text{M}} [\Delta\chi_{\text{O}_3}] \leq 9.01\%, \% \bar{\epsilon}_{\text{M}} = 4.85\%$$

$$6.49\% \leq \% \epsilon_{\text{M}} [R'_{\text{O}_3}] \leq 9.37\%, \% \bar{\epsilon}_{\text{M}} = 8.54\%$$

$$11.7\% \leq \% \epsilon_{\text{M}} [\Delta P] \leq 20.6\%, \% \bar{\epsilon}_{\text{M}} = 17.9\%$$

with increased error estimates for R'_{O_3} and ΔP , in line with what was presented above, and a slight reduction in maximum and average error estimates for $\Delta\chi_{\text{O}_3}$. This might be related to the higher absolute values of $\Delta\chi_{\text{O}_3}$, for the full geometry, while using a scaling similar to the reduced geometry when solving the model. Despite such fact, Fig. 20a still shows that, compared to the available experimental data, the absolute error is much greater, approximately 10 times for $Q \geq 300 \text{ cm}^3 \text{min}^{-1}$. For ΔP , the situation is somewhat better, with errors showing at least the same order of magnitude. Nevertheless, it is clear that the meshes being used have great need for improvement, given the precision already available to the experimental device, and the expected increase with future developments.

Additional response variables of interest, concerning the context of Part 1, can be found in Section SVI of the SM[26]. As mentioned in Section II B 2, the O_3 inlet concentration, the normalized R'_{O_3} and K' ratios, and the real and apparent stoichiometries had their discretization errors estimated following the approach described in Section II B 2 and above.

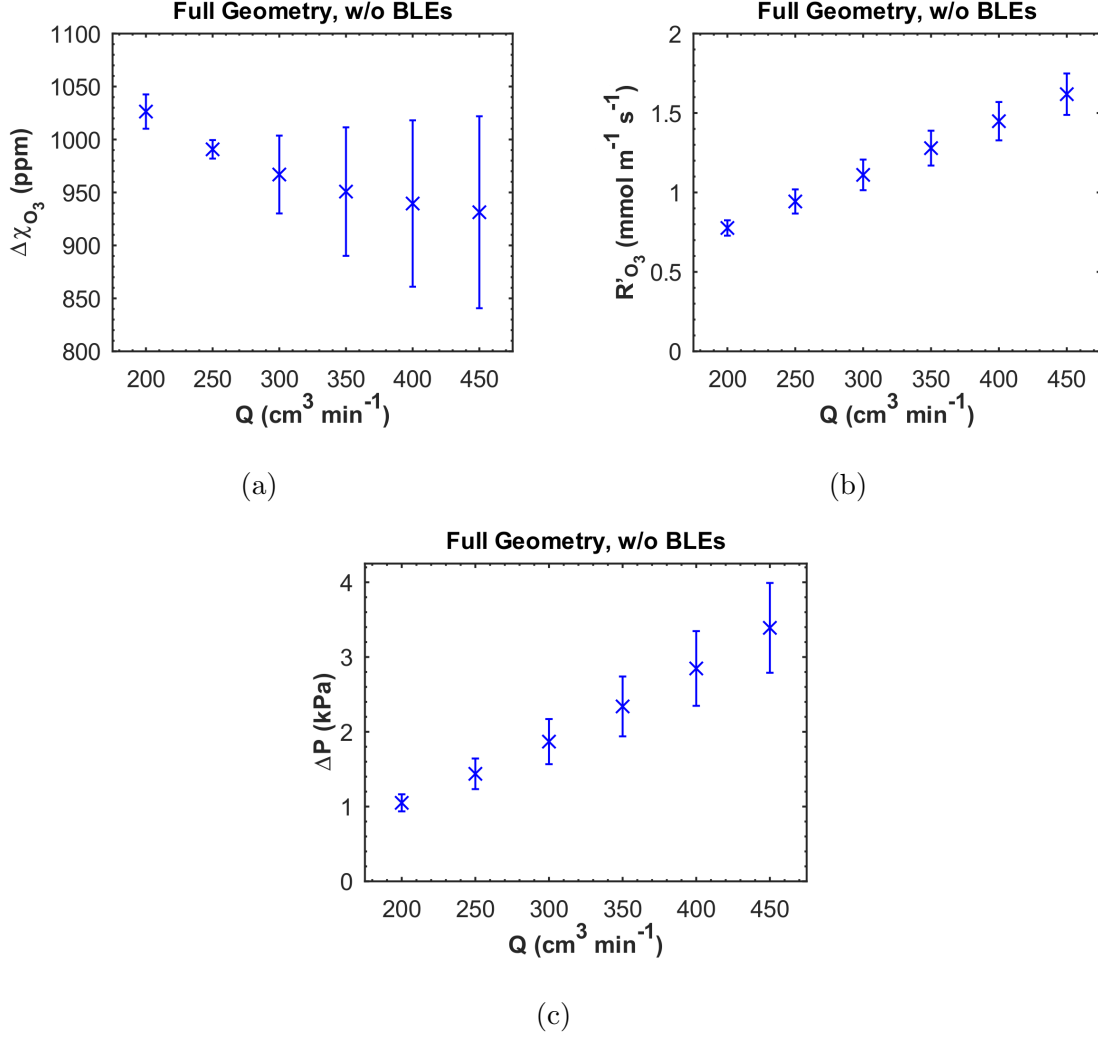


FIG. 20: Scalar response variables as function of the inlet flow rate, using the no-BLEs mesh variant with the full geometry: **(a)** $\Delta\chi_{\text{O}_3}$, **(b)** R'_{O_3} , and **(c)** ΔP . Shown are the numerical results (\times) and available experimental data[14] (\square). Error bars show the estimated discretization error as given by Eq. 18, for the numerical results, and one standard deviation for the experimental data.

Thus, Figs. S17 through S19 show their dependency on h' , the linearity between full and reduced geometries, and the variables as function of Q with their estimated errors.

We conclude this grid convergence analysis of the PEFC prototype model by summarizing the results shown and discussed above. We reiterate the need to assess the uncertainty in a numerical model, be it low or not. The reduced and full geometries used to estimate the discretization error of the model show that it has great need of mesh improvement,

since the estimated relative errors, even for the best meshes, are $\sim 10\%$ and above. However, the grid convergence analysis shows that the experimentally relevant variables show relatively slow convergence, particularly ΔP , and non-monotonic behavior that depends not only on the element size, but also on the mesh scheme. Thus, in addition to finer meshes and additional computational resources, it could be helpful to search for alternatives that might contribute to faster grid convergence, such as structured grids, which might facilitate convergence analysis, but also higher-order interpolation schemes, that, while with increased computational costs, might allow improved error estimates.

IV. SUMMARY

Work is presented concerning progress on numerical modeling of a prototype PEFC[16], building on previously published work[14]. Known limitations of the original model, Alpha, were addressed in order to increase fidelity with the current understanding of fuel cell devices, resulting in the Beta model. In part I of this work, both mathematical frameworks are compared, and approximations and potential shortcomings are discussed (see Part 1). In this part, a grid convergence study has been carried out in order to provide an estimate to the discretization error intrinsic to the updated model.

Grid convergence study was carried out with two mesh schemes, differing only by the existence of so-called “boundary layer” elements (BLEs). Four response variables were tracked in this study, viz. the ratio K' between the drop in reactant molar fraction and the apparent reaction rate, $\Delta\chi_{\text{O}_3}/R'_{\text{O}_3}$; the ratio between pressure drop and inlet pressure, $\Delta P/P_{\text{in}}$; flow speed profiles, U ; and reactant partial pressure profiles, P_{O_3} . Convergence was assessed qualitatively using plots of the variables as a function of an effective, normalized element spacing h , and quantitatively by estimating the discretization error through continuum extrapolates using two different extrapolation schemes[1, 33].

A qualitative assessment of the grid convergence study showed that the use of BLEs leads to non-monotonic behavior in some variables, notably the $\Delta P/P_{\text{in}}$ ratio, while the K' ratio shows non-monotonic behavior for both mesh schemes. Despite such differences at large h (i.e. coarse grids), the mesh schemes converged at low h , suggesting the results were truly approaching mesh independence. In this way, it was established that the no-BLEs mesh scheme was to be used for further assessments and in future studies, and that the finest

mesh available was to be used. Prior to the quantitative assessment, analysis suggested that the so-called Mixed 1st and 2nd order extrapolation scheme[33] (MOE-12) provided the best estimate for the continuum extrapolate, possibly due to the non-monotonic behavior shown by the scalar response variables analyzed. Thus, using MOE-12 on a proxy geometry (fewer channel turns), the estimates of the discretization error, in the inlet flow rate range of $200 \leq Q \leq 450 \text{ cm}^3 \text{ min}^{-1}$, returned average errors of 13.8% for the K' ratio (range of 2.18% to 22.4%) and of 14.0% for the $\Delta P/P_{\text{in}}$ ratio (range of 9.67% to 16.1%).

The grid convergence study also allowed the corroboration of previously established points[14], such as the importance of the turns of the flow channel (Ch) domain on the global flow field, as well as the contribution of convective transport in total molar flux to, and in the porous media (Pm) domains. It was found that secondary flows in the corners of the Ch domain are quite mesh-sensitive, particularly the ones caused by boundary-layer separation (BLS). At low h , BLS produces a pronounced effect on the flow field along the straight sections of the Ch domain, deforming the U profile up to the point that, at $Q = 450 \text{ cm}^3 \text{ min}^{-1}$, the profile is asymmetric with respect to wall distance into the next corner, i.e. it appears that the flow does not fully develop along the straight section. Concerning reactant molar flux, integrated z -component of the molar flux at the Ch-MPS (macroporous substrate) and MPS-CL (catalyst layer) boundaries corroborate a significant contribution of convection to reactant influx to the Pm domains, while average molar flux magnitude inside the Pm domains shows dominance of convective over diffusive transport. Increased mesh resolution ($h \rightarrow 0$) was seen to reduce convective contribution, while simultaneously increasing diffusive transport, although both remain at similar magnitude.

Overall it must be pointed out that the model is not considered to have converged with respect to the discretization. Relative errors of order $\sim 10\%$ in the numerical data are larger than the experimental ones available, which makes actual model validation impossible at the moment. Adding other common sources of uncertainty, such as in parameterization, it is clear that there is a need for denser meshes and schemes with faster convergence, as well as improved methods for error estimation, in the fuel cell modeling community. Given the non-monotonic behavior of some variables of experimental relevance, this work calls for increased caution when comparing numerical to experimental data and when making predictions. On the other hand, uncertainty is only problematic if not acknowledged, and we are of the opinion that a major part of modeling is knowing its limitations and uncertainties. In this

way, the use of proxy models and simpler systems, as exemplified here, may be particularly important to advance on the fundamental understanding of complex devices such as fuel cells.

ACKNOWLEDGMENTS

O.B. acknowledges the Fundação de Apoio à Universidade de São Paulo, FUSP, grant #2968. I.K and T.L. acknowledge the Fundação de Ampara à Pesquisa do Estado de São Paulo, FAPESP, grants #2016/12397-0, and #2014/22130-6 and #2017/15304-6, respectively. Authors also acknowledge the Research Centre for Gas Innovation, RCGI, sponsored by FAPESP grant #2014/50279-4 and Shell Brasil.[36]

-
- [1] P. J. Roache. Quantification of uncertainty in computational fluid dynamics. *Annu. Rev. Fluid. Mech.*, 29:123–160, 1997.
 - [2] C. J. Roy and W. L. Oberkampf. A comprehensive framework for verification, validation, and uncertainty quantification in scientific computing. *Comput. Methods Appl. Mech. Engrg.*, 200:2131–2144, 2011.
 - [3] Christopher Roy. *Review of Discretization Error Estimators in Scientific Computing*. 2010.
 - [4] P. J. Roache. Perspective: A method for uniform reporting of grid refinement studies. *J. Fluid. Eng.*, 116:405–413, 1994.
 - [5] M. Bavarian, M. Soroush, I. G. Kevrekidis, and J. B. Benziger. Mathematical modeling, steady-state and dynamic behavior, and control of fuel cells: a review. *Industrial & Engineering Chemistry Research*, 49:7922–7950, 2010.
 - [6] S. A. Hajimolana, M. A. Hussain, W. M. A. W. Daud, M. Soroush, and A. Shamiri. Mathematical modeling of solid oxide fuel cells: a review. *Renew. Sust. Energ. Rev.*, 15:1893–1917, 2011.
 - [7] A. Z. Weber, R. L. Borup, R. M. Darling, P. K. Das, T. J. Dursch, W. Gu, D. Harvey, A. Kusoglu, S. Litster, M. M. Mench, R. Mukundan, J. P. Owejan, J. G. Pharoah, M. Secanell, and I. V. Zenyuk. A critical review of modeling transport phenomena in polymer-electrolyte fuel cells. *J. Electrochem. Soc.*, 161:F1254–F1299, 2014.

- [8] A. Iranzo, M. Muñoz, F. Rosa, and J. Pino. Numerical model for the performance prediction of a PEM fuel cell. model results and experimental validation. *International Journal of Hydrogen Energy*, 35:11533–11550, 2010.
- [9] B. Carnes, D. Sperjak, G. Luo, L. Hao, K. S. Chen, C.-Y. Wang, R. Mukundan, and R. L. Borup. Validation of a two-phase multidimensional polymer electrolyte membrane fuel cell computational model using current distribution measurements. *J. Power Sources*, 236:126–137, 2013.
- [10] E. Duivesteyn, C. A. Cruickshank, and E. Matida. Modelling of a porous flowing electrolyte layer in a flowing electrolyte direct-methanol fuel cell. *Int. J. Hydrogen Energy*, 38:13434–13442, 2013.
- [11] N. Pourmahmoud, H. Sadeghifar, and A. Torkavannejad. A novel, state-of-the-art tubular architecture for polymer electrolyte membrane fuel cells: Performance enhancement, size and cost reduction. *Int. J. Heat Mass Tran.*, 108:577–584, 2017.
- [12] T. G. Tranter, A. D. Burns, D. B. Ingham, and M. Pourkashanian. The effects of compression on single and multiphase flow in a model polymer electrolyte membrane fuel cell gas diffusion layer. *Int. J. Hydrogen Energy*, 40:652–664, 2015.
- [13] E. Kjeang, J. Goldak, M. R. Golriz, J. Gu, D. James, and K. Kordesch. A parametric study of methanol crossover in a flowing electrolyte-direct methanol fuel cell. *J. Power Sources*, 153:89–99, 2006.
- [14] O. Beruski, T. Lopes, A. R. Kucernak, and J. Perez. Investigation of convective transport in the so-called “gas diffusion layer” used in polymer electrolyte fuel cell. *Phys. Rev. Fluids*, 2:103501, 2017.
- [15] A joint version of parts 1 and 2 can be found with DOI: arXiv:2002.04519.
- [16] T. Lopes, M. Ho, B. K. Kakati, and A. R. J. Kucernak. Assessing the performance of reactant transport layers and flow fields towards oxygen transport: A new imaging method based on chemiluminescence. *J. Power Sources*, 274:382–392, 2015.
- [17] John W. Eaton, David Bateman, Søren Hauberg, and Rik Wehbring. *GNU Octave version 4.2.1 manual: a high-level interactive language for numerical computations*, 2017.
- [18] Available at <https://www.gimp.org/>.
- [19] M. Le Bars and M. G. Worster. Interfacial conditions between pure fluid and a porous medium: implications for binary alloy solidification. *Journal of Fluid Mechanics*, 550:149–173, 2006.

- [20] Z. Fishman, J. Hinebaugh, and A. Bazylak. Microscale tomography investigations of heterogeneous porosity distributions of pemfc gdl. *J. Electrochem. Soc.*, 157:B1643–B1650, 2010.
- [21] Z. Fishman and A. Bazylak. Heterogeneous through-plane distributions of tortuosity, effective diffusivity, and permeability for pemfc gdl. *J. Electrochem. Soc.*, 158:B247–B252, 2011.
- [22] R. Ono and T. Oda. Spatial distribution of ozone density in pulsed corona discharges observed by two-dimensional laser absorption method. *Journal of Physics D: Applied Physics*, 37:730–735, 2004.
- [23] W. J. Massman. A review of the molecular diffusivities of H_2O , CO_2 , CH_4 , CO , O_3 , SO_2 , NH_3 , N_2O , NO and NO_2 in air, O_2 and N_2 near STP. *Atmospheric Environment*, 32:1111–1127, 1998.
- [24] A. Picard, R. S. Davis, M. Gläser, and K. Fujii. Revised formula for the density of moist air (CIPM-2007). *Metrologia*, 45:149–155, 2008.
- [25] R. J. Millington and J. P. Quirk. Permeability of porous solids. *Transactions of the Faraday Society*, 57:1200–1207, 1961.
- [26] Supplemental Material is available at <https://arxiv.org/abs/2002.04519>.
- [27] S. P. Vanka. Block-implicit multigrid solution of Navier-Stokes equations in primitive variables. *J. Comput. Phys.*, 65:138–158, 1986.
- [28] O. Schenk and K. Gärtner. *Parallel Sparse Direct Solver PARDISO - User Guide*, versão 5.0.0 edition, 2014.
- [29] P. R. Amestoy, I. S. Duff, J. Koster, and J.-Y. L’Excellent. A fully asynchronous multi-frontal solver using distributed dynamic scheduling. *SIAM Journal on Matrix Analysis and Applications*, 23(1):15–41, 2001.
- [30] P. R. Amestoy, A. Guermouche, J.-Y. L’Excellent, and S. Pralet. Hybrid scheduling for the parallel solution of linear systems. *Parallel Computing*, 32(2):136–156, 2006.
- [31] Y. Saad and M. H. Schultz. GMRES: A generalized minimal residual algorithm for solving nonsymmetric linear systems. *SIAM Journal on Scientific and Statistical Computing*, 7:856–869, 1986.
- [32] A. Toselli and O. B. Widlund. *Domain Decomposition Methods*. Springer, Berlin, Heidelberg, 1 edition, 2005.
- [33] C. J. Roy. Grid convergence error analysis for mixed-order numerical schemes. *AIAA J.*, 41:595–604, 2003.

- [34] J. A. Ochoa-Tapia and S. Whitaker. Momentum transfer at the boundary between a porous medium and a homogeneous fluid—I. Theoretical development. *International Journal of Heat and Mass Transfer*, 38:2635–2646, 1995.
- [35] Y. Ye, G. Chiogna, O. A. Cirpka, P. Grathwohl, and M. Rolle. Experimental evidence of helical flow in porous media. *Phys. Rev. Lett.*, 115:194502, 2015.
- [36] Author contributions: O.B. designed and conducted the research, analyzed the data and wrote the paper. I.K. contributed with discussions and by revising the paper. T.L. and F.C.F. contributed by revising the paper and with funding sources.